UNIVERSIDADE FEDERAL DE SÃO CARLOS

CENTRO DE CIÊNCIAS EXATAS E DE TECNOLOGIA

PROGRAMA DE PÓS-GRADUAÇÃO EM CIÊNCIA E

ENGENHARIA DE MATERIAIS

IN SITU TRANSMISSION ELECTRON MICROSCOPY STUDY OF NANOSTRUCTURE MIXED OXIDES AT HIGH TEMPERATURES

Santiago Maya Johnson

São Carlos-SP

2018

UNIVERSIDADE FEDERAL DE SÃO CARLOS

CENTRO DE CIÊNCIAS EXATAS E DE TECNOLOGIA

PROGRAMA DE PÓS-GRADUAÇÃO EM CIÊNCIA E

ENGENHARIA DE MATERIAIS

IN SITU TRANSMISSION ELECTRON MICROSCOPY STUDY OF NANOSTRUCTURE MIXED OXIDES AT HIGH TEMPERATURES

Santiago Maya Johnson

Thesis presented to the Post-Graduate Program in Materials Science and Engineering as a partial requirement to obtain the title of DOCTOR OF SCIENCE AND MATERIAL ENGINEERING

Advisor: PhD, Edson Roberto Leite

São Carlos-SP

2018

DEDICATION

To my mother, Olga María Johnson, who always believed in me, and taught me that if you do something, you should do it the right way ... otherwise, it is better not to do it. She was my first teacher and aroused the curiosity that exists inside me; always ask, why?...

I just hope to live up to all their sacrifices.

DEDICATÓRIA

A mi madre, Olga María Johnson, quien siempre creyó en mí, y me enseño que si haces algo, se debe hacer de la manera correcta… sino, mejor no hacerlo. Fue mi primera profesora y despertó la curiosidad que hay en mí; siempre preguntar, ¿por qué?...

Sólo espero estar a la altura de todos sus sacrificios.

RESUME

Master of Engineering - Materials and Process - National University of Colombia, Medellin, Colombia (2014)

Mechanical Engineer - National University of Colombia, Medellin, Colombia (2011).

DISSERTATION COMMITTEE

UNIVERSIDADE FEDERAL DE SÃO CARLOS

Centro de Ciências Exatas e de Tecnologia
Programa de Pós-Graduação em Ciência e Engenharia de Materiais

---

Folha de Aprovação

Assinaturas dos membros da comissão examinadora que avaliou e aprovou a Defesa de Tese de Doutorado do candidato Santiago Maya Johnson, realizada em 19/09/2018:

_____
Prof. Dr. Edson Roberto Leite
UFSCar

_____
Prof. Dr. Márcio Raymundo Morelli
UFSCar

_____
Prof. Dr. Marco Aurelio Liutheviciene Cordeiro
UFSCar

_____
Prof. Dr. Daniel Grando Stroppa
Thermo-Fisher

_____
Prof. Dr. Jefferson Bettini
CNPEM

Certifico que a defesa realizou-se com a participação à distância do(s) membro(s) Daniel Grando Stroppa e, depois das arguições e deliberações realizadas, o(s) participante(s) à distância está(ao) de acordo com o conteúdo do parecer da banca examinadora redigido neste relatório de defesa.

_____
Prof. Dr. Edson Roberto Leite

ACKNOWLEDGEMENTS

Firstly, I would like to express my sincere gratitude to Prof. Antonio José Ramirez, for giving me their confidence and allowing me to work on this challenging project. Also, I would like to express my gratitude to my advisor Prof. Edson R. Leire, who provided me an opportunity to join their team, and who gave access to the laboratory and research facilities. Without they precious support it would not be possible to conduct this research.

I would like to thank my fellow labmates in the LNNano – CNPEM in Campinas, who received me in Brazil, and made me feel at home. The Julian's, Eduardo, Thais, Leonardo, Victor, Joel, and many others that I forget to name. Thanks for the stimulating discussions, the portuguese lessons, for working together, and above all, for all the fun moments we share together.

I would like to thank my fellow labmates in the LIEC – UFSCar in São Carlos, who taught me so many new things, and with whom I shared such good moments. The Bruno's, Julio, Everton, William, Andressa, Renata, Mario, Régis, and all the others. Thanks for the stimulating discussions, the talks in the corridors, for your support and help.

My sincere thanks to all my friends, Juan Pablo, Dario, Ramon, Monica, Claudia, Rodolfo, Jeanine, and everyone with whom I shared during these last four years. Thanks for the laughs and the good times, and above all, for sharing your time with me, the most valuable thing that we all have.

Thanks to my family, for his love, for supporting me, and encourage me to go ahead. Without his teachings I would not be who I am today. Words cannot express how grateful I am.

iv

Last but by no means least, thanks to Leidy, who has accompanied me (and has tolerated me) during these last years, by his side everything has become easier, the penalties and sacrifices have been divided, and the joys and achievements have been added.

ABSTRACT

This work addresses the characterization of the high temperature reactions between different nanoparticles oxides, CeO_2-ZrO_2 and CeO_2-SnO_2, by the direct observation of the phenomenon by *in situ* Transmission Electron Microscopy (TEM). The nanoparticles were synthesized via three different synthesis methods, hydrothermal, solvothermal, and solvent-control. The changes in the size and morphology of the nanoparticles, the interactions that lead to processes of sintering / densification, and the phase transformations that occur during the experiments were documented. Also, a detailed study of the influence of the electron beam current density on the sample, and its synergism with the temperature during the in situ experiments was performed. The interactions between the oxide metal nanoparticles and the films of the TEM grids showed a great influence during the *in situ* tests at high temperature. For the experimental setups tested in this work, the main mechanism of interaction between the nanoparticles was oriented attachment.

Keywords: High-Resolution Transmission Electron Microscopy (HRTEM); *in situ* Transmission Electron Microscopy; metal oxide nanoparticles; nanoparticle synthesis; oriented attachment.

RESUMO

ESTUDO DE MICROSCOPIA ELETRÔNICA DE TRANSMISSÃO *IN SITU* DE NANOESTRUTURA DE ÓXIDOS MISTOS EM ALTAS TEMPERATURAS

Este trabalho aborda a caracterização das reações em alta temperatura entre diferentes nanopartículas de óxidos metálicos, CeO_2-ZrO_2 e CeO_2-SnO_2, pela observação direta do fenômeno pela Microscopia Eletrônica de Transmissão (MET) *in situ*. As nanopartículas foram sintetizadas através de três diferentes métodos de síntese, hidrotérmico, solvotérmico e controle de solvente. As mudanças no tamanho e morfologia das nanopartículas, as interações que levam a processos de sinterização/densificação e as transformações de fase que ocorrem durante os experimentos foram documentadas. Além disso, um estudo detalhado da influência da densidade de corrente do feixe de elétrons na amostra e seu sinergismo com a temperatura durante os experimentos *in situ* foram realizados. As interações entre as nanopartículas de óxidos metálicos e os filmes das grades (grids) para MET mostraram grande influência durante os testes *in situ* em altas temperaturas. Para as configurações experimentais testadas neste trabalho, o principal mecanismo de interação entre as nanopartículas foi a fixação orientada (oriented attachment).

Palavras-chave: Microscopia Eletrônica de Transmissão de Alta Resolução (HRTEM); Microscopia Eletrônica de Transmissão *in situ*; nanopartículas de óxidos metálicos; síntese de nanopartículas; fixação orientada.

PUBLICATIONS

- **MAYA-JOHNSON, SANTIAGO**; GRACIA, LOURDES; LONGO, ELSON; ANDRES, JUAN; LEITE, EDSON R. Synthesis of Cuboctahedral CeO_2 Nanoclusters and Their Assembly into Cuboid Nanoparticles by Oriented Attachment. In: CHEMNANOMAT 3 (4), 228-232; 2017.

- SCZANCOSKI, JÚLIO; **MAYA-JOHNSON, SANTIAGO**; DA SILVA PEREIRA, WYLLAMANNEY; LONGO, ELSON; LEITE, EDSON R. Atomic diffusion induced by electron-beam irradiation: An in situ study of Ag structures grown from α-Ag_2WO_4. In: Crystal Growth & Design (Submitted 16-Jul-2018)

Posters presented in Congresses and Conferences

- **S. Maya-Johnson**, Edson R. Leite; Synthesis and Characterization of CeO2 Nanoclusters with a Very Narrow Size Distribution. 7th Latin American Conference on Metastable and Nanostructured Materials, NANOMAT 2017; Brotas – SP.

- **Santiago Maya Johnson**, Edson Roberto Leite, Lourdes Gracia Edo, Juan Andrés, and Elson Longo; A Theoretical and Practical Approach to the Formation of CeO2 Cuboid Nanoparticles from the Synthesis and Assembly of Cuboctahedral Nanoclusters by Oriented Attachment. XVI Brazilian MRS Meeting, 2017; Gramado – RS.

- **Santiago Maya Johnson** and Edson Roberto Leite; High Temperature Reactions Between CeO2 and ZrO2 nanoparticles. XVI Brazilian MRS Meeting, 2017; Gramado – RS.

x

INDEX

LIST OF TABLES

LIST OF FIGURES

SYMBOLS AND ABBREVIATIONS

BF   Bright-Field

BFP   Back Focal Plane

BSE   Backscattered Electrons

CBED   Convergent Beam Electron Diffraction

CCD   Charge-Coupled Device

Ce(aca)3   Cerium(III) acetylacetonate

DF   Dark-Field

DPs   Diffraction Patterns

DTA   Differential Thermal Analysis

DTG   Derivative Thermogravimetry

EBCD   Electron Beam Current Density

EDX, EDS or **EDXS**   Energy-Dispersive X-Ray Spectroscopy

EELS   Electron Energy Loss Spectroscopy

EM   Electron Microscope (or Microscopy)

ETEM   Environmental Transmission Electron Microscope (or Microscopy)

FEG   Field Emission electron Gun

FFT or **FT**   (fast) Fourier Transform

FTIR   Fourier Transform Infrared

FWHM   Full Width at Half Maximum

HAADF   High-Angle Annular Dark Field

HRTEM   High-Resolution Electron Microscope (or Microscopy)

JCPDS   Joint Committee on Powder Diffraction Standards

LED   Light Emission Diode

MEMS   Microelectromechanical Systems

mt   metric tons

NCs   nanocrystals

OAc   Oleic Acid

OAm   Oleylamine

OLA   Oleyl Alcohol

OSC   Oxygen Store Capacity

ppm	Parts per million
rcf	Relative Centrifugal Force
REEs	Rare Earths Elements
ROS	Reactive Oxygen Species
rpm	Revolutions per minute
SAD or **SAED**	Selected-Area (electron) Diffraction
SE	Secondary Electrons
SEM	Scanning Electron Microscope (or Microscopy)
SNR	Signal-to Noise Ratio
STEM	Scanning Transmission Electron Microscope (or Microscopy)
TEM	Transmission Electron Microscope (or Microscopy)
TG	Thermogravimetry
TGA	Thermogravimetric Analysis or Thermal Gravimetric Analysis
THF	Tetrahydrofuran
TWC	Three-Way Catalysis
USD	United State Dollar
UV	Ultraviolet
XRD	X-Ray Diffraction
Z	atomic (or proton) number
α	alfa
β	beta
γ	gamma
Δ	delta
μ	micron
λ	lambda
σ	sigma

1 INTRODUCTION

The first prototype of an electron microscope was made by the German physicist Ernst Ruska and the electrical engineer Max Knoll in Berlin in 1931. In 1986, shortly before his death, Ruska received the Nobel Prize "*for his fundamental work in electron optics, and for the design of the first electron microscope*". Moreover, Reinhold Rudenberg, the scientific director of Siemens-Schuckertwerke, obtained the patent for the electron microscope in May 1931. In 1930 the 2 ¾ year-old son of Rudenberg became ill with leg paralysis, the illness was diagnosed as poliomyelitis, known to be caused by a virus. This encourages Rudenberg to find a way to make such a small virus visible, because they are too small to be detected under an optical microscope.

In 1933 Ruska build an electron microscope that exceeded the resolution attainable with an optical microscope, but it was only until 1938 that the first commercial electron microscope was produced by Siemens. After years of development in the lenses and detectors, in 1965 the Cambridge Scientific Instrument Company finally let to the market the first commercial Scanning Electron Microscope (SEM) named "Stereoscan". While in 1965 the scanning microscopy was barely born, in the 1960s and 1970s the first megavolt Transmission Electron Microscopes (TEM) was developed. These instruments had sufficient space in their specimen stages to accommodate heating, tensile and gas-reaction stages, and also were powerful enough to permit observation of specimens that were thick enough to mimic bulk behavior.

Nowadays the Electron Microscopy (EM) has evolved greatly making possible, and common, the acquisition of images of atomic resolution. Today the materials and biological science would not be the same without the characterization techniques of the modern EM, but of equal importance to the new developments in EM are the development of new detectors, specimen holders, and the improvements in our capacities to record dynamic images with modern video/CCD cameras as well as store and the digital process of that images [1]. Looking back it would appear that the EM is merely able to provide information from the three-dimensions of the objects. However, the time is our fourth dimension and, indeed, it has been demonstrated since decades that

experiments can be conducted in real time inside the specimen chamber of electron microscopes [2,3]. This field of experimentation became known as *in situ* electron microscopy. In recent years, *in situ* TEM techniques were developed by introducing various attachments, such as gas, force, electricity, heat, and so on [4]. A stage designed to heat specimens up to high temperatures in the microscope allow us to observe phase transformation, change in the oxidation states or reactions between nanostructures at atomic level.

"*We live in a society exquisitely dependent on science and technology, in which hardly anyone knows anything about science and technology.*"

- Carl Sagan

The same quote by Carl Sagan can be applied to nanotechnology. In the last two decades, the number of scientific articles related to the terms "nano" or "nanotechnology" has increased from a few to tens of thousands (Figure 1.1), according to a search made on Scopus. Today we use nanotechnology in many products of our daily lives, from microprocessors, electronics and medicine to cosmetics and textiles. New properties, applications, related to nano-scale products are discovered every day.
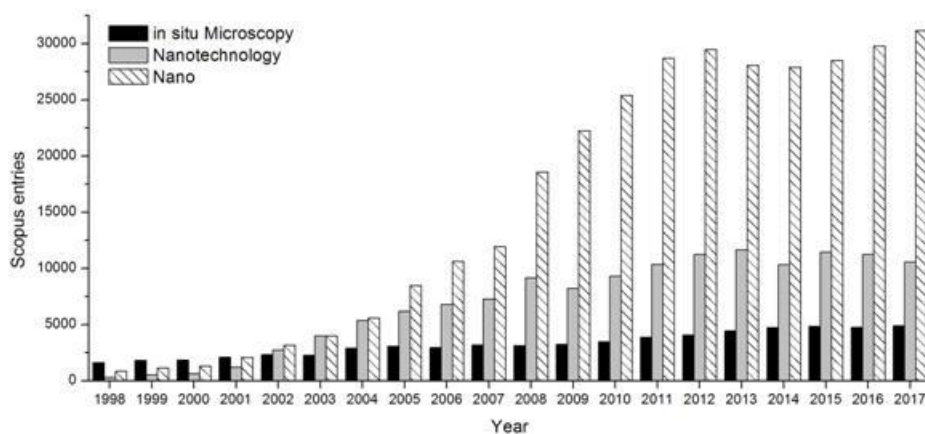
Figure 1.1 - Number of scientific publications per year related to nano, nanotechnology or *in situ* microscopy.

Since the beginning of humanity, man has had the ability to master new technologies, even without understanding them. 1.5 million years ago, *Homo erectus* used fire even before knowing how to create it. In ancient times, silver was used to serve beverages intended for monarchs and aristocrats; its antiseptic properties were known thousands of years before the invention of the optical microscope and identification of bacteria and other microorganisms. Nowadays we use silver nanoparticles to increase their bactericidal properties.

It is obvious that a better understanding of the phenomena that occur on at nanoscale will allow us to enhance the already known properties and applications, and maybe discover some new ones. This is why the *in situ* electron microscopy is so important, since it allow us to observe these phenomena in real time.

Even with *in situ* microscopy, reproduce the exact phenomenon is difficult, since the conditions of vacuum and high electron radiation to which the sample is exposed inside the microscope can alter its normal behavior. Another problem is the lack of reproducibility, which makes difficult the comparison between the obtained results and others reported in the literature. Two-thirds of researchers who responded to a survey by the journal <u>Nature</u> said that current levels of reproducibility are a major problem. Pressure to publish, selective reporting, poor use of statistics and finicky protocols can all contribute to wobbly work [5].

The main objectives of this work are: The synthesis of CeO_2, ZrO_2 and SnO_2 nanoparticles, and the subsequent *in situ* observation of high temperature reactions between CeO_2-ZrO_2 mixed oxides and SnO_2-CeO_2 mixed oxides; developing a reproducible methodology that can be used in other systems. To explore the dynamic changes that take place in nanoparticles and mixed oxides at high temperature, like changes in size, morphology and phase, by the direct observation of the phenomenon. An atomic level characterization of the crystal structures of simple and mixed oxides at several temperatures using High Resolution Transmission Electron Microscopy (HRTEM) and other techniques.

Address new technical and experimental advancements for *in situ* TEM that will contribute to the local "Know how" to further investigations.

2 LITERATURE REVIEW

2.1 A brief summary of Cerium, Zirconium, and Tin oxide

In 2010 the global production of rare earths elements (REEs) was 133600 metric tons (mt). Cerium was the highest consumed elements accounting for over 39% of global consumption in 2012 [6], for this year the global REEs market was valued at USD 4.3 billion and is expected to reach USD 10.9 billion by 2020; being the catalysts one of the dominant applications. United States major end uses for REEs include automotive catalytic converters and fluid cracking catalysts in petroleum refining with about 60% of the local consumption [7].

Brazil is the fourth worldwide producer of REEs, although China has a monopoly with around 96.9% of the total production [7]; New technological knowledge in the extraction and production of REEs are under development, but it is not enough because for be at the forefront with these strategic minerals it is imperative a full understanding of all the aspects around their performance. As Senator Luiz Henrique said, "*Brazil cannot once again make the same mistake we made in the 30s and 50s, when it became exporter of radioactive ores and denied to master nuclear technology*" [8].

Cerium is the most abundant member of the series of elements known as lanthanides or REEs, ranked 26 with 66 ppm just above the Zinc and Cooper with 76 ppm and 68 ppm respectively [9]. Its high abundance, combined with excellent catalytic activity for a variety of reactions, makes cerium the element of choice. Cerium is characterized chemically by having two stable valence states, Ce^{+4}, ceric and Ce^{+3}, cerous. The ceric ion is a powerful oxidizing agent but when associated with oxygen is completely stabilized and indeed cerium oxide, $Ce^{4+}O_2$, (also called ceria) is the form of cerium most widely used.

Ceria (CeO_2) is one of the most reactive rare-earth metal oxides, recently it has attracted vast attention due to the promise it raises for many technological applications in a wide range of fields. The three-way catalysts (TWC), oxygen sensors, solid fuel cells, UV blockers and superhydrophobic coating are just a few representative examples [10–14]. Ceria has been one of the most widely used heterogeneous catalysts particularly in three way catalytic converters.

Most of the catalytic traits can be attributed to two properties of ceria: first, the high mobility and storage capacity of oxygen within the lattice; second, the ease with which cerium changes between Ce^{3+} and Ce^{4+} states. These properties, combined with the abundance of cerium on earth, make ceria a low-cost highly effective alternative to noble metal catalysts. Recent research has been focused on the nanoscale properties of ceria [15], shown that nanostructured CeO_2 gives a superior performance to bulk CeO_2 when they are used as either catalyst or support [16].

On the bulk, when a O vacancy is created, two of the adjacent Ce cations change from Ce^{+4} to Ce^{+3}. In nanoparticles, various studies has shown that decreasing the particle size increase the Ce^{+3}/Ce^{+4} ratio [17–19]. Due to these change on the oxidation states ceria become the focus of attention, since satisfactory results have been reported in antibacterial [20], antioxidant [21–23], and biological applications. On the later, ceria can act as radical scavenging and protect the cells against reactive oxygen species (ROS) [19,21,24], on *in vitro* and *in vivo* tests ceria appear as a promising therapeutics for neuronal degenerative disorders [22,23,25]. To be successfully applied in biology nanoparticles should combine the properties of solids with the mobility of the molecules, besides of being stable and not agglomerate. Hence the value of synthesize small size particles with large surfaces that can interact with biological systems.

Zirconium oxide (ZrO_2) known as zirconia is also a relevant material in electronic ceramics and catalysis. Zirconia is an extremely versatile ceramic with superior chemical stability, mechanical strength and ion-exchange capacity that has found use in oxygen sensors, fuel cells, thermal barrier coatings, and other high-temperature applications [26,27].

In recent studies it has been shown that the redox behavior of cerium oxide can be severely modified by incorporation of zirconium and the formation of mixed Ce-Zr oxides [28–35]. Among the possible compositions and phases forming CeO_2-ZrO_2 mixed oxides in solid solution, it has been shown that the greatest promoting effect on cerium reduction is produced for compositions of $Ce_{1-X}Zr_XO_2$ with $0.2 \leq X \leq 0.5$ [33,36]. Further of the effect of other elements

addition, the effect of the preparation method is also important; Devaraju *et al.* compared the solvothermal and co-precipitation calcinations methods, showing that the latter has a greater oxygen storage capacity (OSC) [33].

Moreover, Tin oxide (SnO_2) based nanomaterials have received interest for use in gas/chemical sensor, transparent conductive electronics, electronic devices such as logic gates and computing circuits [37–39] and recently to fabricate ultraviolet light emission diodes (UV LEDs) [40]. Some studies have exposed the benefits of the addition of CeO_2 to SnO_2, showing an enhance in the thermal stability and catalysis activity for CO and CH_4 oxidation [41], as well as the selectivity to CO compared to CH_4 as a gas sensor [42]. Also, adding SnO_2 to CeO_2 shows more catalytic CO oxidation [43].

Parenthesis

Throughout this text the word *surface* will be used arbitrarily. At macro and microscopic scale, a surface can be defined as the interface between the matter and its environment, either air, material, or vacuum; and this interface have a thickness (which most times is greater than the diameter of the nanoparticles that will be studied in this text). At atomic scale, *we will call "surface", the last layer of atoms on our particles, film, etc.*

2.2   Phase diagrams and solubility

The first contribution to the ceria-zirconia system was made by L. Passerini in 1930. Due the importance of this system even in the last decade still made research and contributions to this phase diagram [44–46]. Several studies found a different compound form of tetragonal zirconia or fluorite ceria, with 40mol % CeO_2 ($Ce_{0.4}Zr_{0.6}O_2$) who is stable below 870°C after long periods of annealed in bulk oxides. It is worth to highlight that for these bulk oxides around 1000°C and between 20-80 mol % of CeO_2 have a combination of tetragonal and fluorite phases, while in nanostructures for the same range only the fluorite structure is present, this is an example that the materials can behave in unusual ways when are in nanoscale. Figure 2.1 shows a tentative phase diagram for the CeO_2-ZrO_2 system, developed experimentally [45].

Comparing the solubility of both oxides in the bulk with the nano form we can see variations. The boundary of the solid solution of ZrO_2 in fluorite-type

cubic CeO_2 at 1250°C is 30 mole percent (in the bulk) [46]. While in the nano size, the solid solution of ZrO_2 in fluorite phase of CeO_2 nanoparticles can be as high as 40 mole percent at room temperature [47]. The increase of the solubility of an element in small particles (nano) is already well known for years [48], but this approach is merely theoretical and no information was found in the literature for such small size as the evaluated in this work. Also, even though both elements (Ce, and Zr) have high solubility there is no guarantee that the particles of the two species will react with each other to form a new particle of homogeneous composition.
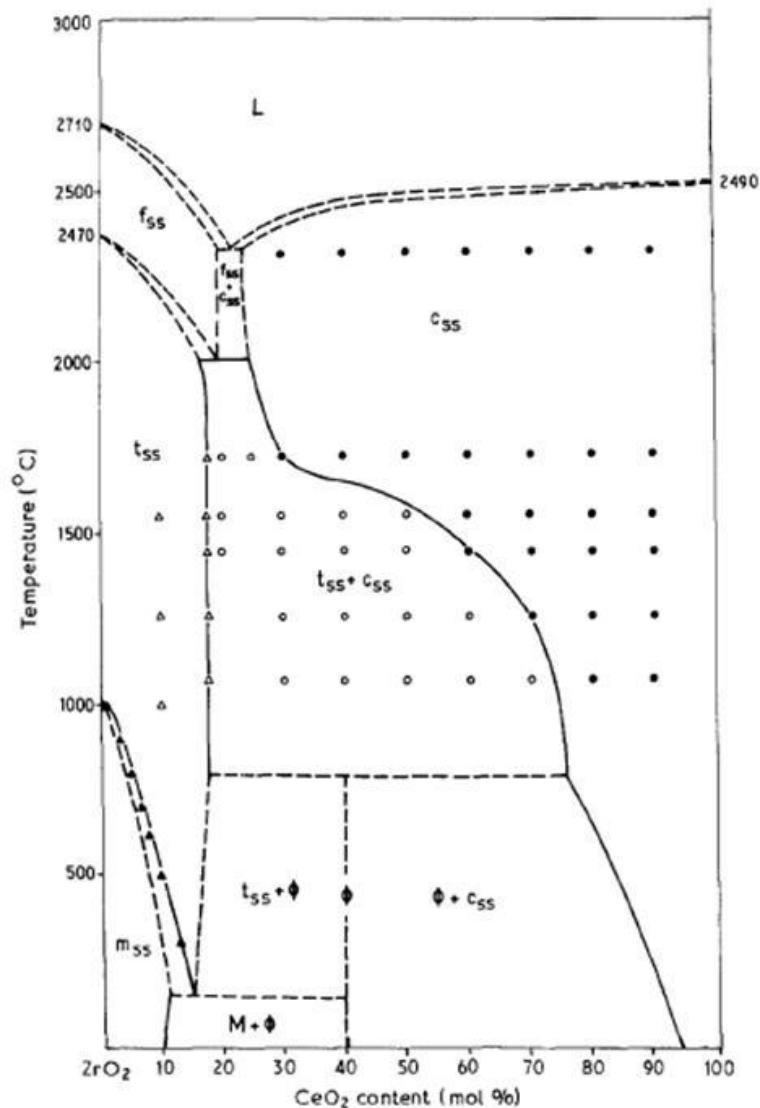
Figure 2.1 - Tentative phase diagram for the ZrO_2-CeO_2 system, proposed by Duran *et al* [45].

For the CeO_2-SnO_2 system no phase diagram was found, but some works gives an idea of the solubility of an oxide in the other. Ayastuy *et al.* estimated the limit of solubility of tin into ceria lattice (fluorite) as 22mol %, but it is possible to see a small peak of SnO_2 at 15mol% (Figure 2.2a) in their XRD which infers that the solubility is between 10-15mol % [43]. Instead, when the cerium is the dopant can enters the lattice of SnO_2 to form solid-solution up to 33mol % without segregation of CeO_2 [41]. Observing the result of Xu *et al.* it is appreciated an increase of the Full Width at Half Maximum (FWHM) in the ceria doped tin oxide, and also no peak of ceria appears (Figure 2.2b), which demonstrates a variation in the lattice parameters due to non-uniform strain induced by the substitutional cerium in solid solution.
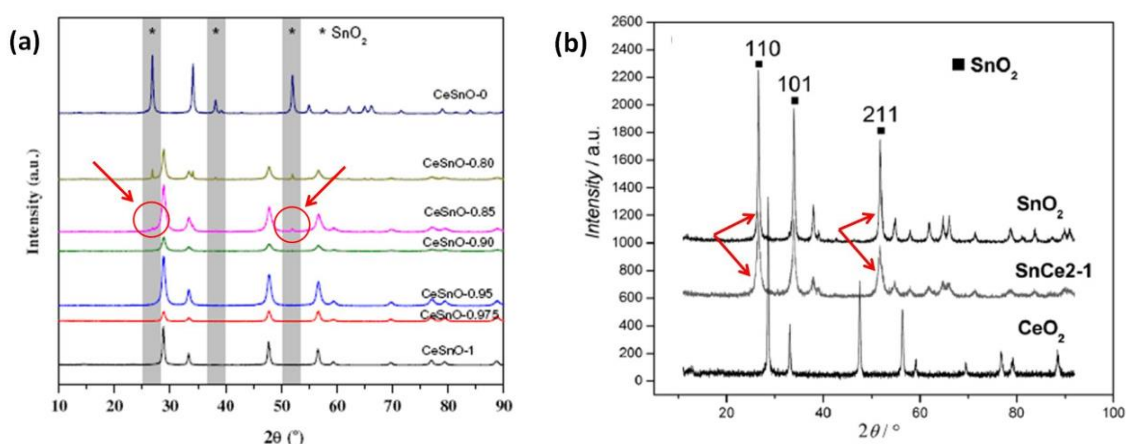
Figure 2.2 - a) XRD patterns of CeO_2-SnO_2 mixed oxides, variation from 0 to 0.20 mol % of tin oxide [43], and b) comparison of the two pure oxides with a mixture with Sn/Ce atomic ratio of 2:1 corresponding to 33mol % of CeO_2 [41]. The red arrows in (a) indicate the appearance of tin oxide at 15mol %; in (b) shows an increase of the Full Width at Half Maximum of tin oxide due to cerium in solid solution at 33mol %.

In the ceria-zirconia system, it is know that both oxides are soluble and a complete reaction of both oxides can be expected, but for the ceria-tin oxide system the solubility of an oxide in the other is different and there is no suspicion of what might happen.

2.3   Conceptual Framework

2.3.1   Electron microscope

A *microscope* is an instrument that increases resolution over that of the human eye alone (about 150 µm between two points or lines).   An electron microscope is a microscope that uses a beam of accelerated electrons as a source of illumination.   The two main types of electron microscopes are: scanning and transmission.   A scanning electron microscope (SEM) scans a focused electron beam over a surface to create an image.   The electrons in the beam interact with the sample, producing various signals, and the reflected electrons can be used to obtain information about the surface topography and composition.   In a transmission electron microscope (TEM) the electron beam is transmitted through a specimen to form an image.   The word "transmission" suggests that the sample must be fine enough for the electrons to pass through it (usually less than less than 100 nm thick).

Microscopy is the interpretive use of microscopes.   No matter what kind of microscope, employing whatever medium, manner, or kind of specimen, microscopy also requires a primary observer to interpret the image.

Resolution is the distance between two specific points or parts of the object as viewed by the eye, microscope, camera, or video.   *Resolving power* is the ability to distinguish two points of an object as separate in an image (with their diffraction discs not overlapping more than half their diameters).   The resolving power is expressed theoretically as the minimum distance between two adjacent, separated points; resolution is the actual perception of the two separate points.   Practical resolution needs adequate contrast [49].

When a wave passes through a circular aperture it diffracts, producing an interference pattern of dark and light regions.   The bright region at the center of this diffraction pattern is known as the Airy disk, which together with the series of concentric bright rings around is called the Airy pattern.   Figure 2.3a illustrates a hypothetical Airy disk that essentially consists of a diffraction pattern containing a central maximum (typically termed a *zeroth order*

maximum) surrounded by concentric 1st, 2nd, 3rd, etc., order maxima of sequentially decreasing brightness that make up the intensity distribution. Two Airy disks and their intensity distributions at the limit of optical resolution are illustrated in Figure 2.3b. In this part of the figure, the separation between the two disks exceeds their radii, and they are resolvable. The limit at which two Airy disks can be resolved into separate entities is often called the *Rayleigh criterion*; which is extensively used to determine the resolution of microscopes. Figure 2.3c shows two Airy disks and their intensity distributions in a situation where the center-to-center distance between the zeroth order maxima is less than the width of these maxima, and the two disks are not individually resolvable by the Rayleigh criterion.
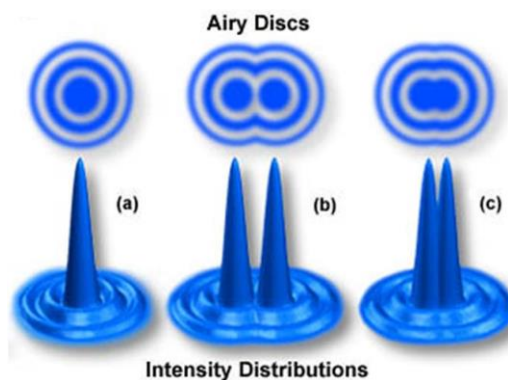
Figure 2.3 - Airy disks and their intensity distributions as a function of separation distance. From Olympus America, Inc.

2.3.1.1   Interactions of electrons with matter

Electrons are one type of ionizing radiation, which is the general term given to radiation that is capable of removing the tightly bound, inner-shell electrons from the attractive field of the nucleus by transferring some of its energy to individual atoms in the specimen. One of the advantages of using ionizing radiation is that it produces a wide range of secondary signals from the specimen. Figure 2.4 summarizes some of those signals, which can be detected in different types of TEM. The directions shown for each signal do not always represent the physical direction of the signal, but indicate, in a relative manner, where the signal is strongest or where it is detected [1].

When a high-energy beam of electrons interacts with a thin specimen a wide range of secondary signals are produced. There are two types of interactions: elastic and inelastic. One of the main signals produced by elastic interactions is the elastically scattered electrons, which is the major source of contrast in TEM images, also creates much of the intensity in diffraction patterns (DPs). The inelastic interactions are equally important since they generate a whole range of signals, each of which can tell us more about the chemistry of the specimen than we can find out from the elastic electrons. Some of the most important signals are the electron energy-loss, the characteristic X-rays, secondary electrons, and, occasionally, visible light (cathodoluminescence).
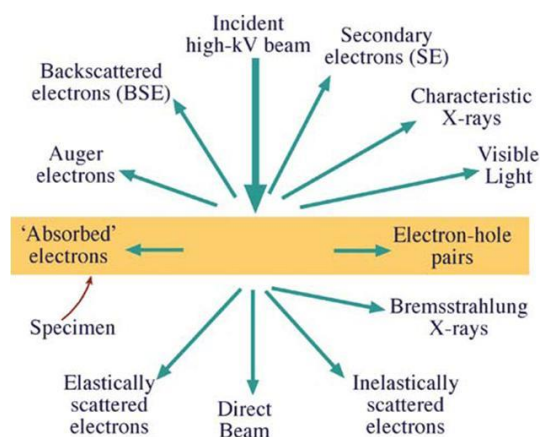
Figure 2.4 - Signals generated when a high-energy beam of electrons interact with a thin specimen [1].

2.3.1.2   Electron beam damage

The inelastic collisions that give us all these useful signals unfortunately have a side effect, electron-beam damage (radiation damage). The damage, which affects the structure and/or the chemistry of the specimen, depends, in some form or other, on the incident-beam energy. Certain materials are more susceptible than others but, in the end, you can damage virtually anything that you put into the TEM, particularly now that aberration correction permits even more electron current to be focused into even smaller beams. Therefore,

damage represents a real physical limit on what the TEM can do and may be regarded as the microscopists' analog of the Heisenberg uncertainty principle in that the very act of observing your specimen can change it [1].

On the other hand, sometimes we can use beam damage to aid certain *in-situ* transformations that are speeded up by the damage process or we can use electron damage to emulate other forms of radiation damage. Generally, however, beam damage must be considered undesirable. Damage takes one of three principal forms [1,50]:

- *Radiolysis:* Inelastic scattering (mainly electron-electron interactions such as ionization) breaks the chemical bonds of certain materials such as polymers and alkali halides. The excitation needs to be localized for a time long enough for the atom to respond mechanically, and the energy acquired by the excited atom must be convertible into momentum, resulting in atomic displacements.
- *Knock-on damage or sputtering:* Knock-on damage is the displacement of atoms from the crystal lattice and creates point defects. These processes are ubiquitous if the beam energy (E_0) is high enough. If the kinetic energy acquired by an atom is higher than its displacement threshold energy (E_d) or surface binding energy (E_s), the atom may be displaced from its site to an interstitial or vacancy, forming a Frenkel pair in the bulk, or sputtered away from surfaces into vacuum. In TEM/STEM, the surface sputtering process usually dominates the former one, because E_s is usually much smaller than E_d.
- *Heating:* Phonons heat your specimen and heat is a major source of damage to polymers and biological tissue.

Other important mechanism is electrostatic charging of materials induced by the incident electron beam. Unlike scanning electron microscopy (SEM), charging in TEM/STEM is mainly caused by the ejection of secondary and Auger electrons into vacuum.

Radiation damage is thought to depend on the energy absorbed by the target and it's mass. The measure of the amount of radiation, the Gray, is thus defined as absorption of one joule of ionizing radiation by one kilogram of matter (1Gy = 1 J/kg). In TEM/STEM, however, almost all the incident electrons pass through thin specimen (only a negligible portion of the electrons can be scattered laterally, and eventually absorbed by specimen after multiple scattering). So, the energy deposited in specimens through inelastic scattering

is only a small portion of the total energy carried by the incident beam. Therefore, it is more convenient to use the number of incident electrons during an exposure (the flow in C/cm^2 or e/nm^2), as the "electron dose", to represent the strength of irradiation in TEM/STEM.

In the literature, this "dose" is defined as the product of electron current density (dose rate) and illumination (or exposure) time (A/m^2 or e/nm^2 s). Generally, it has been considered that there is a "dose threshold", also known as the "critical dose" or "characteristic dose", for each beam-sensitive material, below which beam damage is negligible. The well-known low-dose technique commonly used for biological materials is based on this idea. For a given total dose there are two ways to achieve a low-dose condition in TEM/STEM: either by lowering the electron current density (dose rate) or by shortening the exposure time. The former is widely used in the low-dose technique, but the disadvantage is its low signal-to-noise ratio (SNR) and poor resolution. The latter may increase the SNR, but the very short acquisition time may induce artifacts due to the finite detector response time. Differences in image quality for the same dose but different exposure times (dose rate effects) are known as "reciprocity failure" [50].

$$\frac{1A}{1m^2} \times \frac{1C/s}{1A} \times \frac{6.242x10^{18}\ e}{1C} \times \frac{1m^2}{1x10^{18}\ nm^2} = \frac{6.242\ e}{nm^2 \cdot s}$$

2.3.1.3   The Transmission Electron Microscope

A Transmission Electron Microscope can be divided into three essential systems: the illumination system, the objective lens/stage, and the imaging system. (1) The illumination system comprises the gun and the condenser lenses and its role is to take the electrons from the source and transfer them to your specimen. (2) The objective lens and the specimen holder/stage system is the heart of the TEM. Here is where all of the beam-specimen interactions take place and the two fundamental TEM operations occur, namely, the creation of the various images and diffraction patterns (DPs) that are subsequently

magnified for viewing and recording. (3) The imaging system uses several lenses to magnify the image or the DP produced by the objective lens and to focus these on the viewing screen or computer display via a detector, CCD, or TV camera. The main components of a typical TEM are shown in Figure 2.5.
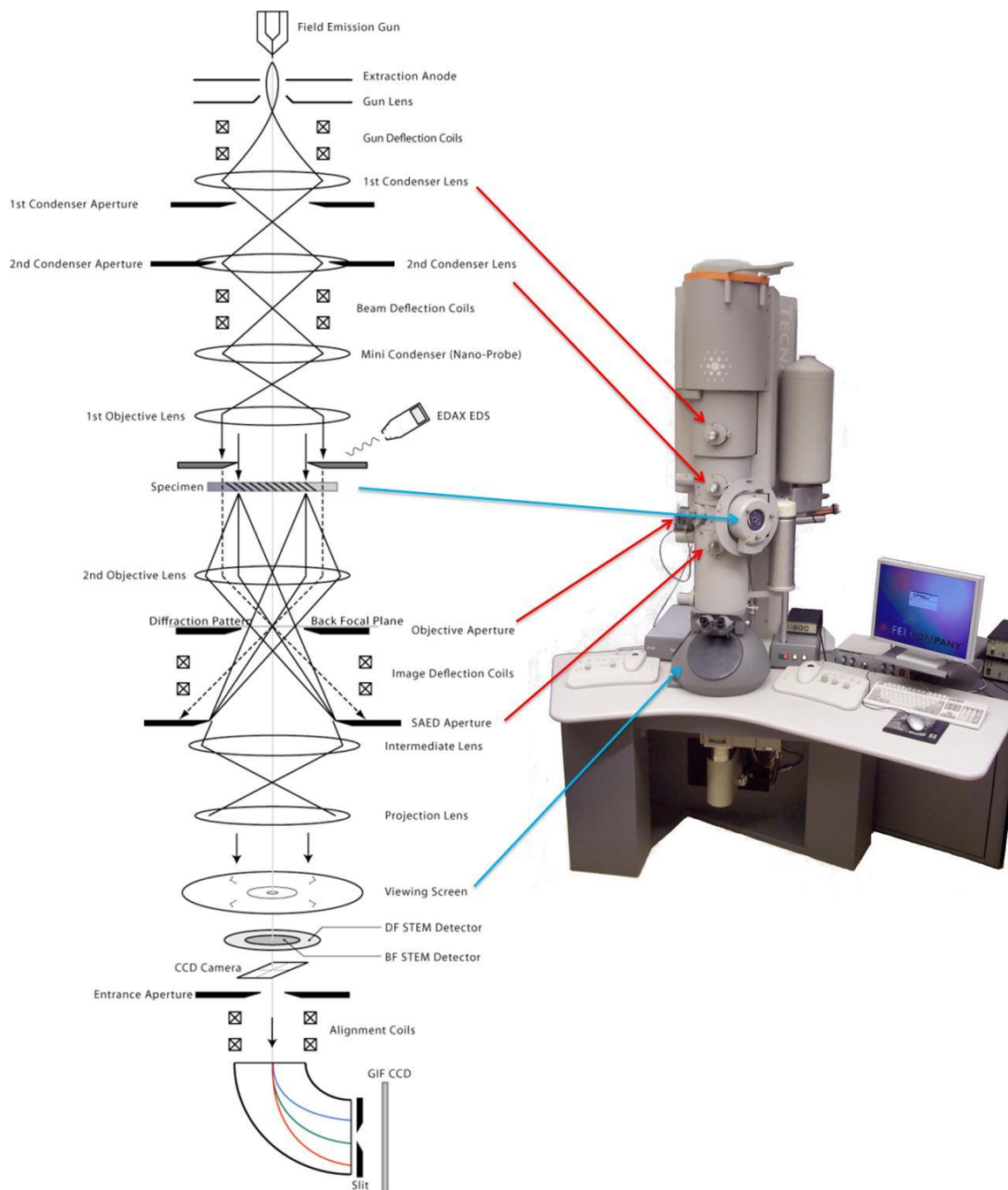
Figure 2.5 - Ray diagram of a Transmission Electron Microscope showing the main components. Adapted from [1].

Below, a brief description of the main components:

- *Electron gun:* The electrons are generated in the source and accelerated to the required energy; to be transferred to the sample.

- *Condenser system:* A set-up of different magnetic lenses and apertures makes it possible to get either a parallel beam (micro probe for TEM image and selected-area diffraction, SAD) or a convergent beam with selected convergence angles (nano probe for STEM and convergent beam electron diffraction, CBED). Furthermore, the beam can be scanned (STEM) or tilted (DF-TEM).

- *Objective lens:* Most important lens in the microscope since it generates the first intermediate image, the quality of which determines the resolution of the final image.

- *Diffraction/intermediate lens:* Switching between imaging and diffraction mode.

- *Projective lenses:* Further magnification of second intermediate image (image or diffraction pattern, respectively).

- *Image observation:* Images and diffraction pattern can directly be observed on the viewing screen in the projection chamber or via a TV camera mounted below the microscope column. Images can be recorded on negative films, on slow-scan CCD cameras or on imaging plates.

- *Vacuum system:* Because of strong interactions of electron with matter, gas particles must be absent in the column. The required high vacuum is maintained by a vacuum system typically comprising a rotary pump (pre-vacuum pump), a diffusion pump and one or more ion getter pumps.

The objective lens takes the electrons emerging from the exit surface of the specimen, disperses them to form a DP in the back-focal plane (BFP), and recombines them to form an image in the image plane (1. intermediate image, in Figure 2.6). Thus, diffraction pattern and image are simultaneously present in the TEM. It depends on the focusing of the intermediate lens which of them appears in the plane of the second intermediate image and magnified by the projective lens system on the viewing screen.
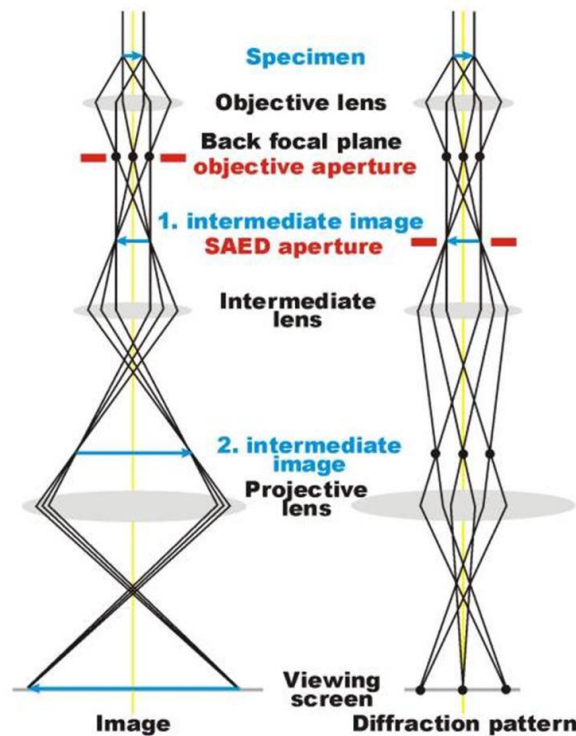
Figure 2.6 - Ray diagram showing the two basic operation modes in TEM: Image mode, and Diffraction mode. From http://www.microscopy.ethz.ch

In imaging mode, an objective aperture can be inserted in the back focal plane to select one or more beams that contribute to the final image (Bright-Field (BF), Dark-Field (DF), High-Resolution TEM (HRTEM)). For selected area electron diffraction (SAED), an aperture in the plane of the first intermediate image defines the region of which the diffraction is obtained. Ray diagrams, and comparison images, showing how the objective aperture is used to produce BF, DF and HRTEM images are shown in Figure 2.7.

In the BF mode, an aperture is placed in the BFP of the objective lens which allows only the direct beam to pass. In this case, the image results from a weakening of the direct beam by its interaction with the sample. Therefore, mass-thickness and diffraction contrast contribute to image formation: thick areas, areas in which heavy atoms are enriched and crystalline areas appear with dark contrast (Figure 2.7a).
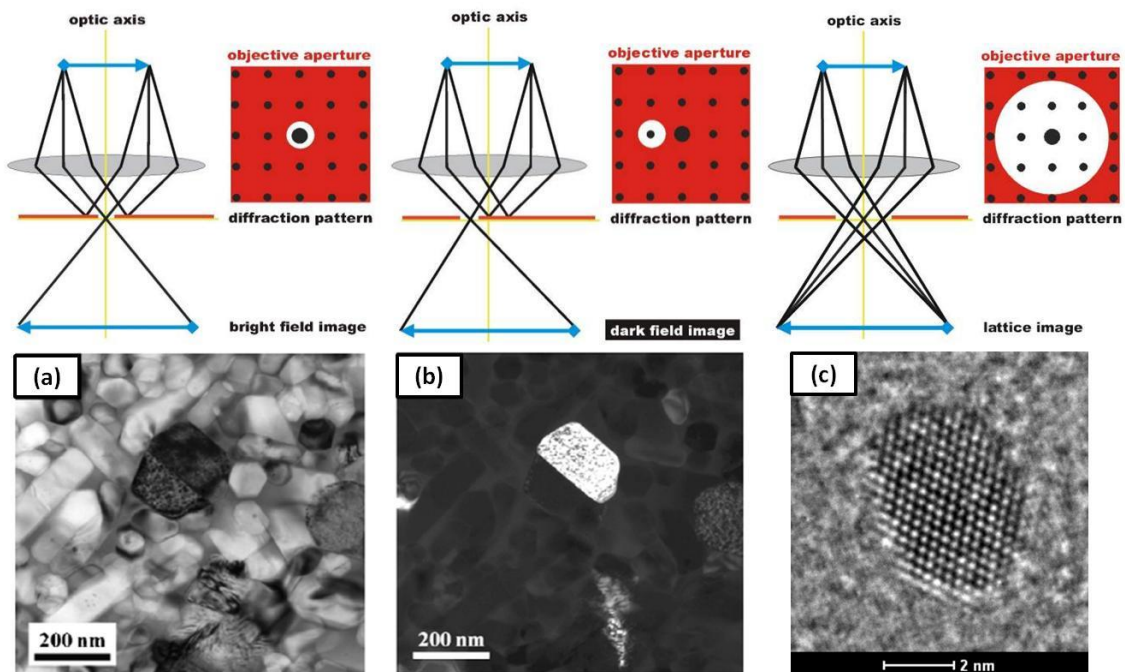
Figure 2.7 - Ray diagram showing how objective aperture is used to produce (a) BF, (b) DF, and (c) HRTEM images. Adapted from http://www.microscopy.ethz.ch

In DF mode, the direct beam is blocked by the aperture while one or more diffracted beams are allowed to pass the objective aperture (Figure 2.7b). Since diffracted beams have strongly interacted with the specimen, very useful information is present in DF images, e.g., about planar defects, stacking faults or particle size.

To obtain lattice images, a large objective aperture has to be selected that allows many beams including the direct beam to pass. The image is formed by the interference of the diffracted beams with the direct beam (phase contrast). If the point resolution of the microscope is sufficiently high and a suitable crystalline sample oriented along a zone axis, then HRTEM images are obtained (Figure 2.7c).

2.3.1.4   Fast Fourier transforms of images

Fourier analysis of a periodic function refers to the extraction of the series of sines and cosines which when superimposed will reproduce the function. This analysis can be expressed as a Fourier series. The fast Fourier

transform is a mathematical method for transforming a function of time (or space) into a function of frequency (or reciprocal space).

We can also think of an image as a varying function, however, rather than varying in time it varies across the two-dimensional space of the image. In a grey scale digital image the pixels each have a value between 0 and 255 representing the darkness of that pixel. So the darkness, or intensity, of that pixel, is a function of the horizontal and vertical coordinates giving the location of that pixel. We can think of the image as an undulating landscape, with the height of the landscape given by the value of the pixel. Figure 2.8 shows a black and white digital photograph and the image function of the same digital photograph, with the gray value u(x, y) plotted as the height of the surface over the (x, y)-plane.
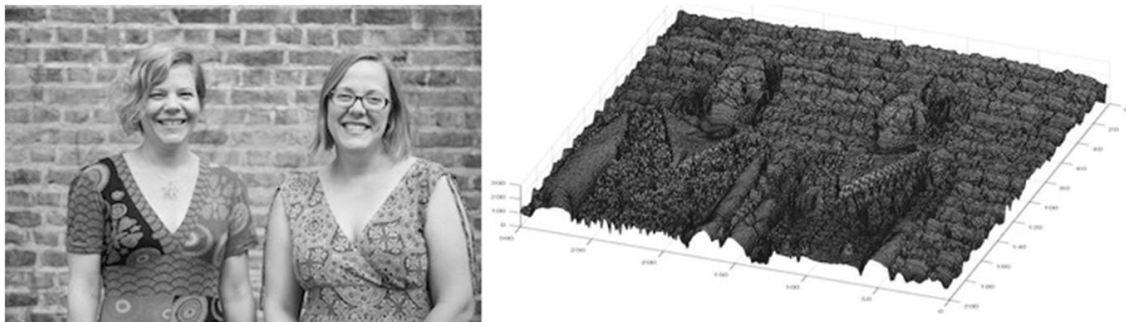
Figure 2.8 - Black and white digital photograph and its representation as a function of gray intensity. From https://plus.maths.org

As we showed earlier, the formation of an HRTEM image requires the use of an aperture large enough to include both the transmitted beam and at least one diffraction beam, in which the transmitted beam provides a reference phase of the electron wavefront. As a result, HRTEM images are interference patterns between the transmitted and diffracted electron waves from the specimen.

The contrast of a HRTEM image comes from the interference in the image plane of the electron wave with itself. Above the sample, the wave of an electron can be approximated as a plane wave incident on the sample surface. As it penetrates the sample, it is attracted by the positive atomic potentials of

the atom cores, and channels along the atom columns of the crystallographic lattice. At the same time, the interaction between the electron wave in different atom columns leads to diffraction. This is known as Fraunhofer diffraction; since a plane incident wave was considered and the diffraction pattern is observed at an infinite distance. Since a wave emitted by a point (atom) becomes planar at large distances.

To change the observation plane of the diffraction pattern from infinite to the back focal plane, a lens is used. So the objective lens in a TEM performs as a Fourier transform.
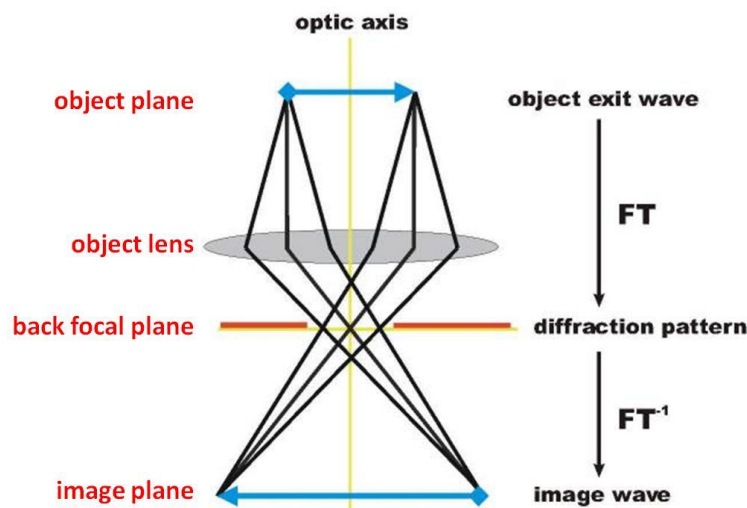
Figure 2.9 - Ray diagram showing the formation of a TEM image. From http://www.microscopy.ethz.ch

In an electron diffraction pattern formed in the back focal plane of the objective lens of an electron microscope, the electron wavefunction is the Fourier transform of the electron wavefunction on the exit face of the crystal, and Bragg's law gives the positions of the diffraction spots. However, the electron wavefunction in the image plane in an electron microscope is the inverse Fourier transform of the wavefunction in the diffraction plane (multiplied by a contrast transfer function to take into account apertures and lens aberrations). So the electron wavefunction in the image plane is the inverse Fourier transform of the Fourier transform of the electron wavefunction on the exit face of the crystal, which has the periodicity of the real-space crystal lattice.

This means that the electron wavefunction in the image plane is the same (multiplied by a contrast transfer function) as in the exit of the crystal.

Since the digital gray image obtained in the image plane is a replica of the crystal, we can repeat the previous process; this time not with lens, but using a mathematical tool in the image function, i.e. applying a fast Fourier transform (FFT) to the image to reveal the diffraction pattern. Figure 2.10 and Figure 2.11 are an example of how, when the necessary conditions are met (a crystalline sample oriented in the zone axis, among others), the selected area electron diffraction (SAED) and the FFT are equivalent.
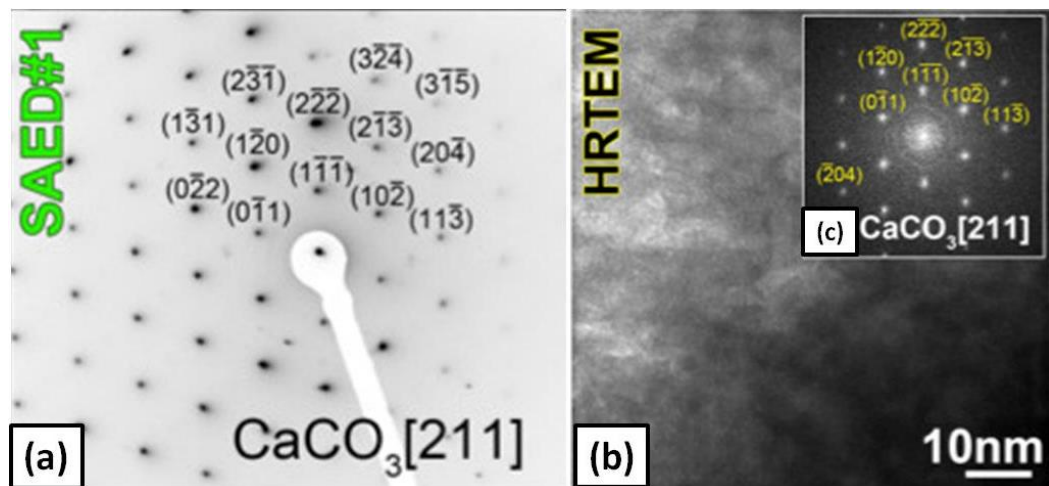
Figure 2.10 - (a) SAED, (b) Low magnification HRTEM image, and (c) FFT of b), of crystalline biogenic calcite. From [51]
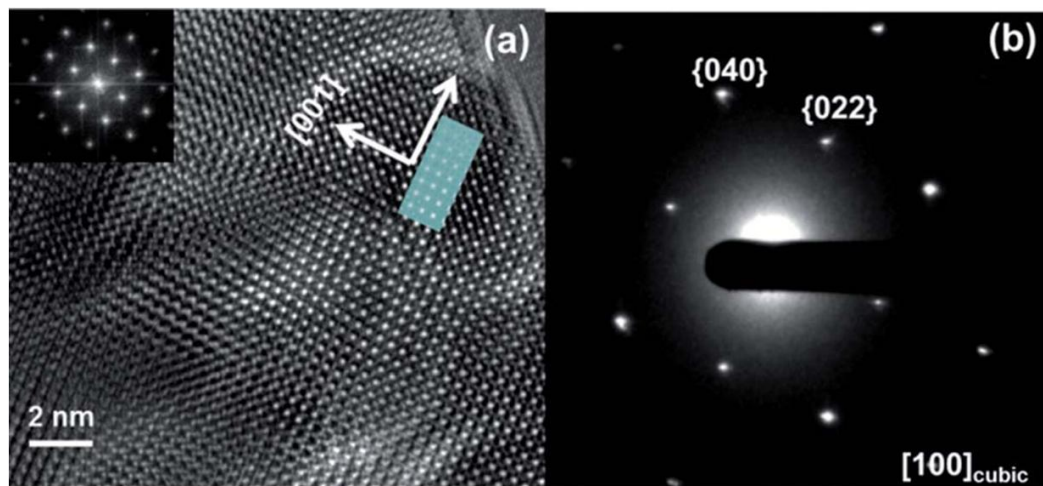
Figure 2.11 - (a) HRTEM image, inset the FFT, and (b) SAED of spinel like structure of $Li_{1.2}Co_{0.1}Mn_{0.55}Ni_{0.15}O_2$. From [52]

Thus, in a crystalline sample oriented in the zone axis, the intensity distribution in a HRTEM image corresponds to the electron density distribution, which is stronger at the atomic columns positions. This means that we are visualizing the crystal structure in the real space. From this we can directly measure the lattice spacing, or apply a FFT to identify patterns of symmetrically organized atoms, i.e. crystallographic planes.

It is worth noting that, as the spots on the FFT come from a mathematical treatment to an image, and not from a diffraction phenomenon, some artifacts in the image that are not directly related with the diffraction process itself (like electromagnetic noise in the microscope, noise in the CCD camera, among others) can generate other spots that are not related with a satisfied diffraction condition in a crystalline sample.

Summarizing, the FFT of a HRTEM image is a powerful tool that, like the SAED, help us to characterize, and analyze the crystal structures and crystal defects of our samples; like lattice matching, interfaces, twinning, among others.

2.3.2 Nanoparticle synthesis

"Nanoparticle synthesis refers to methods for creating nanoparticles. Nanoparticles can be derived from larger molecules, or synthesized by 'bottom-up' methods that, for example, nucleate and grow particles from fine molecular distributions in liquid or vapour phase. Synthesis can also include functionalization by conjugation to bioactive molecules." Nature.com

Although gas-phase processes are successfully employed for the low-cost production of large quantities of nanopowders, it seems that liquid-phase syntheses are more flexible with regard to the controlled variation of structural, compositional, and morphological features of the final nanomaterials. Liquid-phase routes include coprecipitation, hydrolytic as well as nonhydrolytic solgel processes, hydrothermal or solvothermal methods, template synthesis and biomimetic approaches [53].

2.3.2.1 Coprecipitation

Coprecipitation is the simultaneous precipitation of a normally soluble component with a macro-component from the same solution by the formation of mixed crystals, by adsorption, occlusion or mechanical entrapment. An adsorbate is an impurity that is weakly bound (adsorbed) to the surface of the precipitate. An occlusion occurs when an adsorbed impurity gets physically trapped inside the crystal as it grows. Coprecipitation reactions involve the simultaneous occurrence of nucleation, growth, coarsening, and/or agglomeration processes.

As a brief overview, coprecipitation reactions tend to exhibit the following characteristics: (i) The products of precipitation reactions are generally sparingly soluble species formed under conditions of high supersaturation. (ii) Such conditions dictate that nucleation will be a key step of the precipitation process and that a large number of small particles will be formed. (iii) Secondary processes, such as Ostwald ripening and aggregation, will dramatically affect the size, morphology, and properties of the products. (iv) The supersaturation conditions necessary to induce precipitation are usually the result of a chemical reaction [54].

2.3.2.2 Sol-Gel

The sol-gel process involves conversion of monomers into a colloidal solution (sol) that acts as the precursor for an integrated network (or gel) of either discrete particles or network polymers. Typical precursors are metal alkoxides.

The sol-gel process can be characterized by a series of distinct steps.

- Step 1: Formation of stable solutions of the alkoxide or solvated metal precursor (the sol).

- Step 2: Gelation resulting from the formation of an oxide- or alcohol-bridged network (the gel) by a polycondensation or polyesterification reaction that results in a dramatic increase in the viscosity of the solution. If so desired, the gel may be cast into a mold during this step.

- Step 3: Aging of the gel (syneresis), during which the polycondensation reactions continue until the gel transforms into a solid mass, accompanied by contraction of the gel network and expulsion of solvent from the gel pores. Ostwald ripening and phase transformations may occur concurrently with syneresis. The aging process of gels can exceed 7 days and is critical to the prevention of cracks in gels that have been cast.

- Step 4: Drying of the gel, when water and other volatile liquids are removed from the gel network. This process is complicated due to fundamental changes in the structure of the gel. The drying process has itself been broken into four distinct steps: (i) the constant rate period, (ii) the critical point, (iii) the first falling rate period, and (iv) the second falling rate period. If isolated by thermal evaporation, the resulting monolith is termed a xerogel. If the solvent is extracted under supercritical or near-supercritical conditions, the product is an aerogel.

- Step 5: Dehydration, during which surface-bound M−OH groups are removed, thereby stabilizing the gel against rehydration. This is normally achieved by calcining the monolith at temperatures up to 800 °C.

- Step 6: Densification and decomposition of the gels at high temperatures (T > 800 °C). The pores of the gel network are collapsed, and remaining organic species are volatilized. This step is normally reserved for the preparation of dense ceramics or glasses.

2.3.2.3 Hydrothermal and Solvothermal synthesis

Hydrothermal processing can be defined as any heterogeneous reaction in the presence of aqueous solvents or mineralizers under high pressure and temperature conditions to dissolve and recrystallize (recover) materials that are relatively insoluble under ordinary conditions. Byrappa and Yoshimura define hydrothermal as any heterogeneous chemical reaction in the presence of a solvent (whether aqueous or non-aqueous) above the room temperature and at pressure greater than 1 atm in a closed system [55,56]. Analogously, solvothermal means any chemical reaction in the presence of a non-aqueous solvent or solvent in supercritical or near supercritical conditions.

Some solvothermal processes indeed involve supercritical solvents. Most, however, simply take advantage of the increased solubility and reactivity of metal pressures without bringing the solvent to its critical point. In any event, solvothermal processing allows many inorganic materials to be prepared at temperatures substantially below those required by traditional solid-state reactions. Unlike the cases of coprecipitation and sol-gel methods, which also allow for substantially reduced reaction temperatures, the products of solvothermal reactions are usually crystalline and do not require post-annealing treatments.

2.3.2.4 Solvent-Controlled Synthesis

The solvent-controlled synthesis is considered a simpler approach, compared to other synthesis process. The starting reaction mixture generally just consists of a metal oxide precursor and a common organic solvent, and on the other hand the synthesis temperature is lower, typically in the range of 50 to 200°C. However, without any doubts the main advantage of the solvent-controlled (or surfactant-free) synthesis methods lies in the improvement of product purity. Surface-adsorbed surfactants not only influence the toxicity of nanoparticles, but also lower the accessibility of the nanoparticle surface in catalytic and sensing applications.

In the solvent-directed approaches the organic solvent can act as reactant as well as controlling agent for particle growth and thus makes the use of surfactants superfluous. However, the detailed role of the organic species in these approaches is rather complex. On the one hand they provide the oxygen for the formation of the metal oxide, and on the other hand they act as capping agent, which binds to the particle surface, and thus limits the particle growth, and influences morphology and assembly behavior.

Although a rapidly expanding variety of metal oxide nanoparticles has been synthesized by solvent-directed procedures during the last few years, only a relatively limited number of reaction systems were used for this purpose. Suitable metal oxide precursors include metal halides, acetates, acetylacetonates, alkoxides, and in cases of more complex oxides also mixtures

thereof, and the solvents range from oxygen-containing alcohols, ketones and aldehydes, to oxygen-free solvents like amines, acetonitriles or toluene [53].

The most frequently used reaction systems for metal oxide nanoparticle in non-aqueous and surfactant-free synthesis are:

i)   reaction of metal halides with alcohols,

ii)   metal alkoxides, acetates and acetylacetonates with alcohols,

iii)   metal alkoxides with ketones or aldehydes, and

iv)   metal acetylacetonates with amines and nitriles

The reaction of metal halides, in general metal chlorides, with alcohols presumably represents the simplest non-aqueous approach to metal oxide nanoparticles, and it can, in the most cases, be performed by simple "beaker" chemistry using an oil bath as heating tool. Metal chlorides like $FeCl_3$, $VOCl_3$, $CoCl_2$, WCl_6, $SnCl_4$, $HfCl_4$, $NbCl_5$, $TaCl_5$ and $TiCl_4$ readily react with various alcohols to the corresponding metal oxides. The metal halide - alcohol system with its low reaction temperature is particularly useful and versatile in cases where either surface functionalization of the nanoparticles with organic ligands is desired, or where biomimetic reaction principles based on the use of organic templates have to be applied in order to tailor crystal morphology.

The reaction of metal halides with alcohols almost always results in metal oxide nanoparticles with halide impurities. To avoid this contamination synthesis routes based on the reaction of metal acetates, acetylacetonates, or alkoxides with alcohols provide a halide-free alternative.

A detailed description of the chemical reaction mechanisms can be found elsewhere [53].

2.3.3 Solvents

A solvent is a liquid that serves as the medium for a reaction. Its two main purposes are:

1)   (Non-participatory) *to dissolve the reactants*: Polar solvents are best for dissolving polar reactants (such as ions); nonpolar solvents are best for dissolving nonpolar reactants (such as hydrocarbons).

2)   Participatory: as a source of acid (proton), base (removing protons), or as a nucleophile (donating a lone pair of electrons).

What does "polar" and "non-polar" mean?

- *Polar solvents* have large dipole moments ("partial charges"); they contain bonds between atoms with very different electronegativities, such as oxygen and hydrogen.

- *Non polar solvents* contain bonds between atoms with similar electronegativities, such as carbon and hydrogen (think hydrocarbons, such as gasoline). Bonds between atoms with similar electronegativities will lack partial charges; it's this absence of charge which makes these molecules "non-polar".

There are two common ways of measuring this polarity. One is through measuring a constant called "dielectric constant" or permitivity. The greater the dielectric constant, the greater the polarity (water = high, gasoline = low). A second comes from directly measuring the dipole moment.

There's a final distinction to be made and it is a source of confusion. Some solvents are called "protic" and some are called "aprotic".

- *Protic solvents* have O-H or N-H bonds. Why is this important? Because protic solvents can participate in hydrogen bonding, which is a powerful intermolecular force. Additionally, these O-H or N-H bonds can serve as a source of protons (H+).

- *Aprotic solvents* may have hydrogens on them somewhere, but they lack O-H or N-H bonds, and therefore cannot hydrogen bond with themselves.
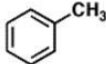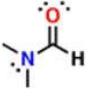
There are 3 types of solvents commonly encountered: nonpolar, polar aprotic, and polar protic.

Nonpolar solvents: These solvents have low dielectric constants (<5) and are not good solvents for charged species such as anions. However diethyl ether (Et_2O) is a common solvent for Grignard reactions; its lone pairs are Lewis basic and can help to solvate the Mg cation.

"**Borderline" Polar aprotic solvents:** These solvents have moderately higher dielectric constants than the nonpolar solvents (between 5 and 20). Since they have intermediate polarity they are good "general purpose" solvents for a wide range of reactions. They are "aprotic" because they lack O-H or N-H bonds. For our purposes they don't participate in reactions: they serve only as the medium.

Polar aprotic solvents: These solvents all have large dielectric constants (>20) and large dipole moments, but they do not participate in hydrogen bonding (no O-H or N-H bonds). Their high polarity allows them to dissolve charged species such as various anions used as nucleophiles (e.g. CN^-, HO^-, etc.). The lack of hydrogen bonding in the solvent means that these nucleophiles are relatively "free" in solution, making them more reactive. For general purposes these solvents do not participate in the reaction.

Polar protic solvents: Polar protic solvents tend to have high dielectric constants and high dipole moments. Furthermore, since they possess O-H or N-H bonds, they can also participate in hydrogen bonding. These solvents can also serve as acids (sources of protons) and weak nucleophiles (forming bonds with strong electrophiles).

Nonpolar solvents		Dielectric constant	Dipole Moment
	Pentane	1.8	0.00 D
	Hexane	1.9	0.00 D
	Cyclohexane	2.0	0.00 D
	Benzene	2.4	0.00 D
	Toluene	2.3	0.36 D
$CHCl_3$	Chloroform	4.8	1.04 D
$CH_3CH_2-\ddot{O}-CH_2CH_3$	Diethyl ether (Et_2O)	4.3	1.15 D

"borderline" Polar aprotic		Dielectric constant	Dipole Moment
CH_2Cl_2	Dichloromethane	9.1	1.60 D
	Tetrahydrofuran (THF)	7.5	1.75 D
	Ethyl acetate	6.0	1.78 D

Polar aprotic solvents		Dielectric constant	Dipole Moment
	Acetone	21	2.88 D
	N,N-Dimethylformamide (DMF)	38	3.82 D
$H_3C-C{\equiv}N\colon$	Acetonitrile (MeCN)	37	3.92 D
	Dimethyl sulfoxide (DMSO)	47	3.96 D

Polar Protic Solvents		Dielectric constant	Dipole Moment	
:NH₃	Ammonia	~25	1.4	D
CH₃ H–Ö–C–CH₃ CH₃	t-Butanol	12	1.7	D
H–Ö–CH₂CH₂CH₃	n-Propanol	20	1.68	D
H–Ö–CH₂CH₃	Ethanol	25	1.69	D
H–Ö–CH₃	Methanol	33	1.70	D
O ‖ H–Ö–C–CH₃	Acetic acid	6.2	1.74	D
H–Ö–H	Water	80	1.85	D

Figure 2.12 - Most common solvents. From
https://www.masterorganicchemistry.com

2.4 Related works in *in situ* electron microscopy

Hiruyasu Saka reported the formation of SiC *via* solid-state reaction between single crystalline Si and poly-crystalline Graphite, the reaction of the particles take place in a HRTEM mounted in a heated holder at 1400°C (in vacuum) [3]. During the reaction can be appreciated that the whole region of the graphite reacted with the Si and a SiC crystal was formed; with the aid of the HRTEM the new phase formed and his lattice spacing could be identified and reported. In the Figure 2.13 can be appreciated how the lattice spacing decrease after the reaction to 0.252 nm of cubic β-SiC.
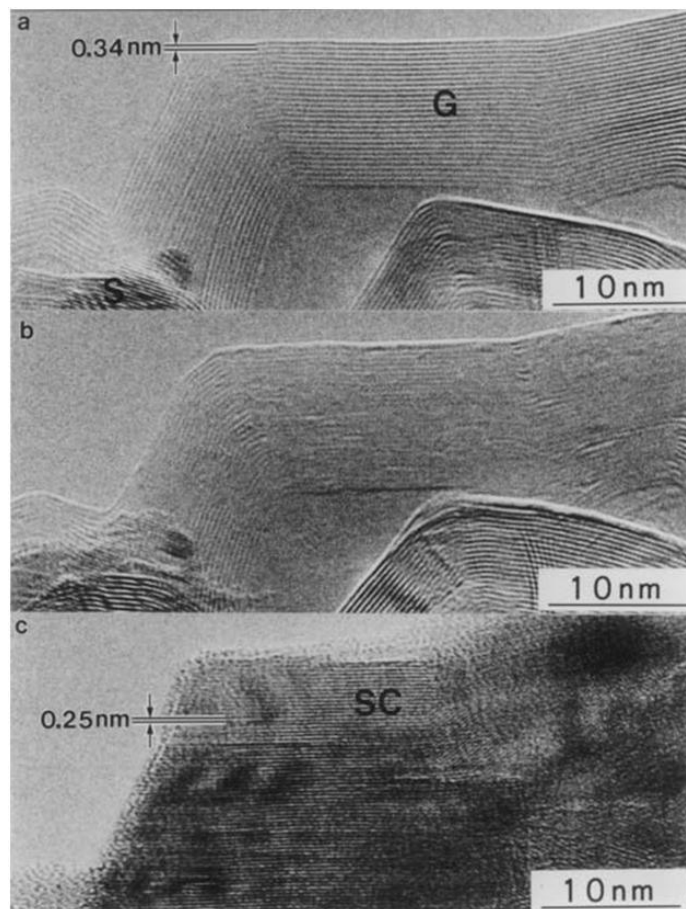
Figure 2.13 - HREM image showing the process by which SiC is formed *via* solid-state reaction between Si and graphite at 1400°C [3].

Lee and Zuo studied the mechanism of growth and phase transformation in nanometer-sized titania powders [57], in his observations anatase nanoparticles was calcined at a certain temperature when the phase transformation from anatase to rutile was archived the nucleated rutile grows fast by absorbing neighboring anatase particles (Figure 2.14). Rutile grows until there are no anatase particles near the rutile particle.
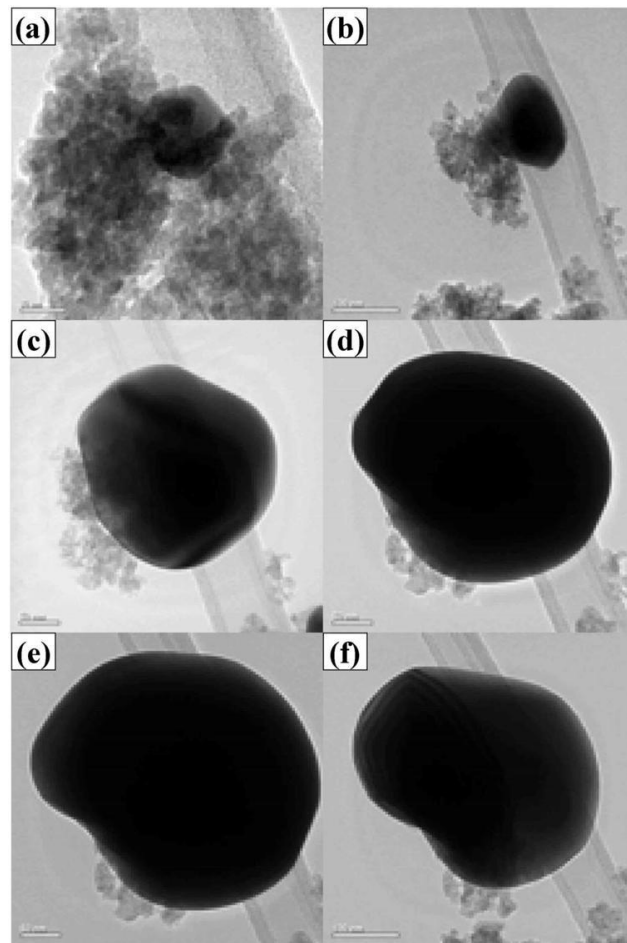
Figure 2.14 - *In situ* TEM observation of rutile particle growth. The TEM micrographs show the absorption of the anatase particles into a rutile particle heated at (a) 710°C, (b) 800°C (0 min), (c) 800°C (31 min), (d) 800°C (160 min), (e) 800°C (211 min), and (f) after cooling [57].

Dongsheng Li *et al.* built a fluid cell to perform *in situ* observations of oriented attachment of iron oxyhydroxide nanoparticles using a HRTEM, at room temperature. The particles undergo continuous rotation and interaction until they find a perfect lattice match. Different phenomena after the oriented attachment were reported (and recorded in video), the formation of twins and stacking faults at particle-particle boundaries, the move of two edge dislocations leaving a large defect-free structure, and the recrystallization of a misaligned particle trapped between two adjacent particles. The results show that after attachment, the boundary advanced by monomer addition [58]. Figure 2.15

shows a sequence of images from a movie showing typical dynamics of the attachment process.
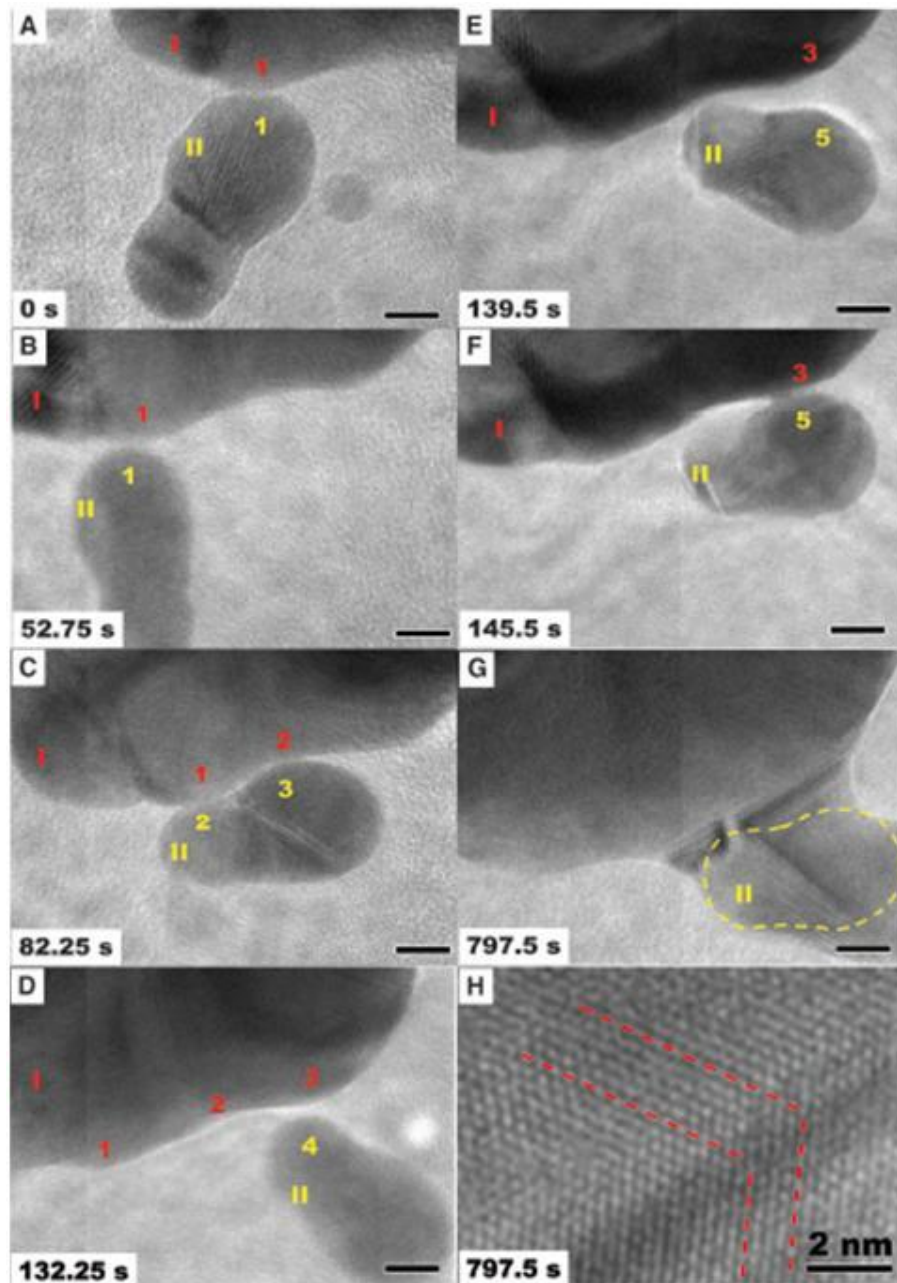
Figure 2.15 - (A to G) The surfaces of particles I and II made transient contact at many points and orientations (points 1-1, 1-2, 2-3, and 3-4) before finally attaching and growing together (points 3-5). (H) High-resolution image of interface in (G) showing twin structure (an inclined twin plane). The yellow dashed line in (G) shows the original boundary of the attached particle [58].

Chao Zhu *et al.* fabricated their own liquid cell, by sandwiched a droplet of the solution into two TEM copper grids with formvar stabilized carbon support films face-to-face. They performed *in situ* tests at room temperature on oriented attachment of gold nanoparticles [59]. Alike Dongsheng Li *et al.*; Chao Zhu *et al.* report how gold nanoparticles rotate randomly and get closer, interacting until they share a common {111} orientation and a sudden contact occurs resulting in a oriented attachment. Figure 2.16 shows a sequence of images from a video, red lines stand for {111} facets and green ones for {100} facets. Dashed lines depict the relative angle between the {111} facets of the two particles. The direction of movement of the particles (approaching and rotation) is denoted by blue arrows.
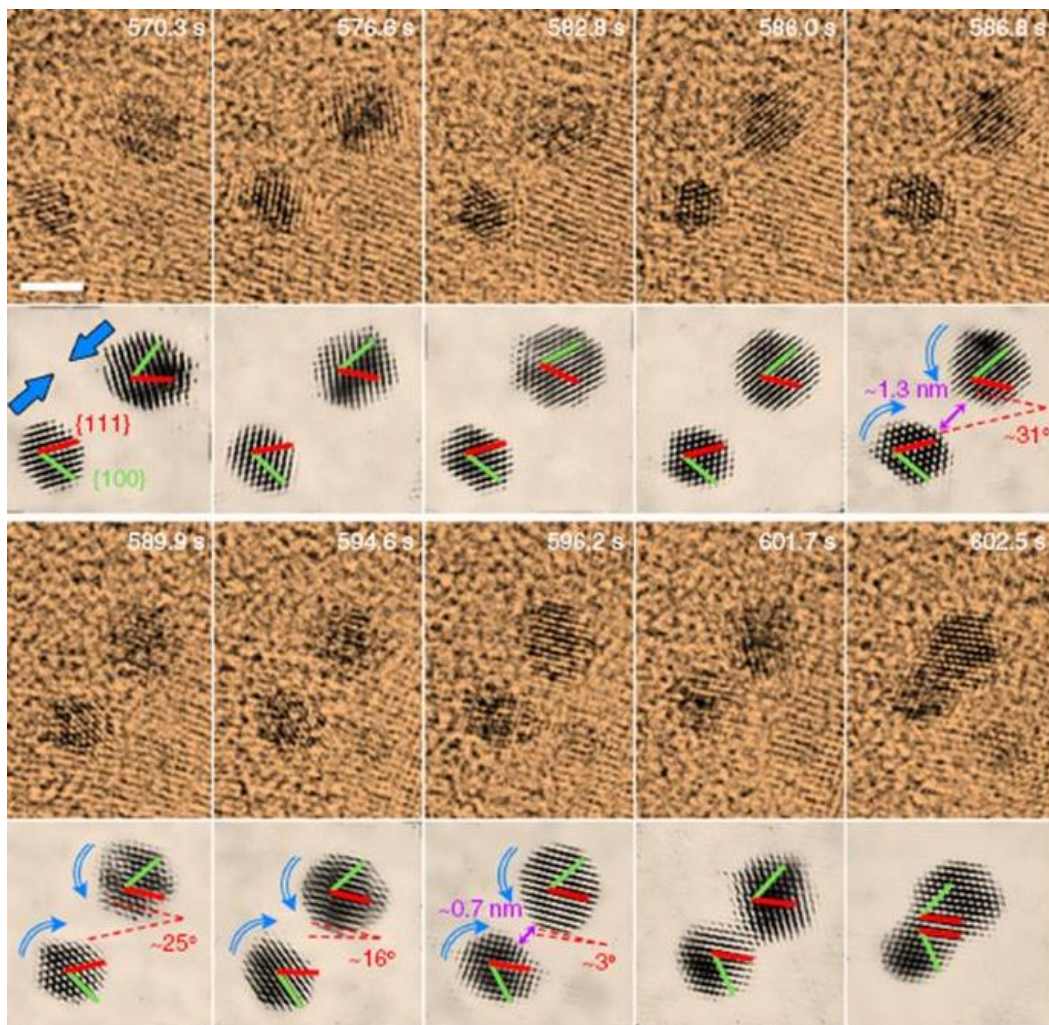
Figure 2.16 - Imaging of oriented attachment at atomic level of gold nanoparticles. Scale bar 2 nm [59].

Different studies have previously proposed growth by oriented attachment in ceria, from nanocrystals to nanorods [60–63], although there have not been found any direct observation of this phenomenon.

Sharma *et al.* studied the reduction of Pr doped ceria by the loaded of Ni nanoparticles during *in situ* experiments in an Environmental Transmission Electron Microscope (ETEM) with a flow of hydrogen gas at 420°C, observing a reduction zone of ceria (+3.2) in the Ni near zones different from the oxidation state (+3.5) in Ni remote regions, this was attributed to gas-nickel-ceria interactions at the three-phase boundary [64].   The chemical changes were recorded with Electron Energy Loss Spectroscopy (EELS).
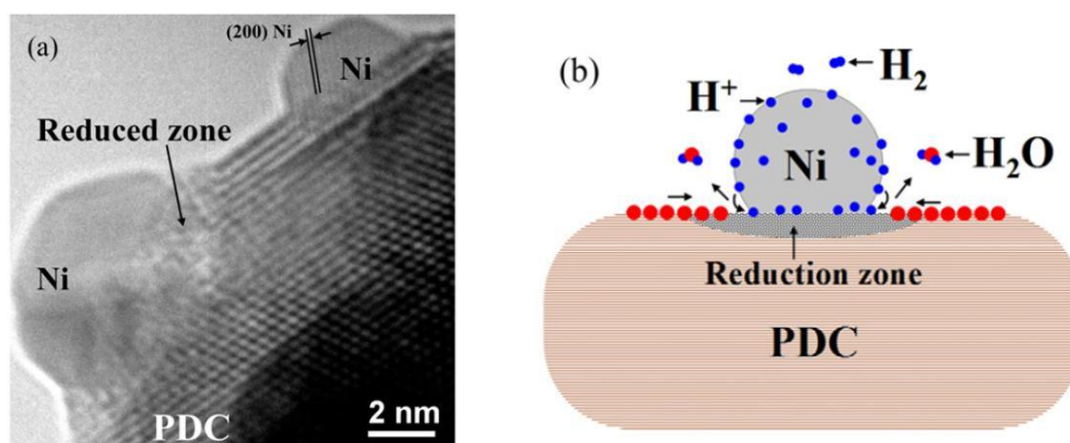
Figure 2.17 - a) HRTEM image of Ni-Pr doped ceria interface in H_2 environment at 650°C, and b) mechanism of reduction zones formation: hydrogen spillover from Ni to Pr doped ceria [64].

Hiruyasu Saka, Lee and Zuo, and Sharma *et al.* illustrated that nanoparticles react during *in situ* TEM experiments in different ways like reaction between nanoparticles, phase transformations and growth, and changes in the oxidation states.   Even more importantly, these reactions can be documented and understood with the aid of TEM techniques.

Pérez-Omil *et al.* combined the HRTEM and atomic-resolution High-Angle Annular Dark Field (HAADF) scanning transmission electron microscopy techniques to investigate structural changes in ceria-zirconia mixed oxides

($Ce_{0.68}Zr_{0.32}O_2$) thermally aged at 1223K [65]. They reported the formation of a pyrochlore superstructure with the aid of the intensity profiles of an HAADF image recorded along the rhombi edge and along a parallel line passing through is center (Figure 2.18a-d). As is known, the HAADF image contrasts strongly depend on the average Z value in the atomic columns; in the case of the ceria-zirconia the difference between the Ce (Z=58) and Zr (Z=40) would allow atomic identification of the cationic columns.
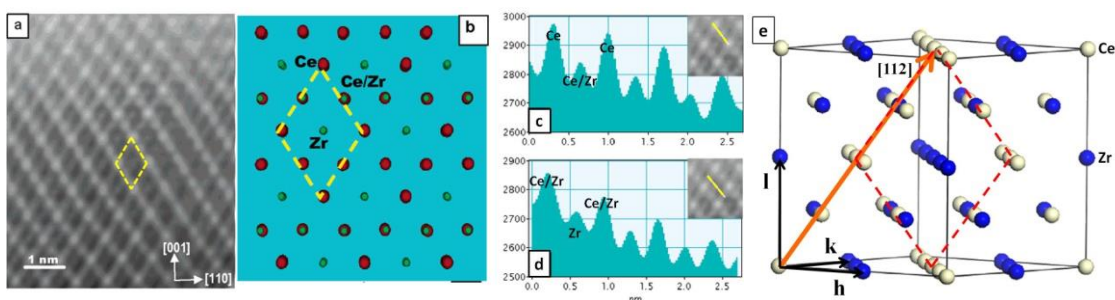
Figure 2.18 - a) Experimental atomic-resolution HAADF image of the ceria-zirconia oxide. b) Projection in the ($1\bar{1}0$) plane of a structural model of the pyrochlore superstructure. c) Intensity profiles along the rhombi edge, and d) along a parallel line passing through the rhombi center. e) Schematic diagram of pyrochlore structure, the orange arrow indicate the [112] direction, where the intensity profiles were taken. (a), (b), (c) and (d) Adapted from Pérez-Omil [65], and (e) Crozier [66].

Crozier *et al.* made *in situ* studies in ETEM with H_2 in synthesized ceria-zirconia powders with nominal composition $Ce_{0.5}Zr_{0.5}O_2$, they use EELS to show that some particles are redox-active and other not. In the actives ones the Ce is in +4 oxidation state at 450°C and at 650°C is reduced to +3 (in 0.5 Torr of H_2) during heating and then return to their +4 state upon cooling, this particle maintains a predominantly cubic fluorite structure; but the inactive ones never recover their state and remains in +3 even at room temperature, in this particles the HRTEM image and electron diffraction pattern show the presence of a pyrochlore type superstructure [66]. In pyrochlore, Ce and Zr cations order along the [$1\bar{1}0$] direction giving rise to individual columns of Ce and Zr (Figure 2.18e). It may be possible to obtain similar reactions by heating in vacuum but

higher temperatures would be required, fortunately the same structure was reported in vacuum by Pérez-Omil *et al.* around 950°C.

The reason to report the same phase transformation at different compositions is due to changes in the stoichiometry of Oxygen, $Ce_{1-X}Zr_XO_{2-\delta}$ ($0.5 \geq \delta \geq 0$). In the ceria-zirconia system the ZrO_2-CeO_2 will transform to ZrO_2-$CeO_{1.5}$ under certain experimental conditions. The Ce^{+4} cations will reduce to Ce^{+3} cations at increasing temperature in reducing atmosphere (H_2, CO, NH_3), under a vacuum of 10^{-1}-10^{-2} Pa (10^{-6}–10^{-7} bar), in inert atmospheres (Ar, He), as well as under a low oxygen partial pressure (1.4 Pa at 1400 °C). S. Huang *et al.* have thermodynamic predictions of phases in these nonstoichiometric ceria-zirconia systems [67], but in his calculations only monoclinic and hexagonal structures appear and these is not what is observed in the TEM.

Pérez-Omil *et al.*and Crozier *et al.* found a new atomic arrangement at high temperature who present different catalytic properties, i.e. a phase transformation. Although both authors reported the same superstructure the nominal composition in the two studies is significantly different ($Ce_{0.68}Zr_{0.32}O_2$ vs $Ce_{0.5}Zr_{0.5}O_2$) and is not clear how only a 32 mol % can be replaced one to one in the cubic structure, could be the zirconia preferentially absorbed by some particles? And which is the minimum amount of zirconia required to form this superstructure? These questions can be addressed by *in situ* TEM techniques.

Cordeiro *et al.* shown dissolution and formation of CeO_2 nanocube-like with {100} exposed facets on an amorphous carbon film, the *in situ* TEM was performed in a FEI Tecnai F20 provided with a Gatan 268 single-tilt heating holder [68]. The dissolving dynamics of the ceria appear dissimilar depending on the initial facet proportion, in nanocrystals with facet ratio far from 1 the smaller facet (S3) decreases in size more slowly than the larger facet (S4), Figure 2.19b. In contrast, nanocrystals with facets sizes (S1,S2) of about same length, the facets shrink homogeneously; that is, the facet size ratio (S1/S2) remains nearly constant with a value around unit, Figure 2.19a.
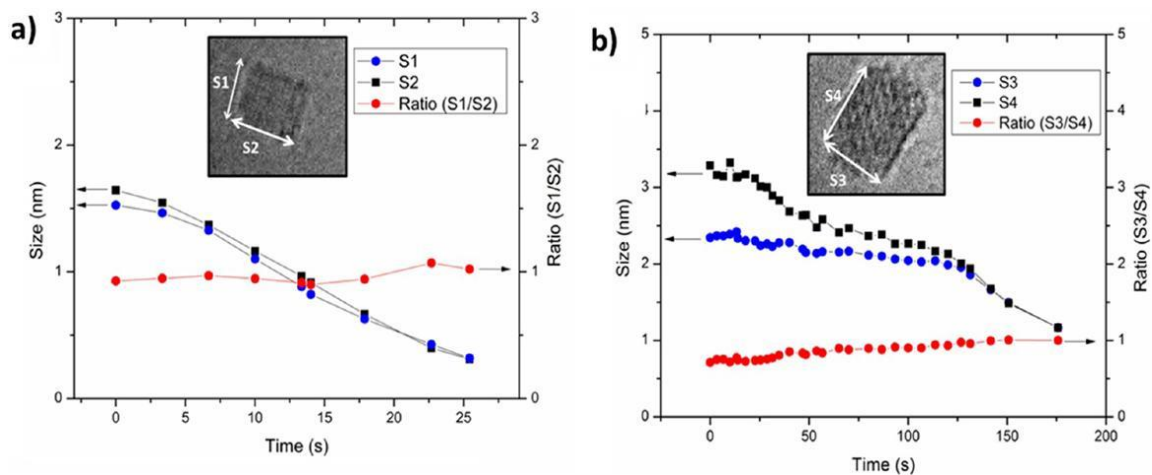
Figure 2.19 - a)CeO$_2$ Nanocubes side size and the side ratio evolution: smaller nanocrystal; b) larger nanocrystal [68].

Zhou *et al.* correlated the catalytic performance and the exposed crystal planes of CeO$_2$ nanorods and nanoparticles (with fluorite structure) using HRTEM [69]. The ceria nanoparticles obtained by the precipitation method predominantly expose the very stable and least reactive {111} planes, whereas the nanorods synthesized by a solution-based hydrothermal method exhibit the less stables reactive planes {110} and {001}. In this study the CeO$_2$ nanoparticles with higher surface area (62.4 m^2/g) were inferior catalysts than the CeO$_2$ nanorods with lower surface area (50.1 m^2/g) who were more active and demonstrate more CO conversion (Figure 2.20). It is normally to speak that lower surface area is better for catalytic activity, but this is not strictly true since as demonstrated is more important have well-defined reactive planes.
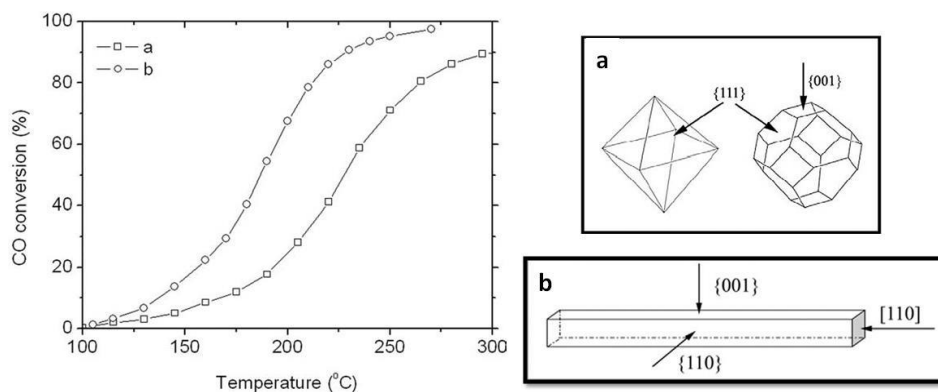
Figure 2.20 - Percentage conversion versus temperature plots for the oxidation of CO over CeO$_2$ a) nanoparticles and b) nanorods [69].

From Cordeiro *et al.* and Zhou *et al.* can be abstracted that not only the stoichiometry plays an important role when we facing reactions at nanoscale but also the geometry, the aspect ratio, exposed planes, among others.

3 MATERIALS AND METHODOLOGY

3.1 Synthesis of the nanocrystals

Three different methods were employed for the synthesis of the nanoparticles, the Hydrothermal method for the first synthesis of the ceria [68,70], the Solvothermal method using benzyl alcohol for the zirconia and the tin oxide [71–73], and the Solvent-controlled synthesis with oleyl alcohol for the second synthesis of the ceria. The TEM samples were be prepared by dropping the colloid onto a TEM grid with support carbon film (~3nm), and dried naturally. The following reagents were used:

Table 3.1 - Reagents used for the production of nanocrystals

Oxide	Reagent	Formula
Ceria [CeO$_2$]	Cerium (III) nitrate	Ce(NO$_3$)$_3$
	Toluene	C$_6$H$_5$CH$_3$
	Oleic acid [OAc]	CH$_3$(CH$_2$)$_7$CH=CH(CH$_2$)$_7$COOH
	tert-butylamine	(CH$_3$)$_3$CNH$_2$
	Cerium(III) acetylacetonate hydrate [Ce(acac)$_3$]	Ce(C$_5$H$_7$O$_2$)$_3$ x H$_2$O
	oleyl alcohol [OLA]	CH$_3$(CH$_2$)$_7$CH=CH(CH$_2$)$_7$CH$_2$OH
	oleylamine [OAm]	CH$_3$(CH$_2$)$_7$CH=CH(CH$_2$)$_7$CH$_2$NH$_2$
	Acetone	(CH$_3$)$_2$CO
Zirconia [ZrO$_2$]	Zirconium(IV) propoxide	Zr(OCH$_2$CH$_2$CH$_3$)$_4$
	Benzyl alcohol	C$_6$H$_5$CH$_2$OH
	Tetrahydrofuran [THF]	C$_4$H$_8$O
Tin Oxide [SnO$_2$]	Tin(IV) chloride	SnCl$_4$
	Benzyl alcohol	C$_6$H$_5$CH$_2$OH
	Tetrahydrofuran [THF]	C$_4$H$_8$O

3.1.1 Synthesis of Ceria nanocrystals

Hydrothermal method in two-phase conditions: In a typical synthesis, 60 mL of 0.017 mol/L cerium (III) nitrate aqueous solution, 60 mL of toluene, 5 mL of oleic acid and 0.60 mL tert-butylamine were transferred to a 150 mL Teflon-lined stainless-steel autoclave, respectively, without stirring. The sealed autoclave was heated at 10°C/min to 180°C in a conventional oven for 24 h, and then cooled to room temperature. The organic part of the mixture was removed and centrifuged once to remove the solid impurities. Subsequently, the nanocrystals were precipitated by the addition of ethanol and submitted to a several cycles of ultra-sonication, centrifugation, and solvent exchange. The

resulting nanocrystals can be dispersed in non-polar solvents (e.g. toluene, hexane, chloroform).

Cerium (III) nitrate (99% trace metals basis, and 99.99% trace metals basis), Cerium(III) acetylacetonate hydrate, oleyl alcohol (OLA) (technical grade, 85%), oleylamine (OAm) (technical grade, 70%) were purchased from Sigma-Aldrich. The cerium acetylacetonate hydrate (Ce(acac)$_3$) was dried on a vacuum oven at 60°C for 24 hours, obtaining an orange powder, straight away was stored on a glovebox with controlled atmosphere under ultrahigh purity nitrogen.

Solvent-controlled method: Within a glovebox, Ce(acac)$_3$ (0.437 g, 1.0 mmol), OLA (15 mL, 40.3 mmol), and OAm (0.47 mL, 1.0 mmol) were added without stirring respectively. The amount of OAm varies from 0 to 5.0 mmol, depending on the synthesis. The flask was sealed and taken out of the glove-box, the solution was mixed in a hotplate magnetic-stirrer at 80°C for 30 min; a dark brown transparent solution was obtained. Then, it was heated to 260°C and maintained for 2 h, later cooled to room temperature, sealed and aged for 2 days. Afterwards, the solution was heated again, under stirring, to 315°C and maintained for 1 h, finally the solution was cooled to room temperature. All syntheses were made under a continuous flow of nitrogen. Subsequently, the nanoparticles were precipitated by the addition of acetone, centrifuged at 8000 rpm (≈8200 rcf). This process was performed two times. The nanoparticles could then be easily dispersed in nonpolar solvents (e.g., toluene, hexane, chloroform) and are stable for months.
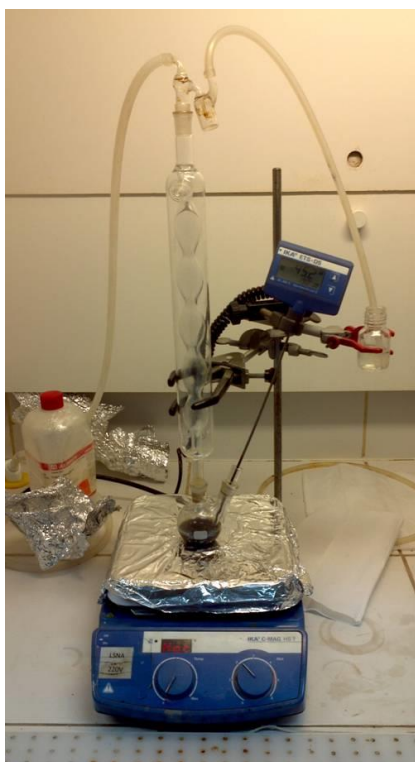
Figure 3.1 - Assembly for synthesis of ceria nanoparticles.

3.1.2 Synthesis of Zirconia nanocrystals

The ZrO_2 nanocrystals were synthesized by the solvothermal method. In a typical synthesis, 3 mL of Zirconium(IV) propoxide [$Zr(OCH_2CH_2CH_3)_4$] and 22 mL of benzyl alcohol were mixed in an autoclave with stirring. All the handling and mixing of reagents was made in a glovebox under controlled atmosphere (<ppm O_2, <ppm H_2O). The closed autoclave was heated to 230°C for 48 h under constant agitation. After this time, the system was cooled to room temperature naturally. The resulting solution was centrifuged and the derivative precipitate was separated and mixed with an aliquot portion of tetrahydrofuran (THF). The mixture was washed (centrifugation, separation and redispersion of the precipitated in ultrasonic bath) until a colloidal dispersion of ZrO_2 nanocrystals was obtained [53,74,75].

As the nanoparticles synthesized with benzyl alcohol disperse in polar solvents, such as ethanol or THF, it is necessary to change the organic layer covering the nanocrystals to disperse them in nonpolar solvents. Thus, the nanoparticles were dried to be subsequently dispersed in 25 mL of Oleic acid

(OAc), and heated on autoclave to 250°C for 24 h under constant agitation. The mixture was washed with acetone until obtain colloidal dispersion of ZrO_2 nanocrystals in organic non-polar solvents, e.g. toluene, chloroform, hexane.

3.2   Characterization techniques

3.2.1 X-Ray Diffraction

For the crystallographic analysis, by X-Ray Diffraction (XRD), aliquots of the suspensions were dried in a vacuum oven (160-260 mmHg, or 0.21-0.34 atm) at 60°C overnight. A D/Max-2500PC (Rigaku) diffractometer was used; with Cu-Kα radiation (λ = 1.5406 Å), with a horizontal rotating anode operating at 30 mA and 40 kV. The scanning speed was 2 deg/min (≈0.03 deg/second) with steps of 0.02°, in a 2θ/θ configuration. The samples were analyzed with the software X'Pert HighScore. The obtained diffractograms were compared with the JCPDS (Joint Committee on Powder Diffraction Standards) database.

3.2.2 Thermal analysis

The thermal behavior of the oxides was evaluated by thermogravimetry/differential thermal analysis (TG/DTA) measurement on a Shimadzu DTG-60H. An atmosphere of O_2 with a flux of 20 mL/min, and a heating rate of 10 deg/min was used. Between 10-15 mg of the dried sample were deposited on an α-alumina crucible for the analyses.

3.2.3 Infrared spectroscopy

A Shimadzu spectrometer in reflection mode was used. Fourier Transform Infrared (FTIR) measurements were made in the region of 400 - 4000 cm^{-1} with a resolution of 2 cm^{-1}. The dried samples were homogenously mixed with potassium bromide (KBr).

3.2.4 Transmission electron microscopy

A FEI Tecnai^{TM} G2 F20 – XTwin was used; this microscope is located on the Interdisciplinary Laboratory of Electrochemistry and Ceramics (LIEC), as a part of the Center for the Development of Functional Materials (CDFM), from the Chemistry Department at Federal University of Sao Carlos (UFSCar). Also the FEI TITAN, located in the facilities of the Brazilian Nanotechnology National Laboratory (LNNano) in the National Center of Research in Energy and Materials (CNPEM) was used.   A list of the microscopes and his main specifications are listed below (Table 3.2):

Table 3.2 - Specifications overview of the TEMs located in the UFSCar, and LNNano/CNPEM.

	HRTEM (FEI Tecnai F20)	TEM-FEG (JEM 2100F)	Aberration Corrected S/TEM (FEI TITAN Themis Cubed)
Electron Gun	Field Emission electron Gun (FEG)	Field Emission electron Gun (FEG)	X-FEG high brightness emitter gun
Acceleration Voltage	200 KV	200 KV	300 KV
Resolution	0.25 nm	0.19 nm	0.07 nm (STEM) 0.20 nm (TEM)
Image Recording		- CCD camera (Gatan)	- 4k x 4k CMOS-based CETA - Ultrascan 2k x2k CCD - GATAN Image Filter Quantum ERS
Gadgets	High Resolution Transmission Electron Microscope (HRTEM), Bright Field (BF) and Dark Field (DF) EDS	STEM, BF, DF and High Angular Annular Dark Field (HAADF) EDS Electron Energy Loss Spectroscopy (EELS)	S/TEM, BF and DF, HAADF. Gun Monochromater, Probe Cs corrector (DCOR) Super-X EDX detector (4 Silicon Drift Detectors)

For the 3D construction of the crystals that were superimposed to the TEM images, the VESTA 3 software was used [76]. The simulated particles are symmetrical, with a crystalline structure without defects, and with all crystallographic planes equidistant to the center of the particle. Oxygen atoms, and organic molecules, on the surface of the particles were not considered.

3.3 Mixture of the nanocrystals

Two different methods to mix the nanoparticles were explored, equalizing the number of particles of each oxide (50% - 50% in number of particles) or equalizing the weight (50 - 50 weight percent). Using the data of the TGAs reported on "Section 4: Results and Analysis" (Figure 4.10 and Figure 4.23) we can proceed as follow:

Table 3.3 - Mass loss, radius, and density of the CeO_2 and ZrO_2 nanoparticles.

	Remaining Mass (TGA @900°C)	Mass Loss	Mean Diameter	Density (from us-nano.com)
ZrO_2	66.9%	33.1%	4.9 ± 07 nm 4.9 x10^{-7} cm	5.89 g/cm^3 (for particles from 40 nm)
CeO_2	51.2%	48.8%	2.7 ± 07 nm 2.7 x10^{-7} cm	7.13 g/cm^3 (for particles from 10-30 nm)

As the particles have a spherical like geometry, we can approximate its volume as:

$$V_{ZrO_2} = \frac{4}{3}\pi(2.45x10^{-7}cm)^3 = 6.1601x10^{-20}cm^3$$

$$V_{CeO_2} = \frac{4}{3}\pi(1.35x10^{-7}cm)^3 = 1.0306x10^{-20}cm^3$$

Calculating the mass of one particle:

$$\delta = \frac{m}{V} \quad \rightarrow \quad m = \delta * V$$

$$m_{ZrO_2} = 5.89\frac{g}{cm^3} * 6.1606x10^{-20}cm^3 = 3.6281x10^{-19}gr$$

$$m_{CeO_2} = 7.13\frac{g}{cm^3} * 1.0306x10^{-20}cm^3 = 7.3482x10^{-20}gr$$

Weighing an aliquot (1 mL) of each dispersion, removing the mass related to the organic layer, and dividing by the mass of one particle we can obtain the number of particles in the aliquots.

$$W_{ZrO_2} = 0.0325gr/mL * (66.9\%) = 0.0217425gr \quad \rightarrow \quad \frac{0.0217425gr/mL}{3.6283x10^{-19}gr}$$

$$= 5.9925x10^{16}particles/mL$$

$$W_{CeO_2} = 0.0141gr/mL * (51.2\%) = 0.0072192gr \quad \rightarrow \quad \frac{0.0072192gr/mL}{7.3482x10^{-20}gr}$$

$$= 9.8244x10^{16}particles/mL$$

So to equalize the number of particles in the dispersion (e.g. 1x10^{15} particles), the following volumes of each aliquot must be added

$$V_{ZrO_2} = \frac{1mL * 1x10^{15}particles}{5.9925x10^{16}particles} = 0.0167mL = 16.7\mu L$$

$$V_{CeO_2} = \frac{1mL * 1x10^{15}particles}{9.8244x10^{16}particles} = 0.0102mL = 10.2\mu L$$

With this approximation, as the zirconia nanoparticles are larger (volume almost 6 times greater); the amount of ZrO_2 in the mixture would be high. When observing the sample in the TEM it is evident that although the number of particles of both oxides is equal, the ZrO_2 nanoparticles overshadow the CeO_2 and the possibility of a reaction between particles of zirconia would be greater than the possibility of a reaction between different oxides. The weight percentage of the sample with equal number of particles is shown below:

$$0.0167mL * \frac{0.0325gr}{mL} * (66.9\%) = 0.000363gr \; of \; Zr$$

$$0.0102mL * \frac{0.0141gr}{mL} * (51.2\%) = 0.0000736gr \; of \; Ce$$

$$wt\%_{ZrO_2} = \frac{0.000363gr}{(0.000363gr + 0.0000736gr)} * 100 = 83.14\%$$

$$wt\%_{CeO_2} = \frac{0.0000736gr}{(0.000363gr + 0.0000736gr)} * 100 = 16.86\%$$

With this methodology, more than 80% of the sample would be zirconia. Another approach is equalizing the weight (e.g. 0.00025gr), as shown below. Similar to the previous one, an aliquot is weighed and the organic layer is removed.

$$V_{50wt\% \, ZrO_2} = \frac{1mL * 0.00025gr}{0.0217425gr} = 0.01150mL = 11.5\mu L$$

$$V_{50wt\% \, CeO_2} = \frac{1mL * 0.00025gr}{0.0072192gr} = 0.03463mL = 34.63\mu L$$

Those volumes were added to a vial and diluted in 1 mL of Toluene. To observe the nanoparticles on the microscope, TEM grids were immersed into the dilution and dried naturally to remove the excess of toluene.

Figure 3.2 shows the mixture of the nanoparticles with 50-50 wt%. A good dispersion is observed, also the major nanoparticles (zirconia) are easily distinguishable from the smaller ones (ceria). Figure 3.3 shows a HRTEM image, inset the fast Fourier transform (FFT) of two particles, and the crystallographic planes measured. As can be seen, the errors on the measure are low, and the characterization of the oxides by HRTEM can be made successfully.
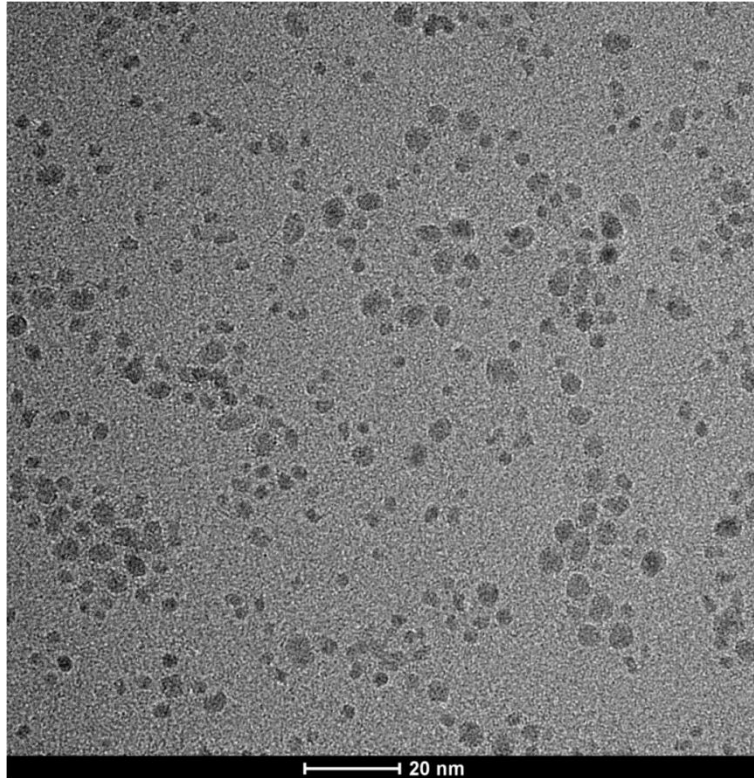
Figure 3.2 - Low magnification HRTEM of mixed nanoparticles (50-50 wt%) of CeO_2 and ZrO_2.
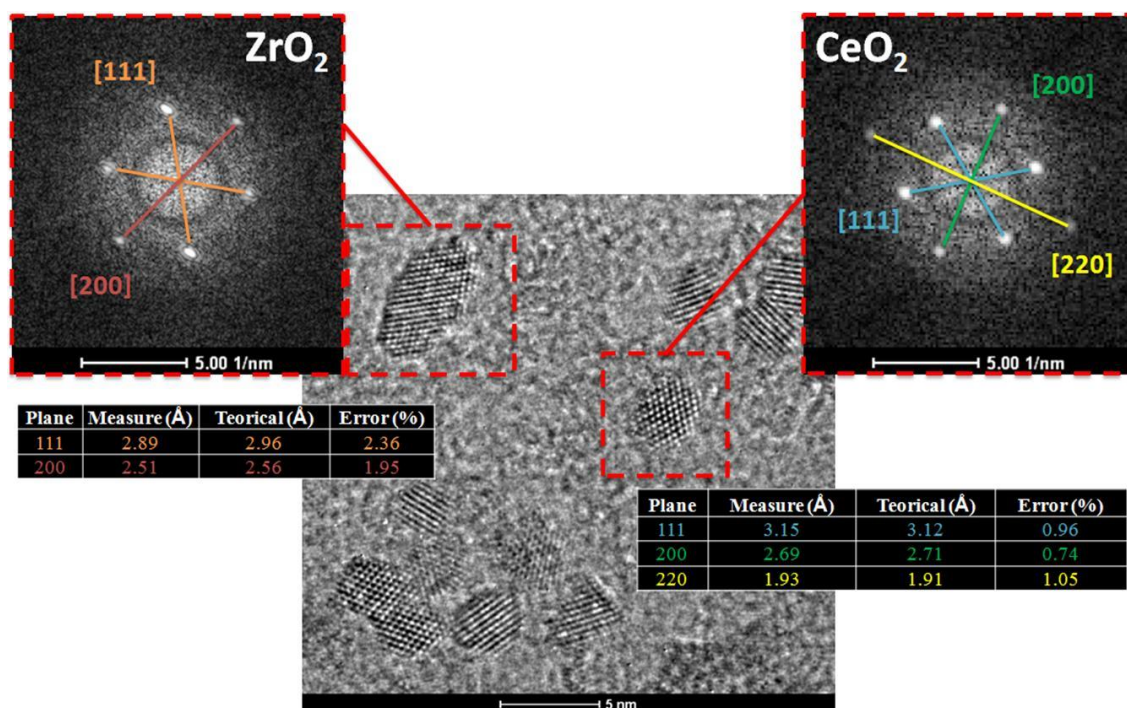
Figure 3.3 - HRTEM of mixed nanoparticles of CeO_2 and ZrO_2; inset FFT of two nanoparticles with the measurements of the crystallographic planes.

Other characterization techniques were also explored. Figure 3.4 shows High Angle Annular Dark Field (HAADF) images of the same sample; as this technique is highly sensitive to variations in the atomic number of atoms (Z-contrast), was assumed that it would be easy to differentiate cerium (Z=58) from zirconium (Z=40). Because of the difference in size between the nanoparticles of each oxide, the amount of scattered electrons by each atomic column is equivalent. Although the cerium atoms scatter more electrons, the number of atoms in a column of a nanoparticle of CeO_2 is less than in the ZrO_2, so in the end the differentiation of the two types of oxides only by the intensity of the signal was not possible, as can be seen on the following images.
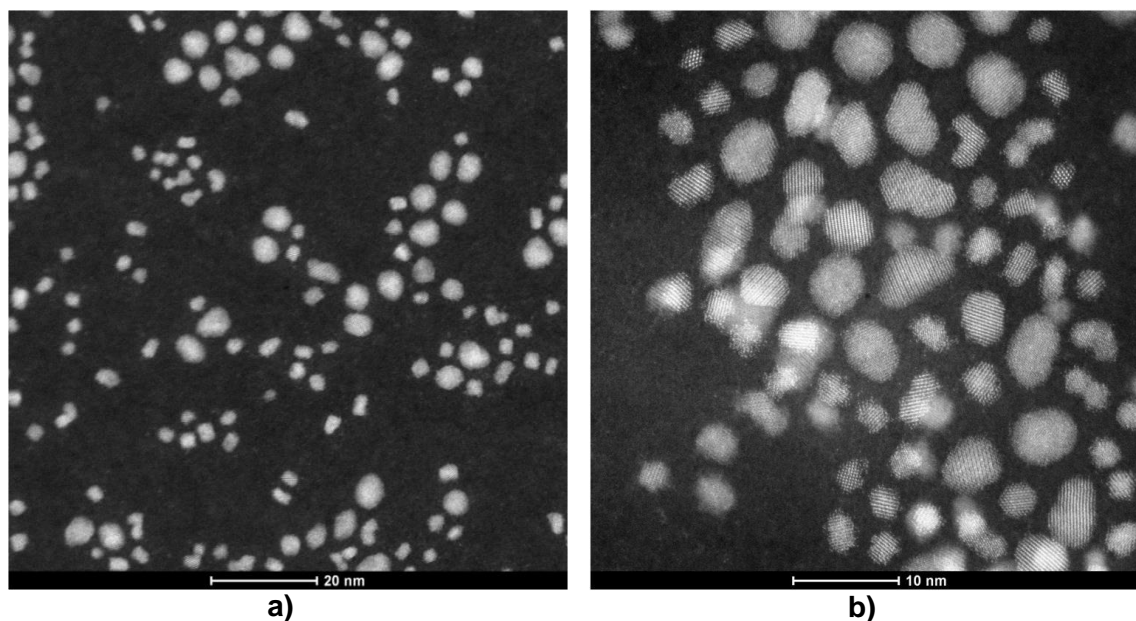
Figure 3.4 - a) and b) HAADF images of mixed nanoparticles of CeO_2 and ZrO_2.

Other technique used was the Energy-dispersive X-ray (EDX) mapping. On the Figure 3.5a can be clearly identify the particles of CeO_2 from the ZrO_2, also the technique has so good spatial resolution than the contour between neighboring particles is easily identified. The disadvantage of this technique is that require a lot of time (from 2 up to 10 minutes, in our case) to acquire an image with good resolution, so it is not possible to track the evolution of a phenomenon (i.e. sintering, diffusion, etc); only compare the before and after. The HAADF and EDX mapping were performed on the high resolution electron microscope Titan Cubed Themis (FEI) located at the LNNano (CNPEM) in Campinas, São Paulo.
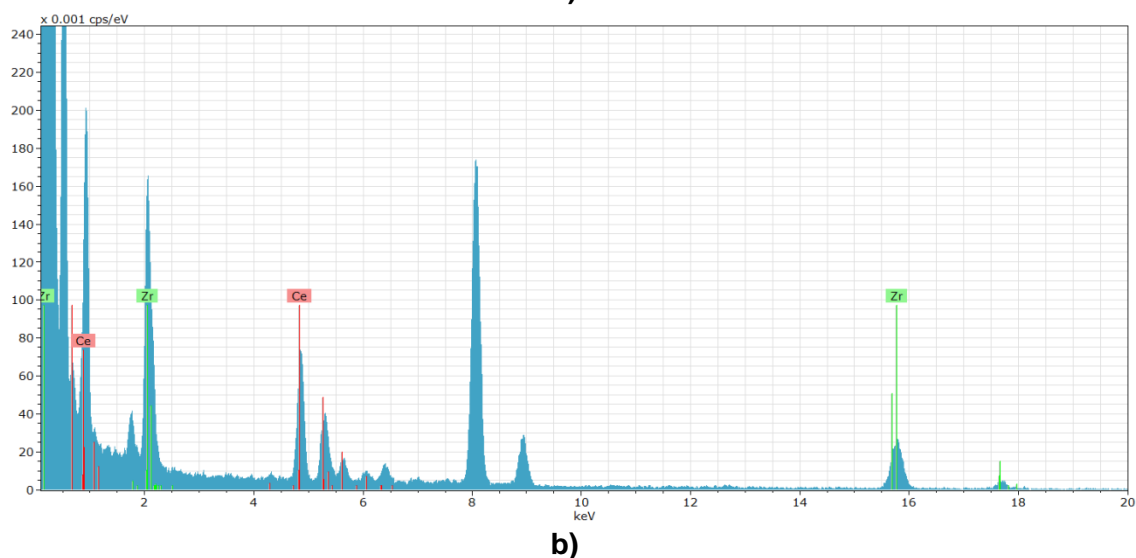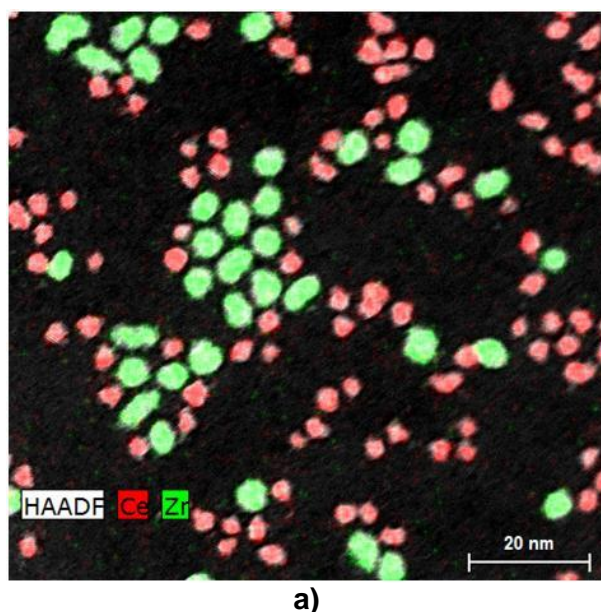
Figure 3.5 - a) EDX image mapping of mixed nanoparticles of CeO_2 and ZrO_2, and b) EDX spectrum of the scanned area.

3.4   Remotion of the organic layer

To remove the organic layer of the nanoparticles, the TEM grids were heated in a high vacuum; for this a MTI furnace with quartz tube, and a T-Station 75D turbomolecular pump were used (Figure 3.6).   Different combinations of time and temperature (i.e. heat treatments) were tested, but the one who shows better results is shown on the Figure 3.7 (5 min at 110°C, and 10 min at 210°C, with heating rates of 50°C/min).

Figure 3.6 - MTI furnace with quartz tube, and T-Station 75D turbomolecular pump.

The methodology used to remove the organic layer was the follows: 1) the sample was introduced into the furnace and a vacuum was made, 2) the vacuum valve was closed and a pure O_2 gas was introduced into the furnace chamber until reach a pressure similar to the atmospheric, 3) the gas input valve was closed and the heating start, 4) finally when the heat treatment was finish the furnace was cooled and the gas was removed.

To guarantee that no changes have occurred during the process of the remotion of the layer, the samples were observed again on the TEM before the heating tests. Figure 3.8 shows the HRTEM images of the sample before and after the remotion of the organic layer; no changes were observed. The images on the Figure 3.4 were also acquired after the remotion of the organic layer with this methodology; since the Scanning Transmission Electron Microscopy (STEM) techniques are very sensitive to contamination on the sample we can conclude that the remotion of the organic layer was successful.
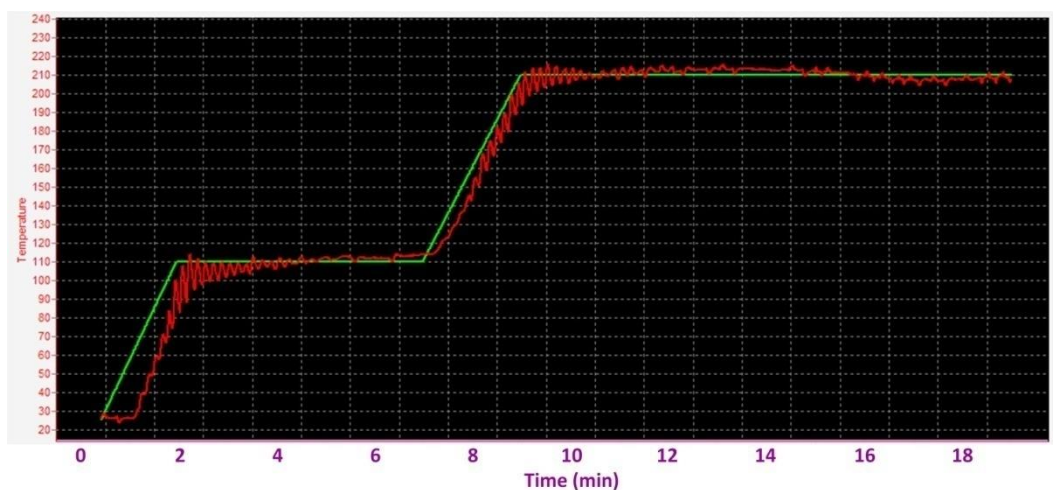
Figure 3.7 - Heat treatment curve used to remove the organic layer. Green line and red line are the set temperature, and real temperature respectively.

a)   b)
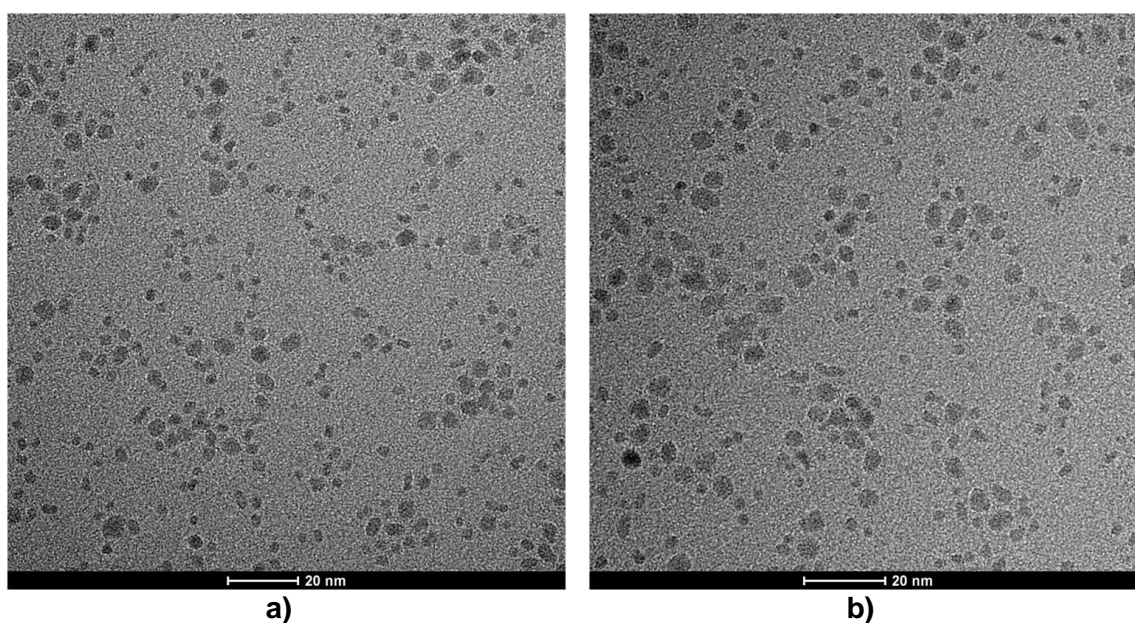
Figure 3.8 - Low magnification HRTEM images of mixed nanoparticles (CeO_2 and ZrO_2): a) before, and b) after the remotion of the organic layer.

3.5   TEM grids

As the TEM grids are heated together with the samples, it is imperative to have certain care with the material selection of the TEM grids. As an example, the material of the grids cannot react chemically with the samples, or with the holder, must be thermally stable at working temperatures, among others. On

our experiments, Cu grids coated with α-C film (3 nm thick), and Silicon windows grids with silicon nitride (Si_3N_4) membrane (10 nm thick) were used. Both have advantages and disadvantages, the Cu grids are cheaper and being thinner they allow better high resolution images with better signal to noise ratio, especially with the smallest nanoparticles, but they are unstable at temperatures around 600°C as numerous copper nanoparticles appear [77]. The main advantage of the silicon grids is they thermal stability, allowing to work at temperatures above 1300°C, being the materials of the holder and the geometry of the polar piece of the microscope the real limitations. Figure 3.9 shows some commonly used TEM grids. The metal grids can be made of copper (Cu), gold (Au), nickel (Ni), and molybdenum (Mo).

One of the main disadvantages of the nickel grids is their magnetism at room temperature, which difficult the acquisition of high quality images when the sample is near the metal parts of the grid. If the experiments are performed above the Curie temperature of nickel (355°C) this effect can be neglected, but other metal grids (such as molybdenum) are generally recommended.

Holey carbon films have many uses in microscopy but for certain applications the mesh sizes of standard TEM grids are too large to support the sample. Continuous carbon films can also be a problem due to the fact that the thin film can inelastically scatter electrons and contribute to background noise. Holey carbon films therefore are a suitable alternative. Holey carbon films have holes of various sizes up to 100μm. In addition to providing support, the increased image contrast in the regions of the holes compared to regions of film is also of benefit. Typical applications include biological and materials science and cryo-TEM. Lacey carbon films are similar to the holey carbon films in that they have open areas but because of the fine lacey mesh structure they offer a greater percentage of open area in comparison (Figure 3.10). They provide the thinnest possible support film while maintaining adequate strength and give practically no background interference in the TEM.
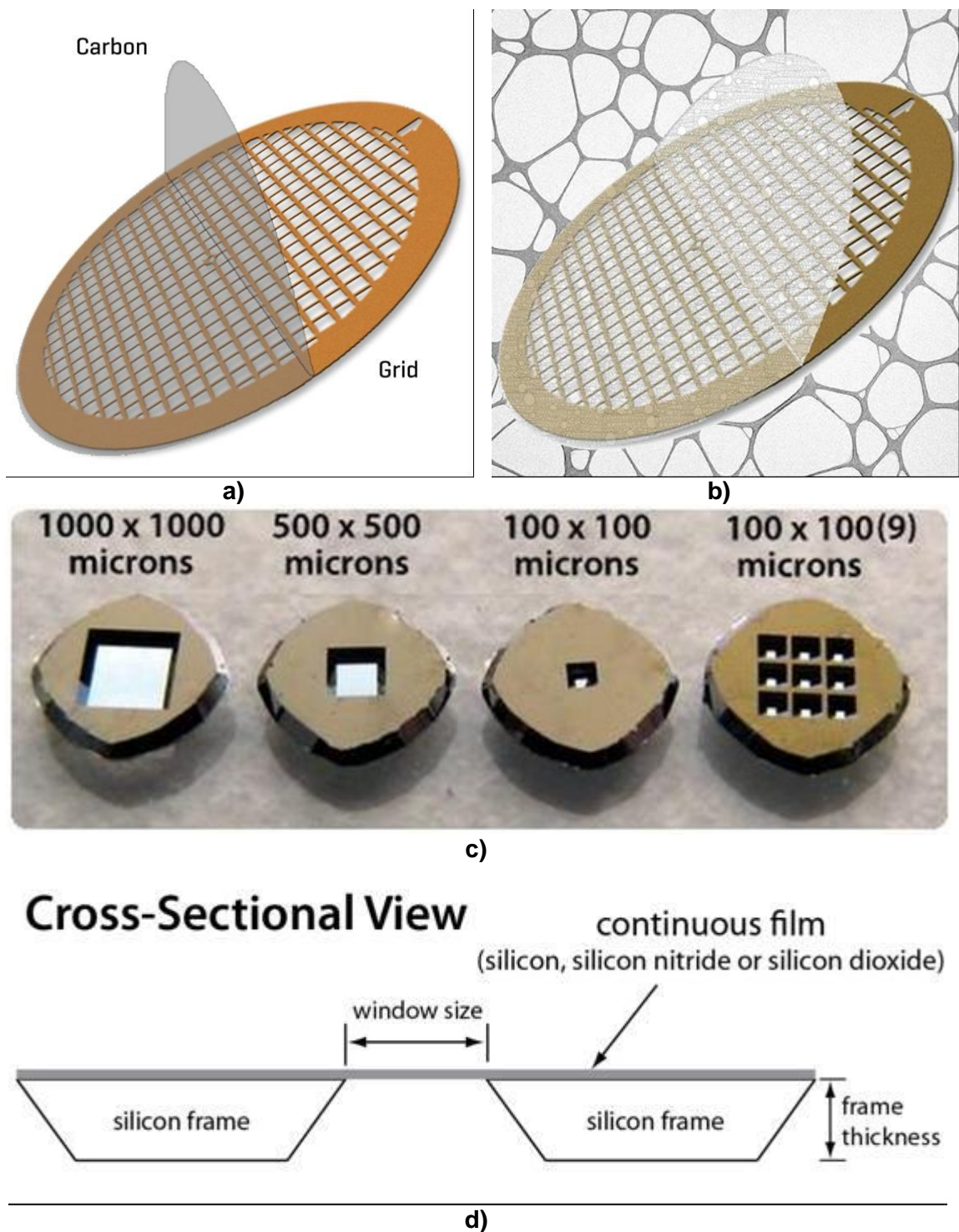
Figure 3.9 - TEM grids, a) metal grid with carbon support film, b) metal grid with lacey support film, c) silicon grid with membrane, and d) cross section of c). a) and b) from https://emresolutions.com; c) from http://www.octalab.com; d) from https://www.temwindows.com.

<p style="text-align:center;">a)   b)</p>
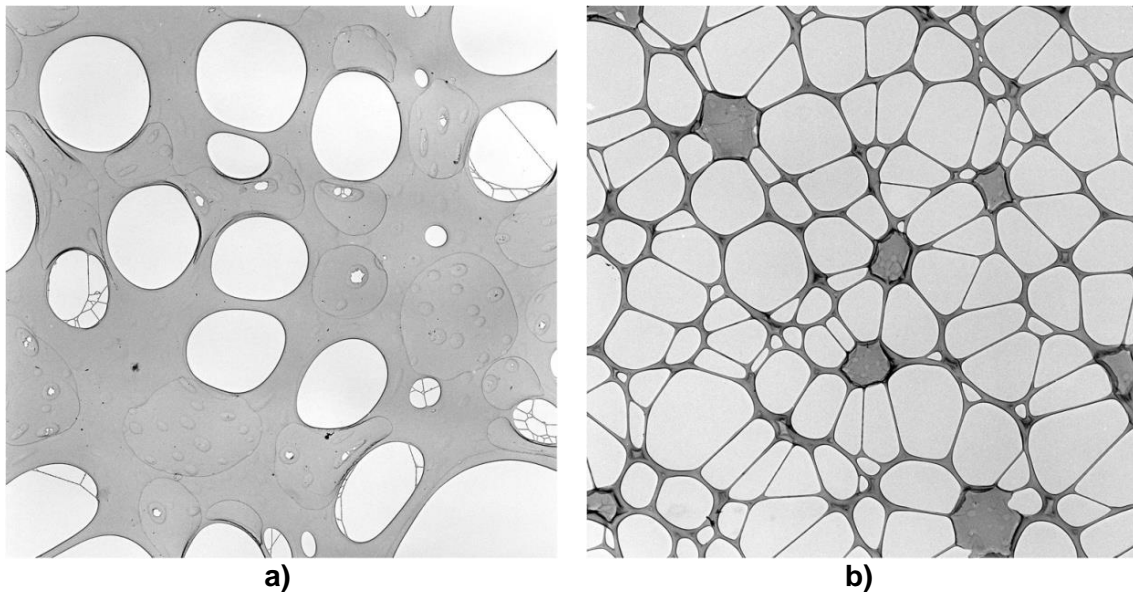
Figure 3.10 - Micrograph of: a) holey carbon film, and b) lacey carbon film. From https://emresolutions.com

Another grids available on the marked are the MEMS (Microelectromechanical systems) device that serves both as the heating element and the specimen support grid, allowing temperature cycling from room temperature to greater than 1000°C in 1 ms (a heating rate of 1 million centigrade degrees per second) and cooling at nearly the same rate. It also exhibits a return to stable operation (drift controlled by the microscope stage, not the heater) in a few seconds after large temperature variations [78]. For those grids is necessary an especial designed sample holder, and they are the most expensive in the market (Figure 3.11).
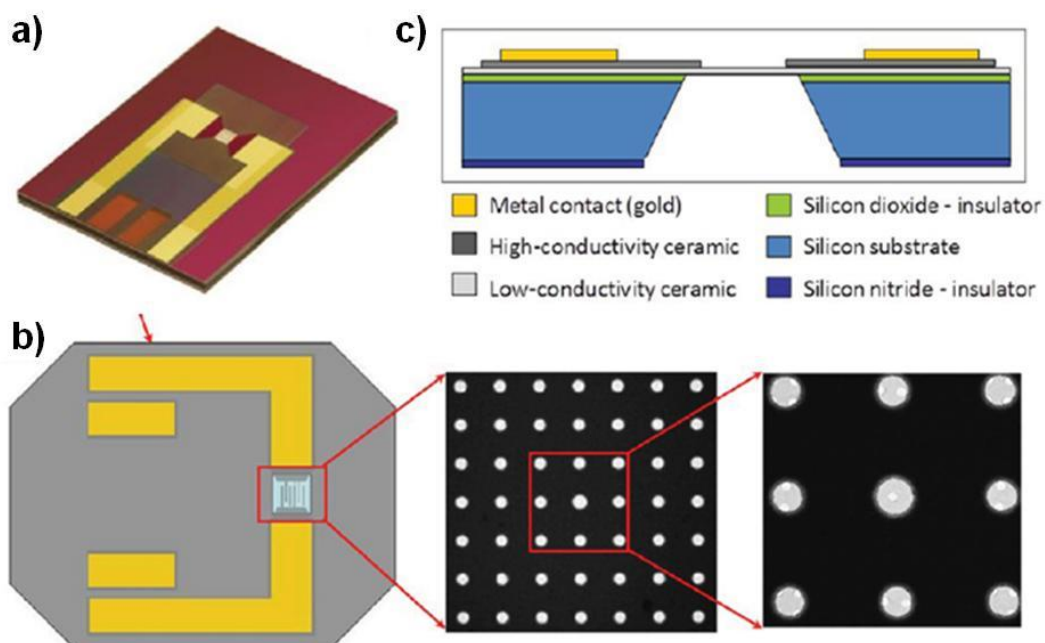
Figure 3.11 – a) E-chip device featuring a ceramic membrane used for heating. b) Schematic top view of the heater chip. The insets are low-magnification TEM images of the central region of the chip showing the pattern of holes in the low-conductivity ceramic membrane and holey carbon support film overlaying the holes in the ceramic membrane. c) Cross-section view of the chip shown in b). (Courtesy of Protochips Inc.).

3.6   *Ex situ* experiments

As the *in situ* tests are very complex and expensive; a first approach to the temperatures and reaction times between the particles will be carried out through *ex situ* tests. The *ex situ* tests were made in the furnace shown in Figure 3.6, at pressures around 10^{-6} Torr, to simulate the high vacuum conditions inside the column of the microscope (~10^{-6} - 10^{-9} Torr).

3.7   *In situ* TEM experiments at high temperature

A FEI Tecnai^{TM} G2 F20 – XTwin was used; this microscope is located on the Interdisciplinary Laboratory of Electrochemistry and Ceramics (LIEC), as a

part of the Center for the Development of Functional Materials (CDFM), from the Chemistry Department at Federal University of Sao Carlos (UFSCar). For the *in situ* tests, a Gatan 628 single tilt heating holder will be used, the maximum temperature is 900°C, and 1300°C, for Inconel and Tantalum furnace respectively (on our experiments we used the Tantalum furnace). Figure 3.12 shows the heating holder and temperature control system. For all tests, a heating rate of 50°C/min was used.
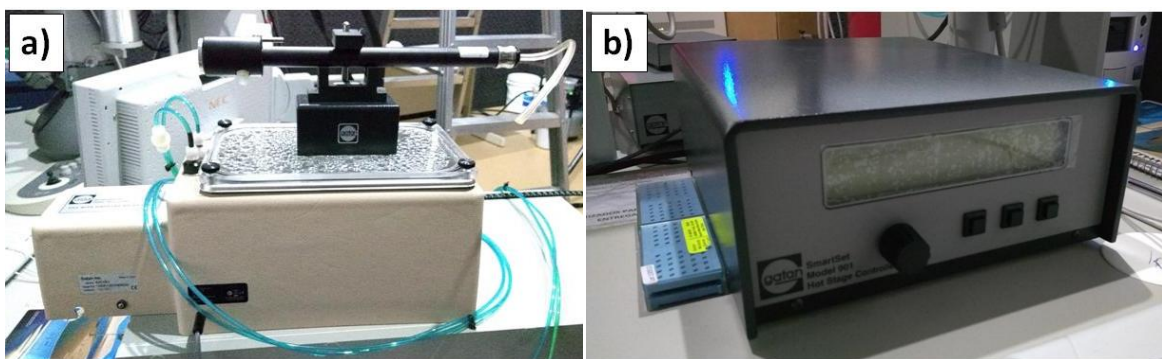
Figure 3.12 - a) Gatan 628 single tilt heating holder, and b) SmartSet Hot Stage controller.

The Gatan heating holder works by the passage of an electric current through a conductor, producing heat (Joule heating effect). Water circulates through the holder shaft to keep it cool, thus, only the holder tip (where the sample is) reaches high temperatures.

4   RESULTS AND ANALYSIS

4.1   Synthesis of Ceria nanocrystals

For the cerium oxide nanoparticles, a previously reported synthesis was tested. Although the synthesis by the hydrothermal method has been reported in several studies [68,70], the lack of repetitiveness (less than 30%) and the low amount of material obtained in each synthesis difficult the use of this synthesis. Figure 4.1 shows XRD patterns of the nanoparticles obtained in this work, and those reported in the literature. The broadband in small angles and the small size of the peaks shows a large amount of organic, by-products of the synthesis, and a small quantity of nanoparticle.

| a) | b) |
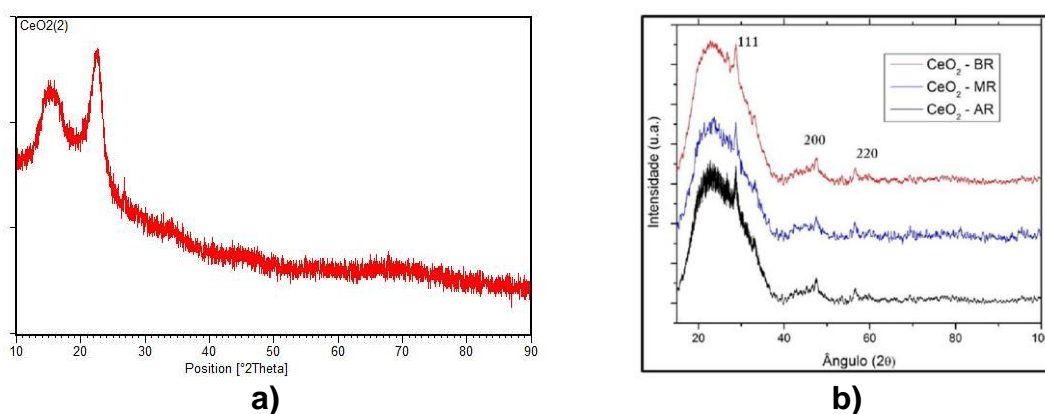
Figure 4.1 - XRD pattern of the samples synthesized by the hydrothermal methodology, (a) synthesized on the laboratory, and (b) reported on the literature.

Figure 4.2 shows that although it is possible to synthesize cerium oxide nanoparticles using the hydrothermal method, with the methodology reported on the literature, a small amount of nanoparticles is obtained and the control in size and shape is complicated. The size distribution reported in the literature is between 4 and 6 nm (Figure 4.3c, d), which is very similar to those obtained in this work.
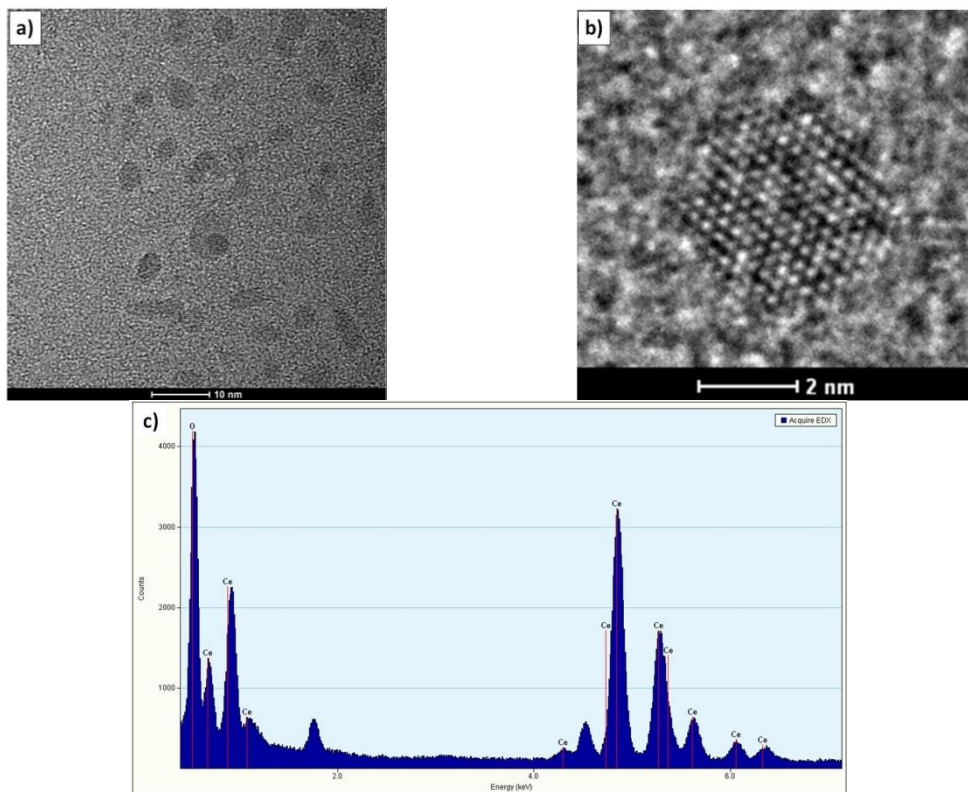
Figure 4.2 - a) Low magnification TEM image, b) HRTEM image, and c) EDS of the ceria nanoparticles synthesized by the hydrothermal method.
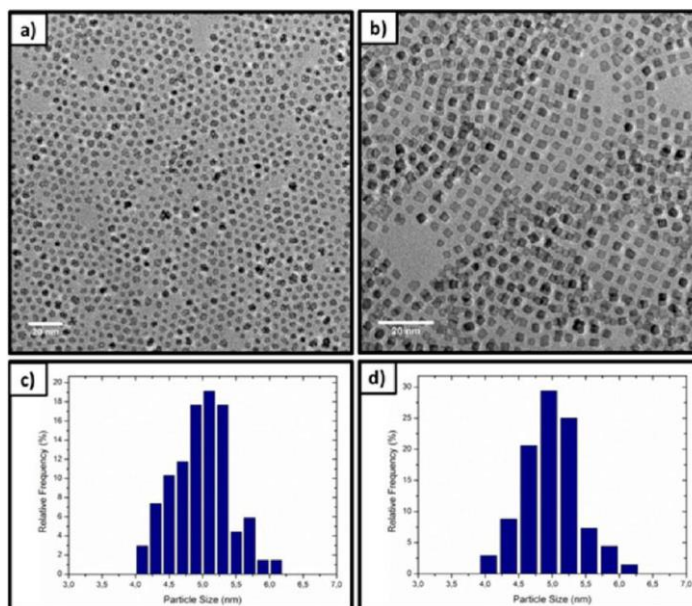
Figure 4.3 - a), b) TEM images, and c), d) particles size distribution of cerium nanoparticles reported by Cordeiro *et al.* [70].

To ensure a better control of size and morphology, a novel synthesis using the solvent-controlled methodology was proposed. Several syntheses using cerium acetylacetonate (Ce(acac)$_3$) are reported in the literature [17,25,53]. Seung Soo Lee *et al.* reported near-spherical cerium oxide nanocrystals with 4, 6, and 10 nm when cerium nitrate is used as a precursor, and oleylamine and 1-octadecene as solvents; and nanocrystals with 3 nm when Ce(acac)$_3$ is used as a precursor [17]. Generally, it is very common to find syntheses that use cerium nitrate as a precursor (because it is cheaper compared to other precursors), and when other precursors are used, such as acetylacetonate or isopropoxide, the solvents commonly used are benzylamine or benzyl alcohol (respectively). In syntheses of other metal oxides, such as Fe$_3$O$_4$, acetylacetonate and oleic acid have been used successfully to obtain nanoparticles [53]. Other works made by the group has also successfully synthesized iron oxide nanoparticles, using oleyl alcohol (OLA) as solvent [79]. Another advantage of solvent-controlled synthesis with OLA is its cost efficiency, because when compared to other solvents (commonly used in those syntheses) his price per mole is lower. Table 4.1 shows the price of several solvents used in solvothermal and solvent-controlled syntheses, the prices were consulted on the Sigma-Aldrich website in July 2018.

Table 4.1 - Price per mol of some solvents used in solvothermal syntheses.

Reagent	Purity [%]	Molecular Weight [g/mol]	Density @ 25°C [g/mL]	Price [R$]	Price, pure [R$/mol]
Oleyl alcohol	85	268.48	0.849	312.00 / 100g	985.48
Oleylamine	70	267.49	0.813	261.00 / 100g	997.36
Oleic acid	90	282.46	0.887	263.00 / 1L	93.06
1,2-Hexadecanediol	90	258.44	-	3039.00 / 50g	17453.31
1-Octadecene	90	252.48	0.789	271.00 / 1L	96.36
				224.00 / 25mL	3185.78

As an example, for oleyl alcohol:

$$\frac{312\ R\$}{100g(85\%)} = 3.6706\ \frac{R\$}{g} \quad \rightarrow \quad 3.6706\frac{R\$}{g} * 268.48\frac{g}{mol} = 985.48\frac{R\$}{mol}$$

So, for the simplicity in the syntheses, reliability and cost efficiency, a novel synthesis by the solvent-controlled methodology, using Ce(acac)$_3$ as a precursor, and oleyl alcohol as solvent was developed. Several syntheses were made to optimize the time and temperature at each stage of the synthesis. To identify the temperatures used in the synthesis, the thermal decomposition of the cerium [III] acetylacetonate was studied [80].

Figure 4.4 summarizes some of the different thermal cycles tested in several syntheses until obtaining a reproducible methodology. The first two syntheses were made with 8 and 4 mmol of Ce(acac)$_3$, in 15 mL of OLA, but after several hours at 110°C never solubilized, so those were discarded and the amount of Ce(acac)$_3$ was decreased to 1 mmol, solubilizing at 80°C after half an hour. Generally for a successful synthesis the dehydration of the precursors is necessary, this is achieved heating the dissolution above 80 or 100°C. With the Ce(acac)$_3$ hydrate, when the temperature exceed 100°C the dissolution become turbid, with agglomerates, and not nanoparticles were obtained. To avoid this, the Ce(acac)$_3$ hydrate powder was dried in the oven at 60°C overnight, changing the color from a light yellow-gold, to a dark orange-brown; this powder was stored on the glove-box to prevent future rehydration.

Two groups of tests were performed, the first with only one heating cycle (named CeO2 acac#), and the second with a heating cycle, cooled, aged for 2 day, followed by another heating cycle (named CeO2 acac#_2). All tests made with previously dehydrated Ce(acac)$_3$ showed good results (tests #13 onwards). Tests made in two stages, i.e., heating, cooling, aging for 2 days, and heating again; also showed good results.

Figure 4.5 shows that if two tests, of one and two stages, made with the same temperatures and holding times were compared, the sample made in two stages have no agglomerates; e.g. samples #6 or #7 (heated at 260°C for 2h, increased to 315°C for 1h), vs sample #8_2 (heated at 260°C for 2h, cooled, aged for 2 day, and heated to 315°C for 1h). This may be related to the bivalent nature of cerium, which is +3 in the Ce(acac)$_3$ but changes to +4 to form a more stable oxide; the 2 days aging perhaps helped the entry of oxygen to the

dissolution and the nucleation of oxides nanoparticles (CeO_2 instead of Ce_2O_3), due to the previously decomposition of the $Ce(acac)_3$ at 260°C.
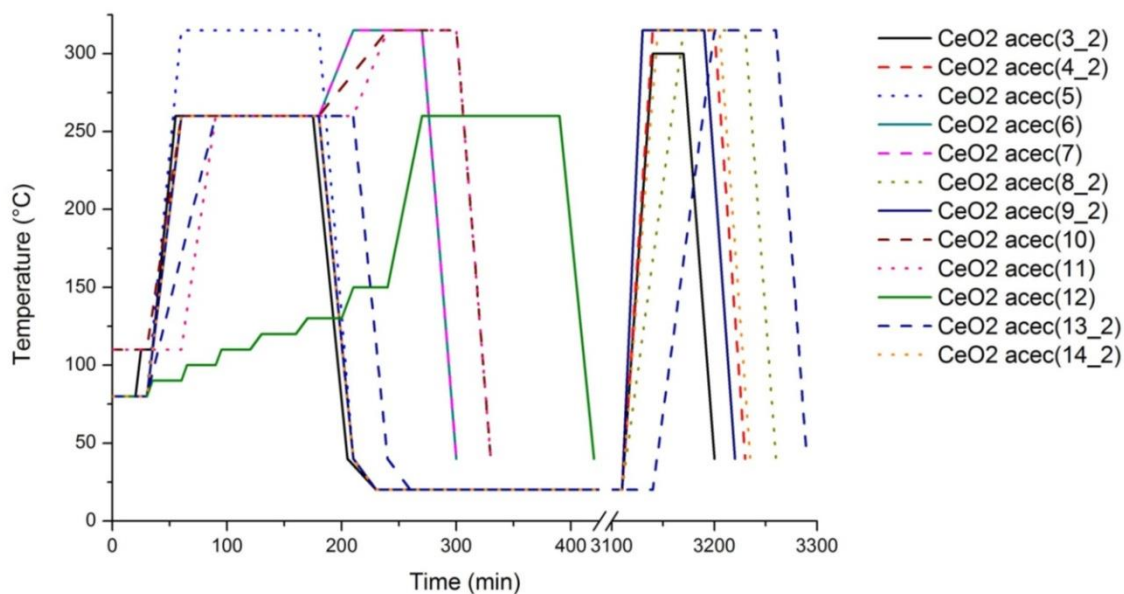
Figure 4.4 - Thermal cycles of the different tests of solvent-controlled syntheses.

Figure 4.5 - Dispersions of the different syntheses made by the solvent-controlled method using hydrated precursors.

Figure 4.6 shows that although it is possible to obtain nanoparticles starting from the hydrated precursor, there are some agglomerates and control of size and morphology is poor.
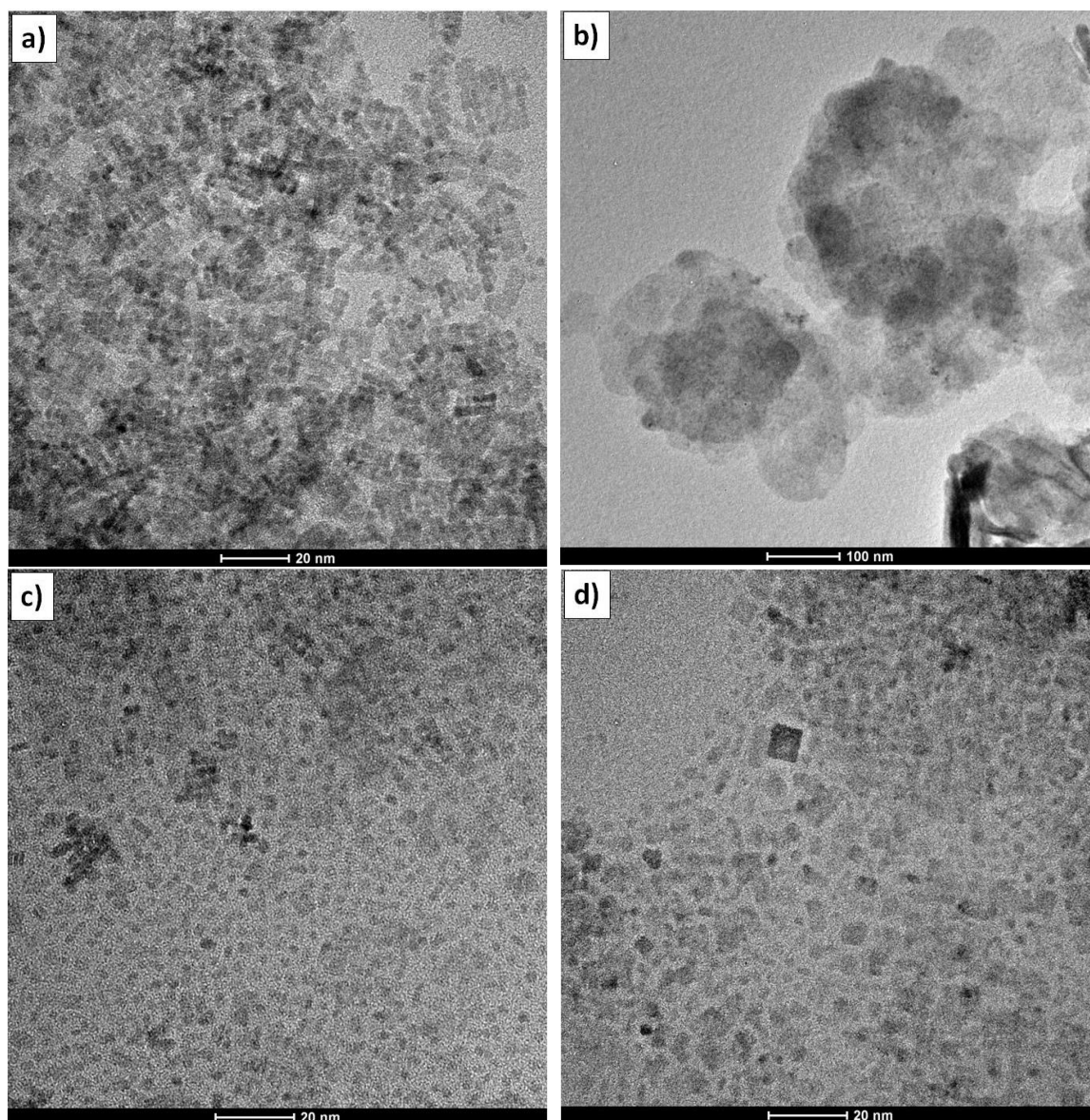
Figure 4.6 – Low magnification HRTEM images of ceria synthesis made by the solvent-controlled method; samples (a) CeO2 acec(3_2), (b) CeO2 acec(5), (c) CeO2 acec(6), and (d) CeO2 acec(8_2).

After optimizing the synthesis process, four tests were performed varying the amount of OAm (0, 1, 3 and 5 mmol), as specified in the methodology. Figure 4.7 shows the nanoparticles dissolved on toluene; up to 3 mmol of OAm a yellowish solution was obtained, the solution remained stable for months and the change on intensity is related to the concentration. On the sample with 5 mmol large agglomerates was obtained and it was not possible to disperse in organic solvents.

Figure 4.7 - Dispersion of the different synthesis made by the solvent-controlled method using previously dehydrated precursors; from left to right the samples has 0, 1, 3, and 5 mmol of OAm respectively

It is worth noting that the sample with 5 mmol of OAm had many problems during the synthesis, because when the amount of OAm increases explosions occur. Perhaps, the acetone produced during the decomposition of the Ce(acac)3, which has low melting point, condenses and when the drops come into contact with the solution at high temperature of the synthesis, they implodes. The explosions create smoke, delay the evacuation of the gases produced during the synthesis, propitiate the entry of air, and hinder the correct circulation of nitrogen. Maybe in another laboratory assembly, with a triple-neck round-bottom flask, where the gas inlet and outlet of gases are in different lines, the nanoparticles can be successfully synthesized with higher amounts of OAm. As the sample with 5 mmol of OAm did not synthesize, it was discarded and will not be considered for future discussions.

The OAm has been widely used to control the size and morphology of several nanoparticles syntheses [81]. From Figure 4.7 and Figure 4.8, can be observed that for the methodology developed in this work, a low amount of OAm (1 mmol) has no influence on the size or morphology, but a higher quantity (3 mmol) can favor the agglomeration of the nanoparticles. This could indicate that the OAm remove the oleate layer formed by the OLA, and for the

times explored in these experiments there is not bond between the OAm and the surface of the nanoparticles; leaving exposed the surface of the nanoparticles, facilitating the agglomeration. Perhaps with longer holding times at 315°C the OAm might bind to the surface of the nanoparticles, but longer times could also imply an increase in the size of the nanoparticles.

To characterize the crystal structure of the samples, with 0, 1 and 3 mmol of OAm, XRD patterns were made. The XRD patterns (Figure 4.9) revealed a characteristic cubic fluorite structure on the three samples (JCPDS card no. 034-0394). Regarding to the crystal structure, no significant differences were observed between the three samples. Comparing Figure 4.1 and Figure 4.9 can be observed that in the samples synthesized by the solvent-controlled method all peaks are present, even in the sample with 3 mmol of OAm; unlike the samples synthesized by the hydrothermal method, where only the peaks (111) and (220) were observed in a very discrete way.

To quantify the amount of organic layer on the surfaces of the nanoparticles TGAs were performed, under pure oxygen flux. Figure 4.10 shows a very similar behavior between the three samples, having a mass loss in two stages. The first stage in the range of 55-220°C, is related to the desorption of toluene and free OLA trapped among the organic layer; the second mass loss correspond to the decomposition of the oleates groups in the range of 220-320°C. These results are consistent with the observed on Figure 4.8e, showing an arrangement of the nanoparticles due a loss of the organic layer in some of its crystallographic planes. This is confirmed by the 15% less mass in the sample synthesized with 3 mmol of OAm.
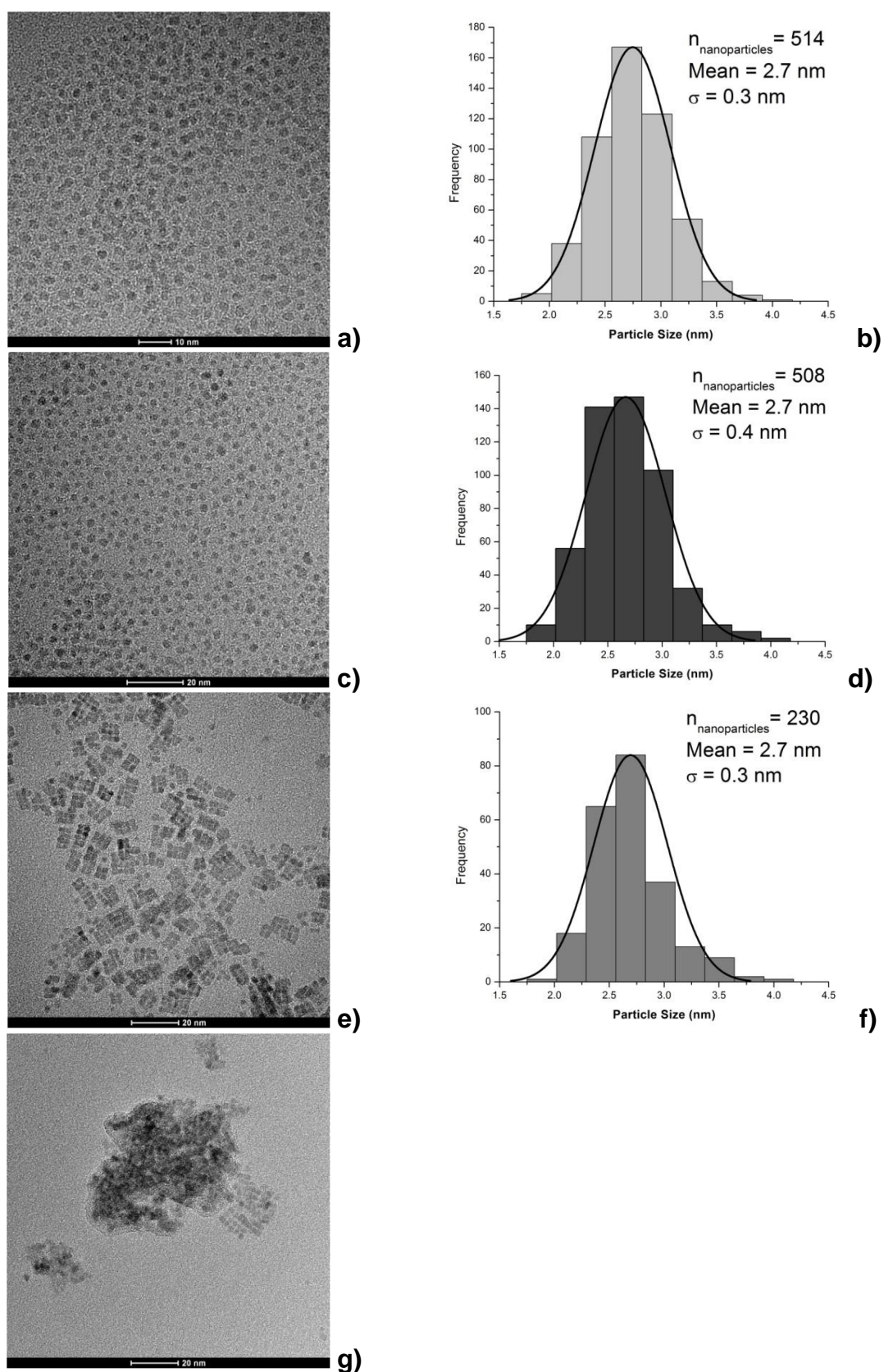
Figure 4.8 - TEM images and particle size distribution of ceria nanoparticles synthesized with, 0 a) and b), 1 c) and d), 3 e) and f), and 5 mmol of OAm.
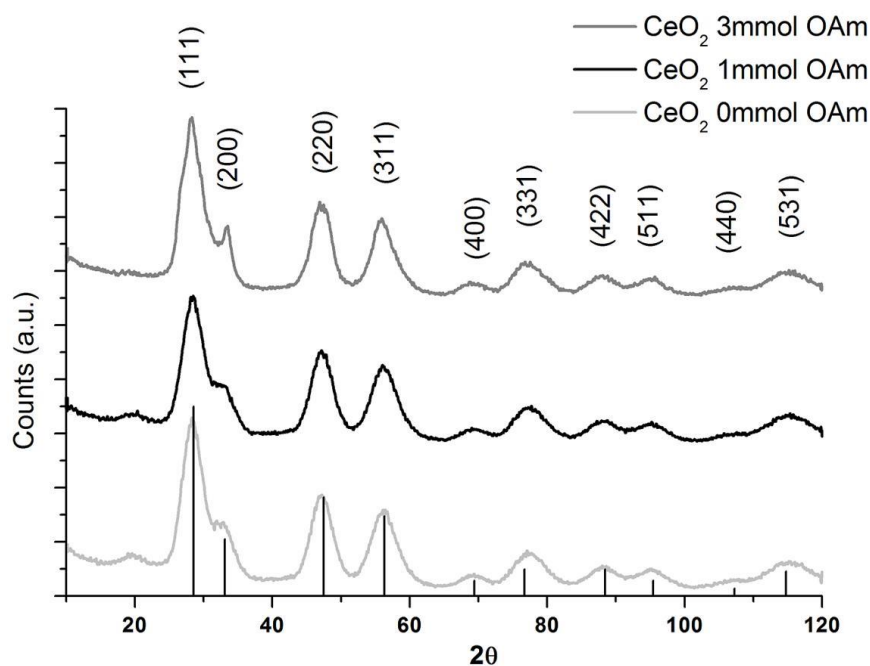
Figure 4.9 - XRD patterns of ceria nanoparticles synthesized with 0, 1 and 3 mmol of OAm.
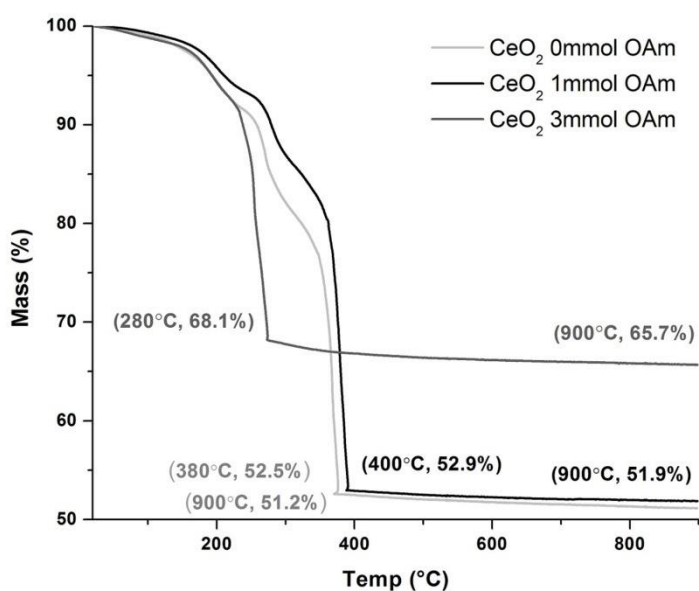
Figure 4.10 - TGA of ceria nanoparticles synthesized with 0, 1 and 3 mmol of OAm.

Figure 4.11 shows the UV-visible absorption spectrums of the samples synthesized by the solvent-controlled method. The three samples exhibit an

absorption peak around 290 nm, which is characteristic of the ceria nanoparticles, no significant differences were observed between the three samples.
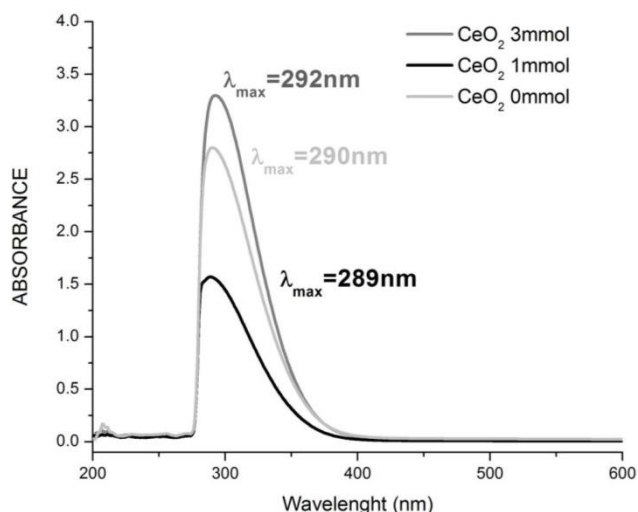
Figure 4.11 - UV-Visible spectrum of ceria nanoparticles synthesized with 0, 1 and 3 mmol of OAm.

For a more complete characterization of the nanoparticles, HRTEM were obtained. Figure 4.12a, c, and e shows high resolution images of isolated nanoparticles. From the fast Fourier transform (FFT) of the HRTEM images (Figure 4.12b, d, and f) can be observed that the zone axis is the same for all the isolated nanoparticles, i.e. [$\bar{1}01$], but when the nanoparticles are linked together the zone axis changes to [010] (Figure 4.12g and h). Figure 4.13a shows low magnification HRTEM images of nanoparticles synthesized with zero mmol of oleylamine, where no interaction between particles is observed and the FFT of the whole image (Figure 4.13b) shows that the spots correspond to the (111) and (200) planes, reaffirming that most of the isolated particles are oriented in the zone axis [$\bar{1}01$]. Figure 4.13c shows the FFT of the image of nanoparticles synthesized with 3 mmol of OAm; in this case the spots corresponding to the (220) plane appears more frequently, showing that when the particles interact it is more likely to observe them oriented on the zone axis [010]. Other images can be found in APPENDIX B (Figure B.1 and Figure B.2).
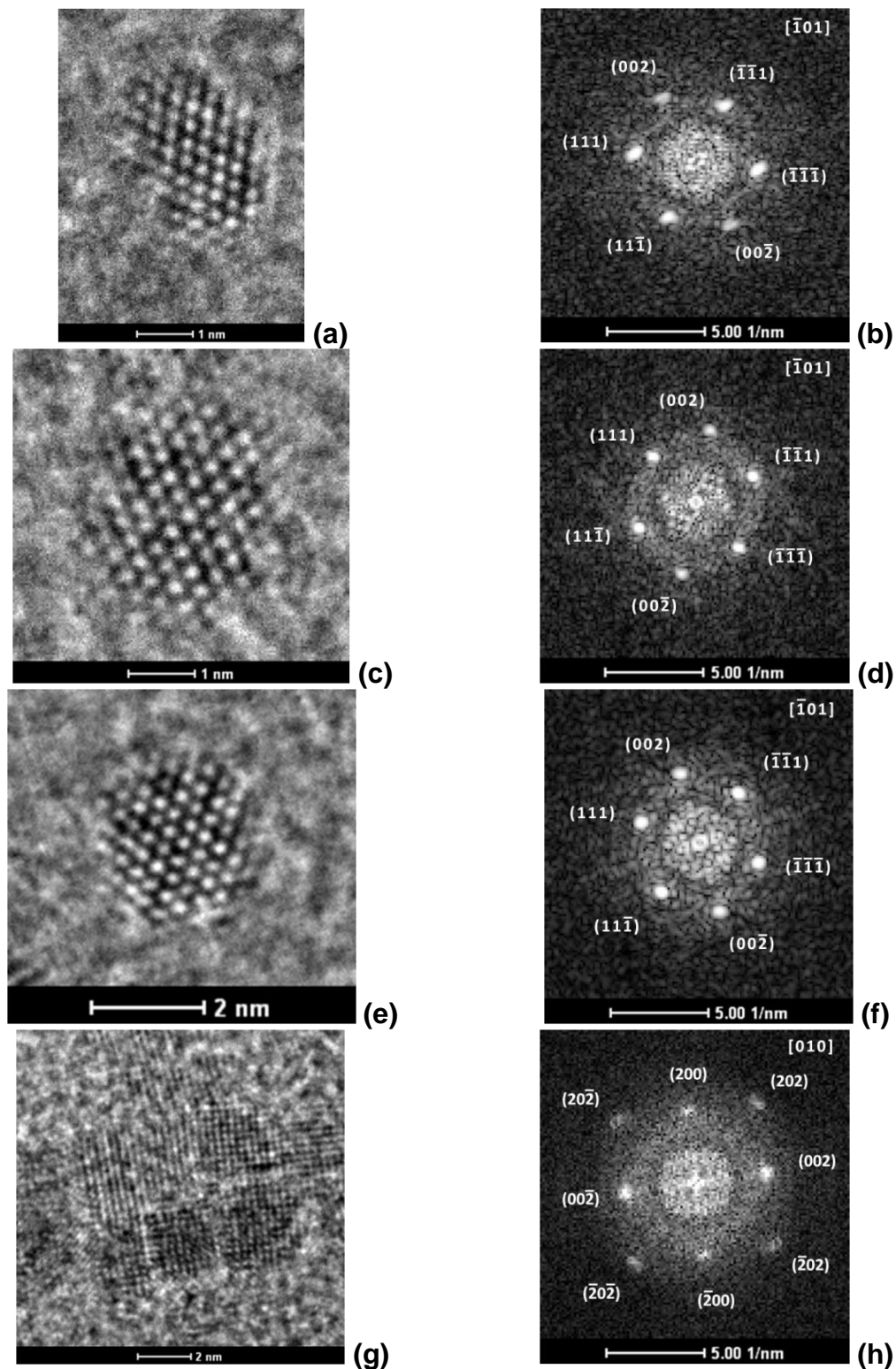
Figure 4.12 - HRTEM images and the corresponding FFT of ceria nanoparticles synthesized with, 0 a) and b), 1 c) and d), 3 mmol of OAm e), f), g), and h).
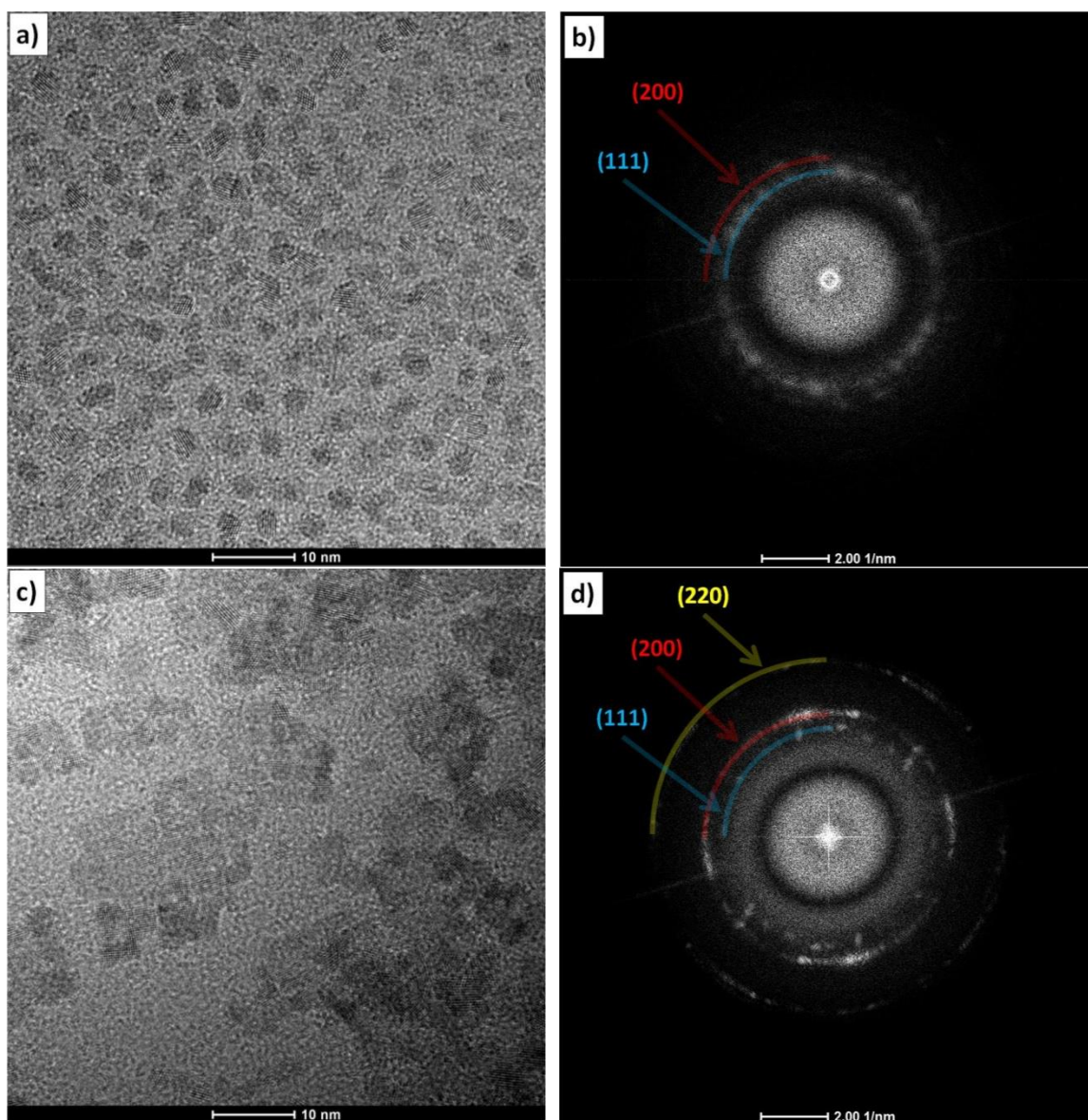
Figure 4.13 - Low magnification HRTEM images and the corresponding FFT of ceria nanoparticles synthesized with, 0 a) and b), 3 mmol of OAm c) and d).

The fact than the nanoparticles have a selective orientation when linked is an indication that an "oriented attachment" may be happening; due to a selective removal of the organic layer in specific planes by the OAm. It is well known that the OAm can act as a surfactant, solvent, and reducing agent. Also, when combined with other surfactants and depending on their relative ratio, the OAm bind selectively with some crystal planes helping to control the final morphology of the particles [53,81].

To check the accuracy of the HRTEM characterization, HRTEM multislice simulations using the software Dr. Probe [82] were made. CeO_2 with cubic fluorite structure and Fm3m space group under the experimental image conditions was used for the simulations. Figure 4.14c shows an isolated CeO_2 nanoparticle oriented in the zone axis $[\bar{1}01]$, inset the multislice simulation (red box) fits properly with the HRTEM image, reaffirming that the crystalline structure and the crystallographic orientation correspond to those previously mentioned. It can be noticed that the diffraction spots in the HRTEM images correspond to the columns of the Ce atoms for this orientation.
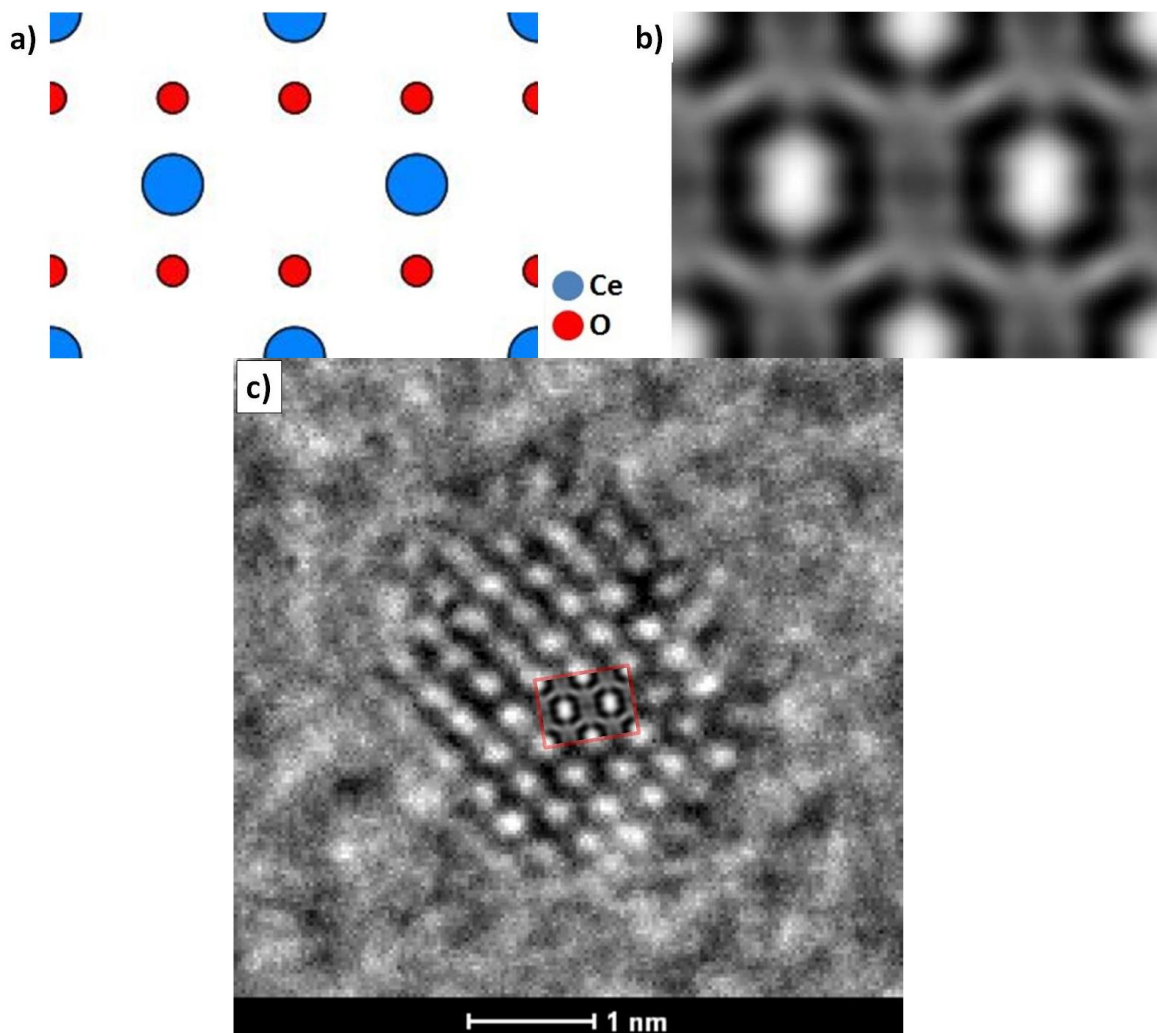
Figure 4.14 - a) CeO_2 with fluorite structure oriented in the zone axis $[\bar{1}01]$, b) multislice image simulation for the experimental image conditions, and c) HRTEM image of CeO2 nanoparticle, inset, the red lines indicate the HRTEM multislice simulation.

In order to identify the exposed crystallographic planes in the nanoparticles, several 3D particles were simulated using the software VESTA [76]. Figure 4.15 shows three possible configurations. The nanoparticle on the Figure 4.15a has 4 x 4 x 2 unit cells, approx, with exposed planes {111}, {110}, and {100}. Figure 4.15b has 4 x 4 x 3 unit cells, approx, with exposed planes {111}, {110}, and {100}. Figure 4.15c has 4 x 4 x 3 unit cells, approx, with exposed planes {111}, and {100}. Figure 4.15b, and Figure 4.15c are very similar, the only difference is one atom at the tip of the corners, that when removed leave the planes {110} exposed.

a)   b)   c)
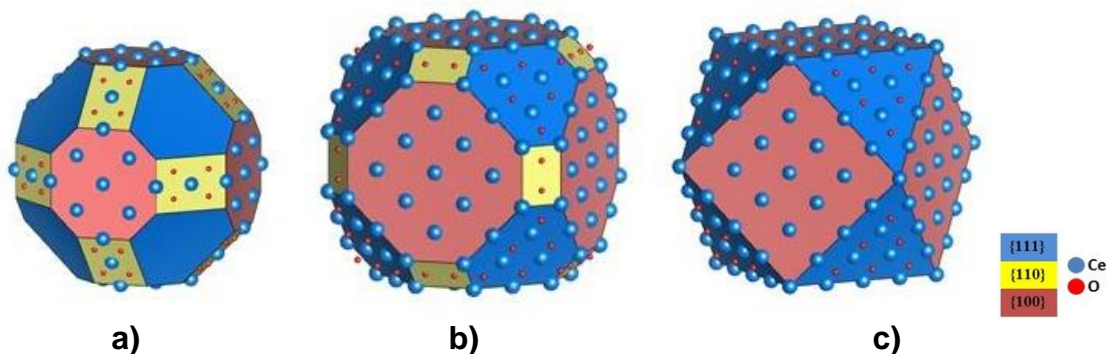
Figure 4.15 - 3D simulation of ceria nanoparticles with fluorite structure.

Due to the small size of the nanoparticles (2.7 nm) and with a difference of only 1 atom at the corner, to be sure which reconstruction is the most accurate, a deeper characterization is required. In the larger nanoparticles (e.g. 5 nm) the difference would be 4 or more atoms, which would greatly facilitate the characterization. It is worth noting that looking through the $[\bar{1}01]$ zone axis only one atom appear at the tip of the corners (where the {110} plane should be). Getting a signal from just one atom, through the ≈ 3 nm carbon film that generates a greater amount of noise, is very difficult. Thereby, even if the atom is there, it probably will not appear on the HRTEM images.

At this point, it is worth discussing if the remotion of only one atom is enough to justify the creation, or not, of a new crystallographic plane. Figure 4.16 shows the representation of the unit cell of CeO_2 with fluorite structure, observing the Figure 4.16c and comparing the Figure 4.15b and c; can be

noticed that only half of the (110) plane of the unit cell appear when the cerium atom on the tips of the nanoparticle is removed. It is difficult to know if, indeed, the (110) plane is stabilizing or if simply, keep an atom in that position is very unstable by the fact of having virtually no neighbors around.

a)   **b)**   **c)**
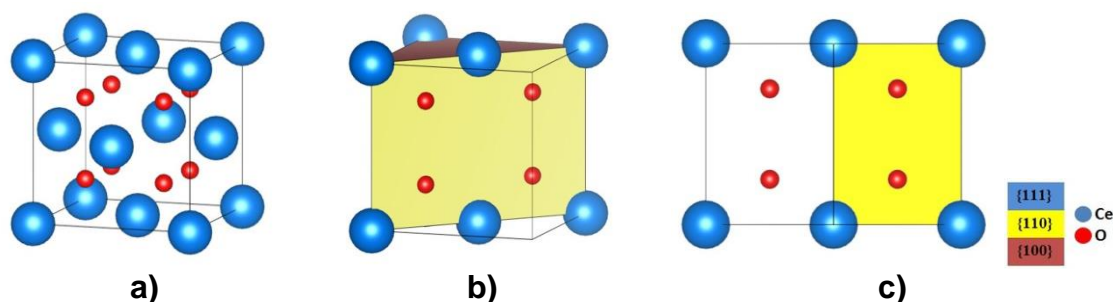
Figure 4.16 – a) Representation of the unit cell of CeO_2 (Fluorite), b) and c) (110) plane.

Figure 4.17 shows the superimposition of 3D simulations (Figure 4.15a, and b) over HRTEM images of isolated nanoparticles synthesized with 1 and 3 mmol of OAm. In both nanoparticles, it is noted that the best fit is with the simulation shown in Figure 4.15b; the symmetry of the particle seems to be very good, and the few points that do not fit can be atoms on the crystal that are outside the Ewald's sphere.

Both nanoparticles (synthesized with 1 and 3 mmol OAm) fits almost perfectly to the same 3D simulated crystal (Figure 4.15b), therefore, we can assume that in the three synthesis all nanoparticles have the same morphology. This suggests that the OAm does not affect the morphology (in this synthesis), but favors the agglomeration in a specific orientation. This hypothesis is supported by the fact that the particle size distribution is equal on the three syntheses.
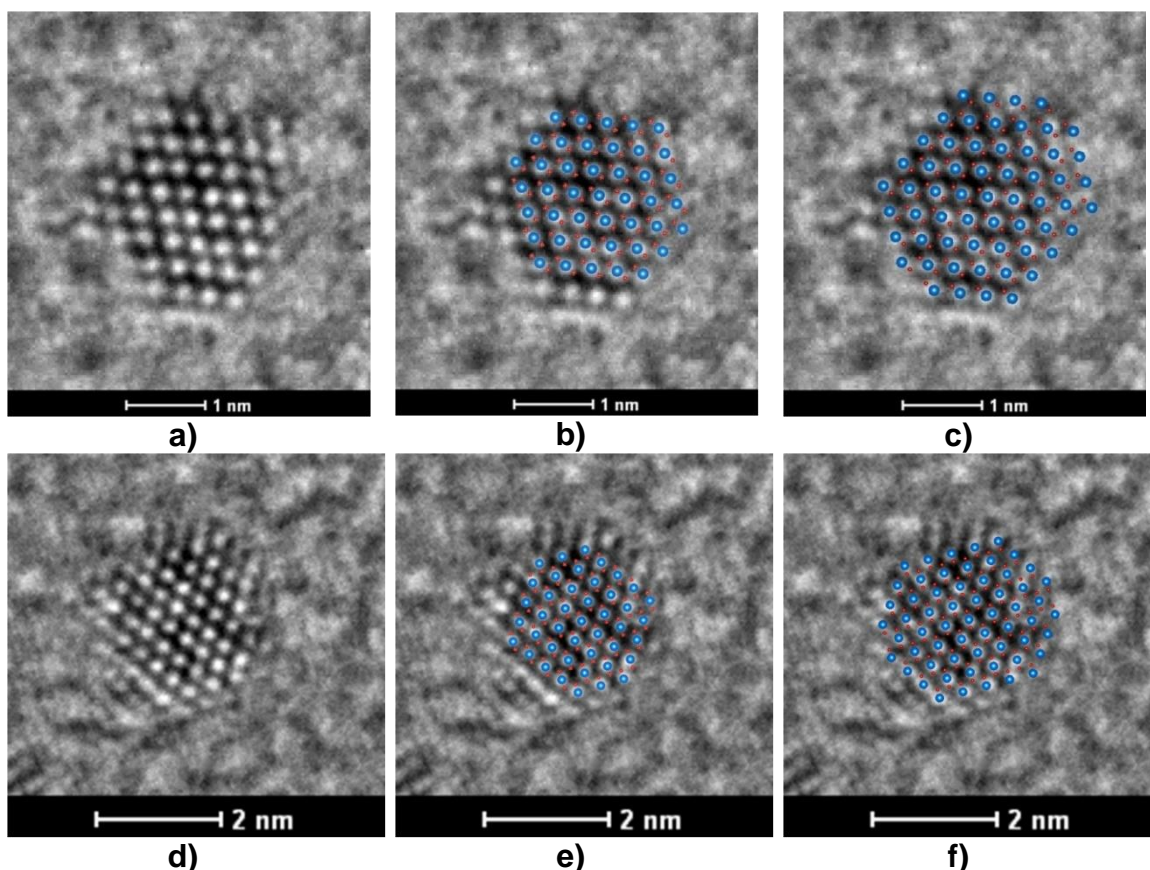
Figure 4.17 - Superimposition of simulated 3D crystals over HRTEM images. Isolated nanoparticles of ceria synthesized with a), b), and c) 1, and d), e), and f) 3 mmol of OAm.

To evaluate the nanoparticles assembly in a specific crystallographic plane, due to the selective removal of the organic layer by the OAm, 3D crystals were attached in different crystallographic planes to simulate the images observed on the Figure 4.8e. Comparing Figure 4.8e and Figure 4.18c a similarity in the arrangement of nanoparticles is perceived, which suggest that the OAm reacts preferentially with the {100} crystallographic planes. For a better comprehension of how the OAm reacts with the different crystallographic planes, to replace (or remove) the oleates groups, further theoretical studies are required.

a)   **b)**   **c)**
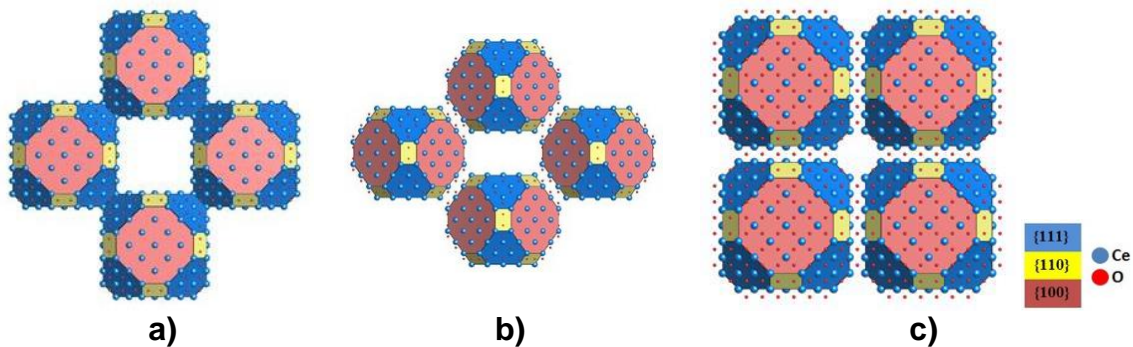
Figure 4.18 - Simulated assembly of ceria nanoparticles; oriented assembly on the crystallographic plane a) {110}, b) {111}, and c) {100}.

The assembly of the nanoparticles, as shown in Figure 4.18, could also explain the growth mechanism of larger cube-like nanocrystals of cerium oxide. Also, the absence of the cerium atoms at the tips of the 2.7 nm nanoparticles explains the deficit of cerium atoms on the center of the {100} faces of cube-like nanocrystals, with size ≈5.2 nm [70], as shown Figure 4.19. This answers some doubts of the scientific community, and helps improve our understanding of the mechanisms of growth of nanoparticles.
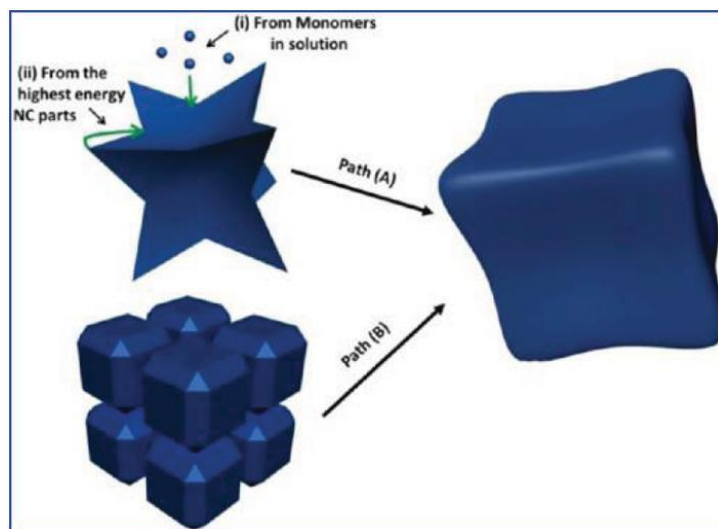
Figure 4.19 - Two possible growth mechanisms of the CeO_2 cube-like NCs [70].

Finally, after a comprehensive characterization of the cerium oxide nanoparticles synthesized by the solvent-controlled method, the morphology and the main crystallographic planes ({100}, and {111}) were described.

It is worth noting that there are no previous reports in the literature of a synthesis of cerium oxide nanoparticles using cerium acetylacetonate as a precursor, and oleyl alcohol as solvent. Here is reported a novel synthesis with average size as low as 2.7 nm, and with a narrow distribution, and a high reproducibility (above 80%).

4.2   Synthesis of Zirconia nanocrystals

The zirconium oxide nanoparticles were made based on previously reported synthesis from Niederberger *et al.* [47,73]. As previously described in the methodology, the zirconia nanoparticles were submitted to a change in the organic layer. To ensure that this stage does not change the crystal structure of the nanoparticles, different characterization techniques were performed before and after the process.

Figure 4.20 shows a typical cubic structure of the zirconium oxide (JCPDS card no. 003-0640); no change on the crystal structure was perceived after the second cycle in the reactor for the change of the organic layer. From Figure 4.20 and Figure 4.21 can be observed that the change of the organic layer produced no significant change in the crystal structure or morphology of the nanoparticles.
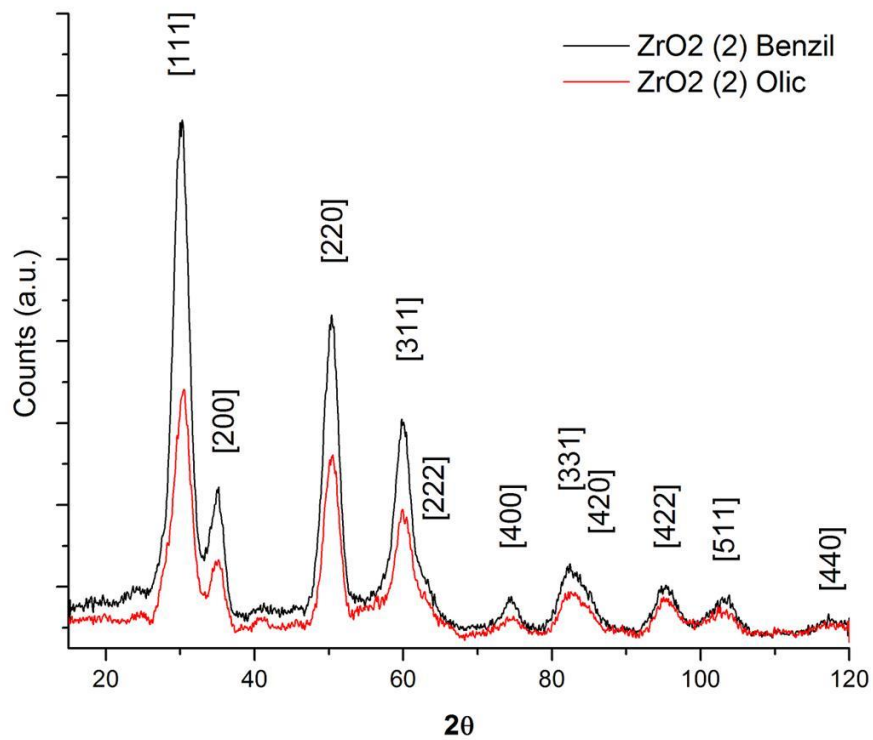
Figure 4.20 - XRD patterns of zirconia nanoparticles before (benzyl alcohol) and after (oleic acid) the change of the organic layer.
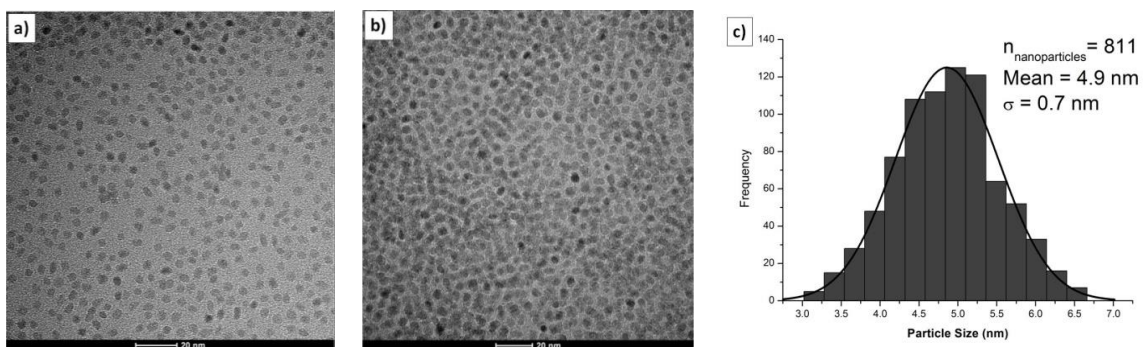
Figure 4.21 – Low magnification HRTEM images of zirconia nanoparticles; a) before, and b) after the change of the organic layer. c) Particle size distribution after the change of the organic layer.
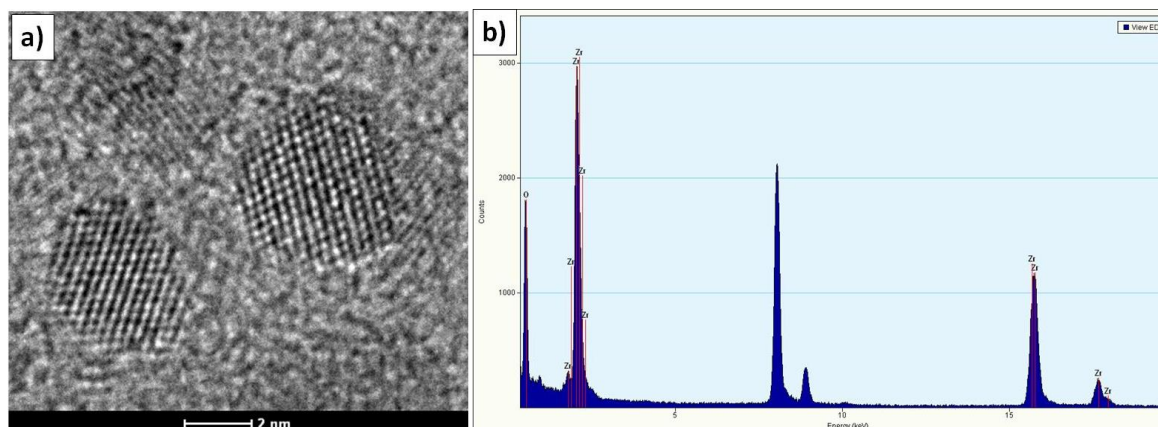
Figure 4.22 – a) HRTEM image, and b) EDS of the zirconia nanoparticles after the change of the organic layer.

Figure 4.23 shows behavior a very similar to that observed in ceria samples, a two stages mass loss. The total mass loss in the sample of zirconia is 14% higher than the ceria (with 0, and 1 mmol of OAm). The amount of organic layer present on the nanoparticles should not affect the *in situ* tests, because the organic layer in the samples will be removed before performing the tests, to ensure that they can make contact and can react with each other.
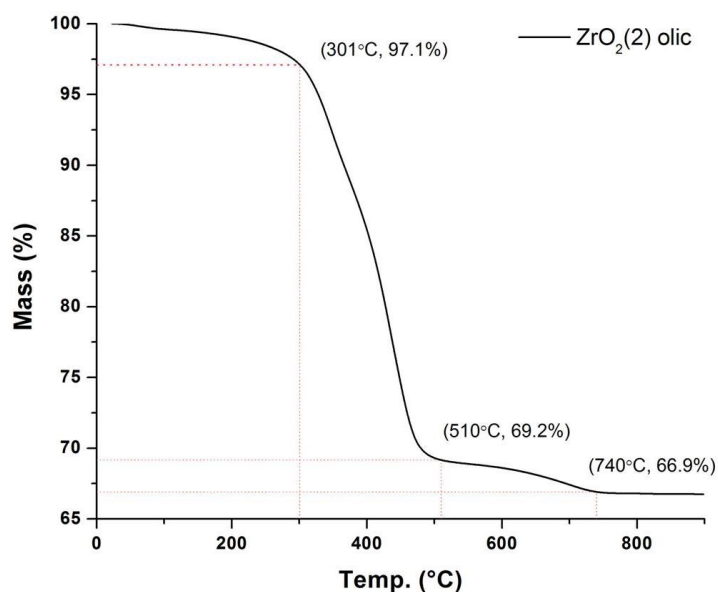
Figure 4.23 - TGA of zirconia nanoparticles after the change of the organic layer.

Figure 4.24 shows the zirconia nanoparticles forming a yellowish dissolution in toluene; this yellow color is characteristic from the oleic layer.
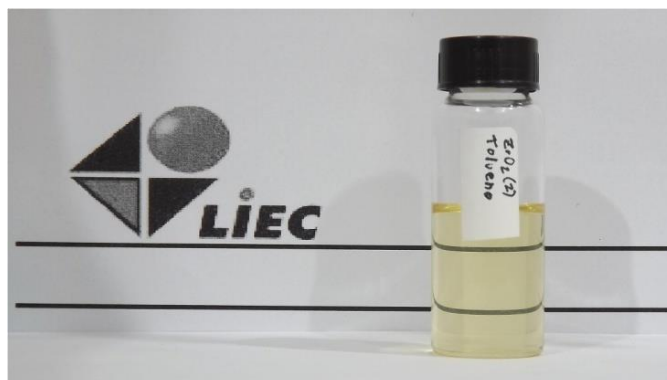
Figure 4.24 - Dispersion of zirconia nanoparticles after the change of the organic layer

4.3   *Ex situ* tests

Since copper TEM grids are highly sensitive to high temperatures (low melting point, high thermal strain) the firsts *ex situ* tests were made at a maximum temperature of 300°C. Figure 4.25 shows mixed nanoparticles after an *ex situ* test at 300°C for 2 hours, compared with the sample before the test (Figure 3.8a) no changes were observed. Other tests were attempted without success because the copper grid breaks at higher temperatures or longer times. To achieve higher temperatures that allow the reaction between particles it is necessary to use silicon nitride (Si_3N_4) grids. To prepare samples on the Si_3N_4 grids it is necessary drip 1.0-1.5 µL of the dilution over the grid, as shown on the Figure 4.26b. The process to remove the organic layer was the described above (Section 3.4).
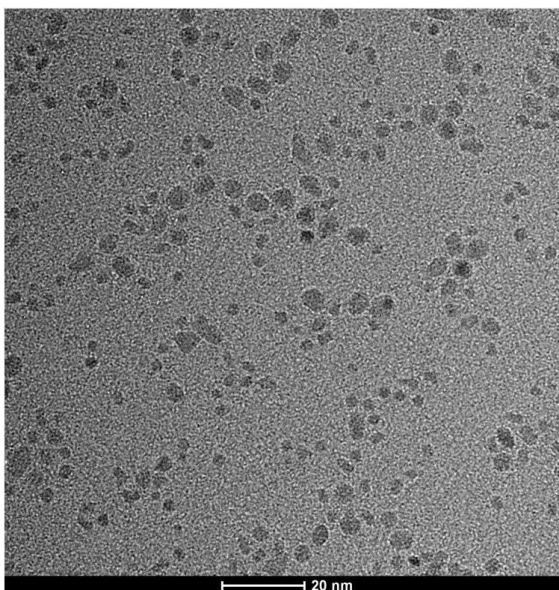
Figure 4.25 - Low magnification HRTEM image of mixed nanoparticles (CeO_2 and ZrO_2) after an *ex situ* test at 300°C for 2 hours.

| a) | b) |
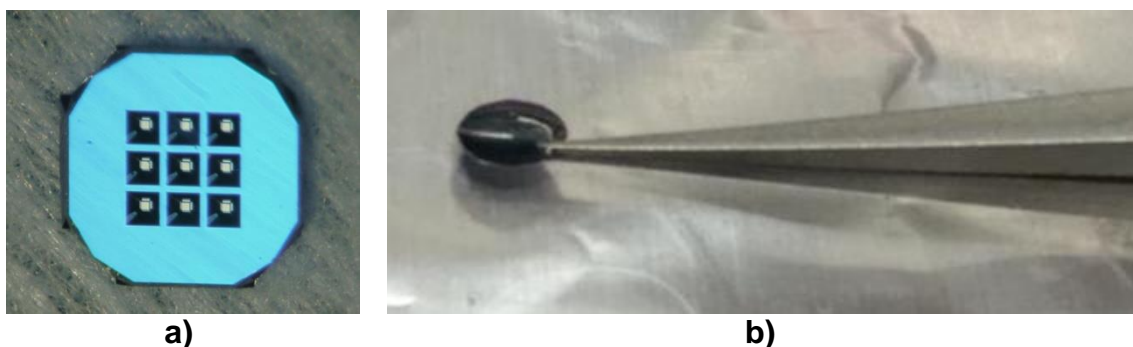
Figure 4.26 - a) Silicon nitride TEM 9 windows grid with 5 nm thick square membrane, and b) drop of the dilution of mixed oxides over the TEM grid.

Other *ex situ* tests were performed at 500°C for 30 minutes, 600°C for 30 minutes, and 600°C for 1 hour. Figure 4.27 shows HRTEM images of the sample treated at 500°C for 30 minutes; as the previous tests, no significant changes were observed. Comparing the Figure 4.27 with Figure 4.25, no significant differences were observed, there is still no evidence of agglomeration, growth (Ostwald ripening) or sintering. On the APPENDIX B (Figure B.3) more images can be found, showing that there are no differences in the particles before and after the *ex situ* test at 500°C for 30 minutes.
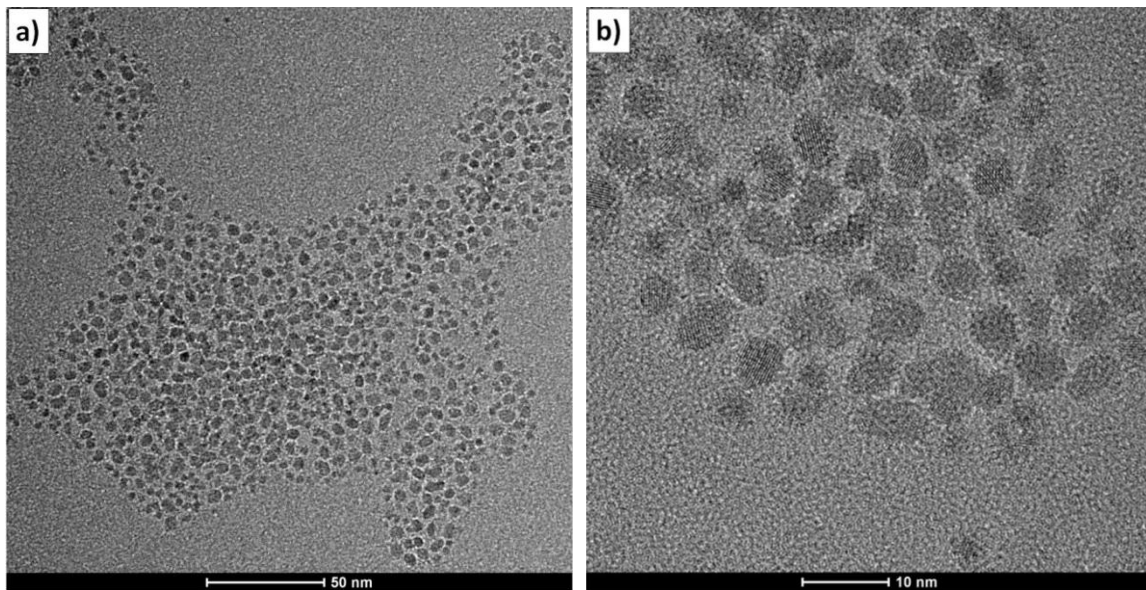
Figure 4.27 - Low magnification HRTEM images of *ex situ* test at 500°C for 30 minutes in mixed nanoparticles of CeO_2 and ZrO_2.

Figure 4.28 shows HRTEM images of the sample treated at 600°C for 30 minutes, in contrast to the sample at 500°C for 30 minutes, at this temperature and time a slight agglomeration of the nanoparticles is notice, and no growth is observed. Nevertheless, sintering processes begin to take place, mainly oriented attachment. On the APPENDIX B (Figure B.4) more images can be found, showing the slight differences in the particles before and after the *ex situ* test at 600°C for 30 minutes.

Figure 4.29 shows the assembly between two ceria nanoparticles, the red line represent the (111) plane in the bottom particle, and the orange represent the same plane in the upper particle. A misalignment of 31±1° can be observed between the two nanoparticles. The angle between the planes can be easily measured as an azimuthal angle on the FFT of the image (Figure 4.29b). Although a perfect oriented attachment was the most probable option, in these conditions where the degrees of freedom (movement and rotation) of a particle are restricted (for being over a silicon TEM grid), these misalignments can be expected.
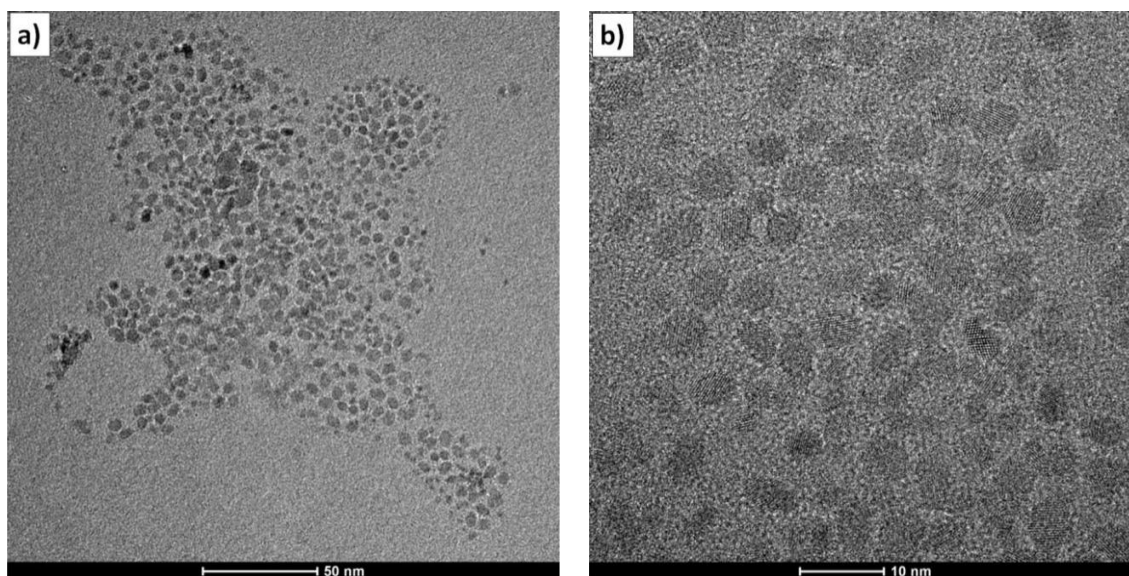
Figure 4.28 - Low magnification HRTEM images of *ex situ* test at 600°C for 30 minutes in mixed nanoparticles of CeO_2 and ZrO_2.
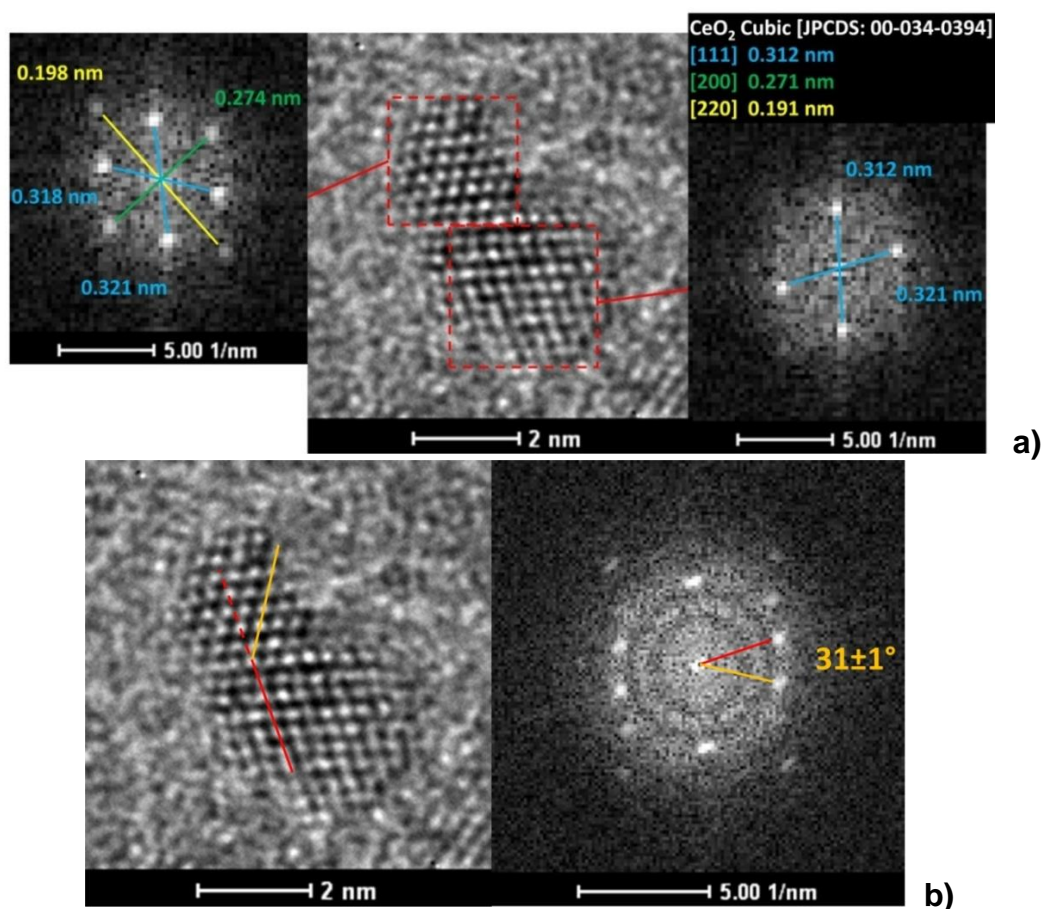
Figure 4.29 - HRTEM images of *ex situ* test at 600°C for 30, a) FFT of two CeO_2 nanoparticles, and b) FFT of both nanoparticles, the red and orange line represent the (111) plane on each particle.

Figure 4.30 shows HRTEM images of the sample treated at 600°C for 60 minutes, as in the sample treated for 30 minutes, an agglomeration of the particles can be noticed. However, there is no significant difference when increasing the time from 30 to 60 minutes at this temperature. As in the sample treated for 30 minutes, the oriented attachment phenomenon is observed, this time more often and the agglomeration is more visible. On the APPENDIX B (Figure B.5) more images can be found, showing a higher agglomeration of the particles after the *ex situ* test at 600°C for 60 minutes, even so no sintering is observed. Although at this temperature phenomena such as oriented attachment begin to be observed, until now only the assembly between nanoparticles of the same type was observed (i.e. CeO_2 with CeO_2, or ZrO_2 with ZrO_2). To try to see mixture or growth higher temperatures must be tested.

Figure 4.31 shows oriented attachment between ceria nanoparticles. The phenomenon is different from that observed in the synthesis with 3 mmol of OAm, when the organic layer is selectively removed from the (100) planes and the oriented attachment only occurred on those planes. In this case the oriented attachment occurs in other planes since the organic layer was completely removed. Figure 4.32 shows the particle size distribution of the ceria and zirconia particles before and after the ex situ test, a decrease in the number of isolated ceria particles can be noticed (<4 nm), while larger particles (>8 nm) begin to appear due to the fusion of the initial particles.
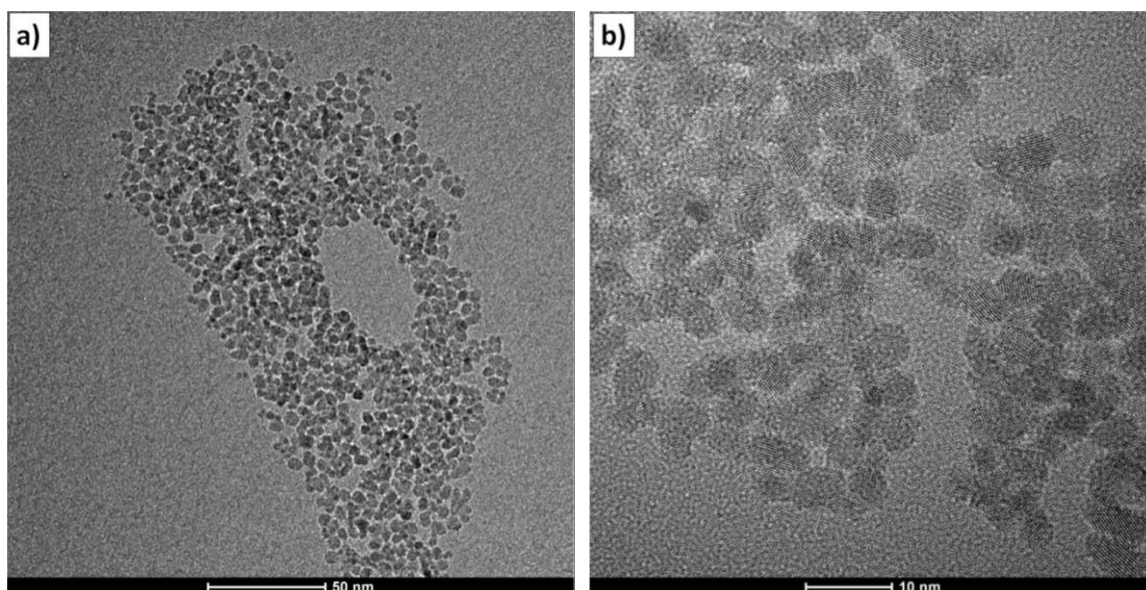
Figure 4.30 - Low magnification HRTEM images of *ex situ* test at 600°C for 60 minutes in mixed nanoparticles of CeO_2 and ZrO_2.
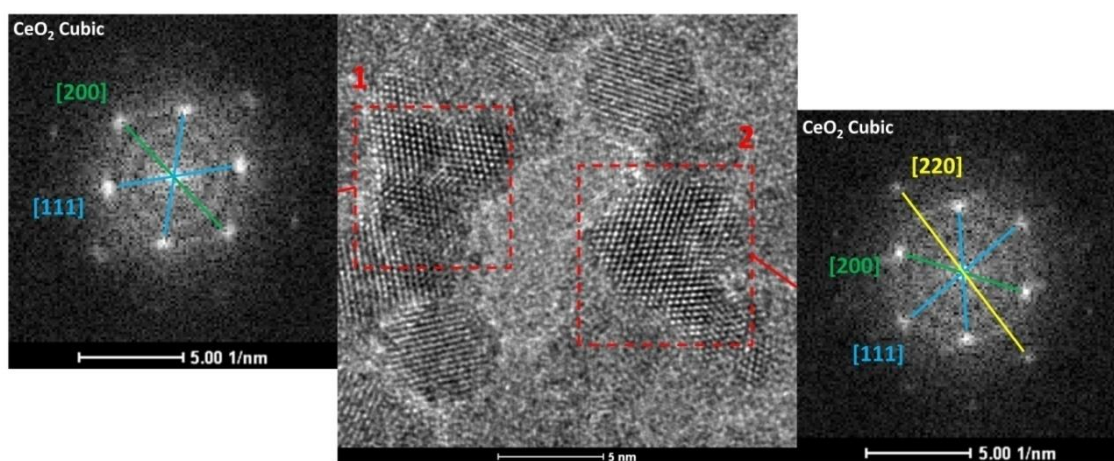
Figure 4.31 - HRTEM image of *ex situ* test at 600°C for 60 minutes. Inset FFT of some ceria nanoparticles in oriented attachment.
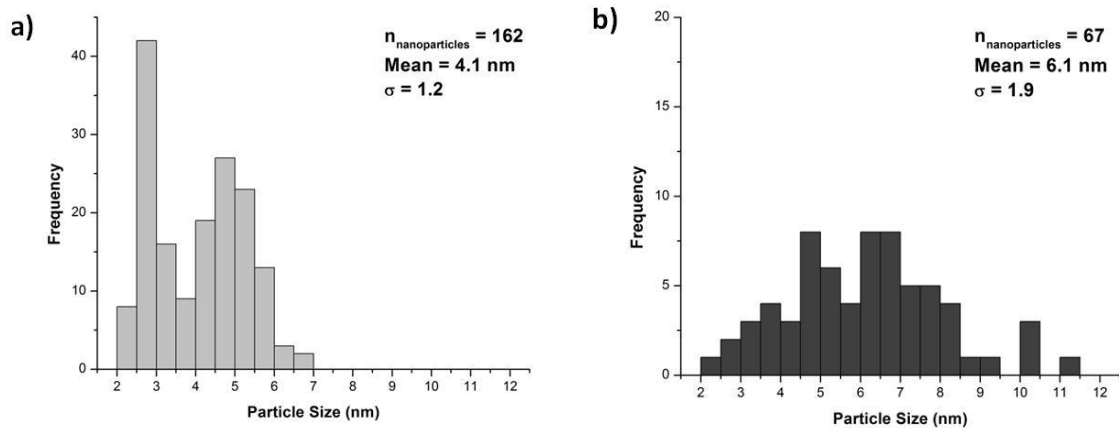
Figure 4.32 - Particle size distribution of CeO_2 and ZrO_2 a) before, and b) after *ex situ* test at 600°C for 60 minutes.

4.4   The dose-rate threshold of beam damage

To ensure that the phenomena observed during the *in situ* experiments are due to the increase in temperature and not by electron irradiation, a sample of ZrO_2 nanoparticles was subjected to different electron beam current density (EBCD) at room temperature for one hour, the sample was prepared on a Cu grid and the organic layer of the nanoparticles was previously removed.
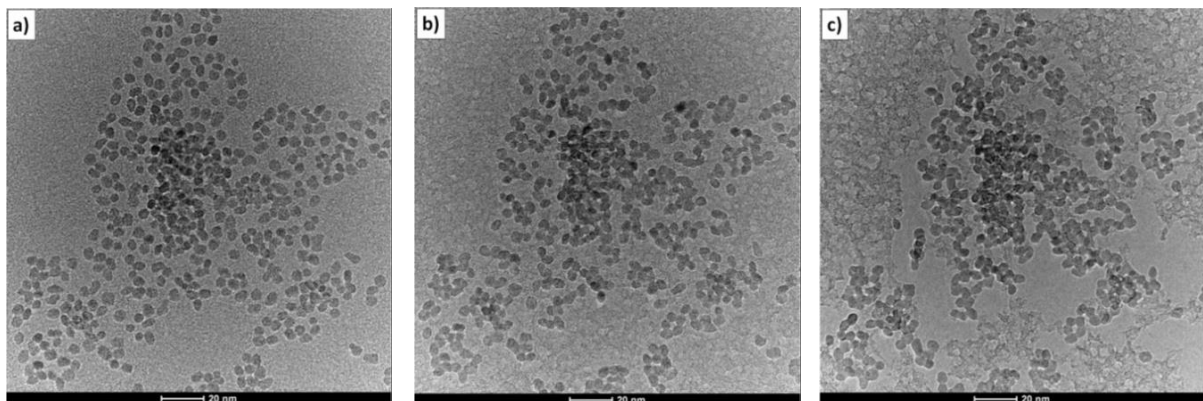
Figure 4.33 - Low magnification HRTEM images of ZrO_2 nanoparticles at room temperature exposed to an EBCD of 5000 A/m^2 for: a) 0 min, b) 30 min, and c) 60 min.
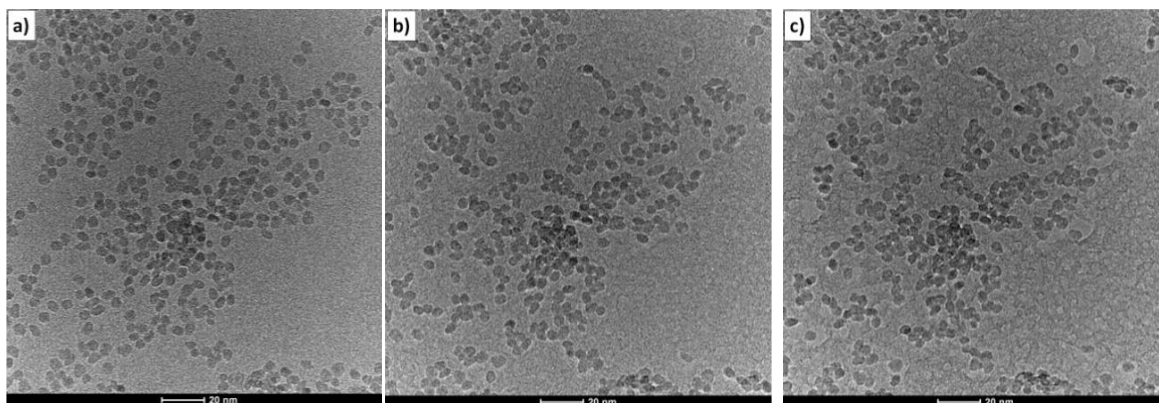
Figure 4.34 - Low magnification HRTEM images of ZrO$_2$ nanoparticles at room temperature exposed to an EBCD of 2000 A/m^2 for: a) 0 min, b) 30 min, and c) 60 min.
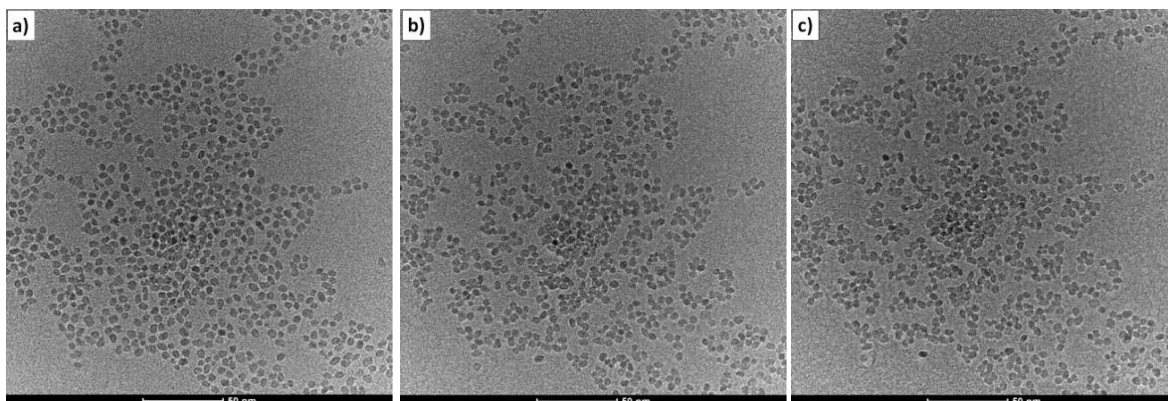
Figure 4.35 - Low magnification HRTEM images of ZrO$_2$ nanoparticles at room temperature exposed to an EBCD of 1000 A/m^2 for: a) 0 min, b) 30 min, and c) 60 min.
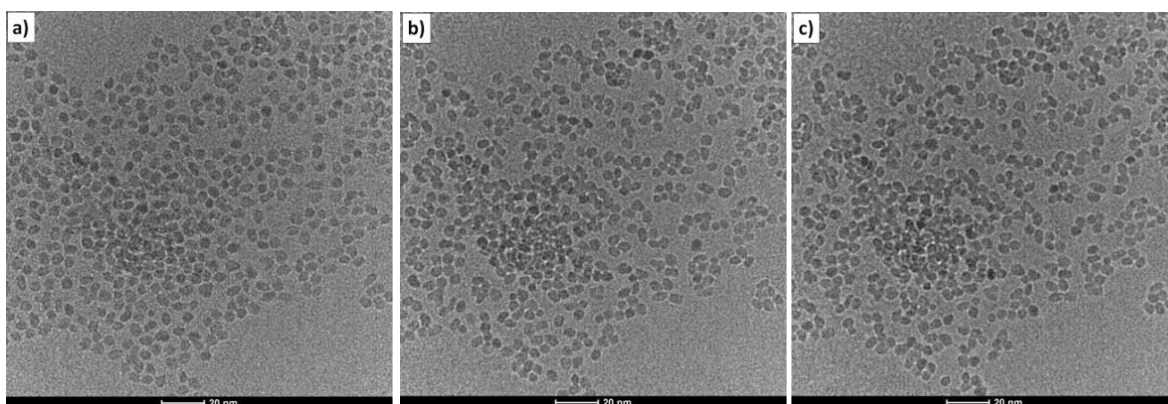
Figure 4.36 - Low magnification HRTEM images of ZrO$_2$ nanoparticles at room temperature exposed to an EBCD of 800 A/m^2 for: a) 0 min, b) 30 min, and c) 60 min.

The Figure 4.33 to Figure 4.36 shows the effect of the electron beam on the samples, and on the α-C film of the grid. For 5000 A/m^2 the beam damage is massive, while for 800 A/m^2 is almost negligible. Since the *knock-on* damage is related to the beam energy (acceleration voltage) and during our experiments it was set at 300 KV, this type of damage will always be present. Damage by radiolysis (inelastic scattering) it is usually known to be proportional to the energy deposited per unit volume of the specimen, so we can infer that a higher EBCD increases the damage produced by radiolysis. Obviously at high temperatures can exist a synergy and the beam damage could be higher for the same dose reported at room temperature. But, as a first approximation, we can infer that for EBCD below 800 A/m^2 the main contribution to the phenomena observed will be the temperature.

Analyzing Figure 4.34, we can see a decrease in the projected area of the nanoparticles over time. As the images were acquired at room temperature, this decrease in the area can only be due to beam damage. The beam damage can be easily noticed in the carbon film. By increasing the beam damage, more and more atoms are removed from the carbon film, decreasing their thickness. By decreasing the thickness of the film there are fewer interactions between the electron beam and the atoms, increasing the number of electrons that reach the camera, making the image brighter in the thinner areas (when observed in bright-field, or high resolution mode). When the damage is massive, the material can be completely removed and vacuum regions can be observed.

Figure 4.37 shows some zooms to the Figure 4.34. By increasing the beam damage more atoms of the nanoparticles are removed, decreasing their volume (which is observed as a smaller projected area). Figure 4.38 shows the change in the projected area of four particles, in general we can see a reduction in the area. Two particles present a peculiar behavior at minute 30; this may be due to a rotation of the particle, which affects the projected area but not the real volume.
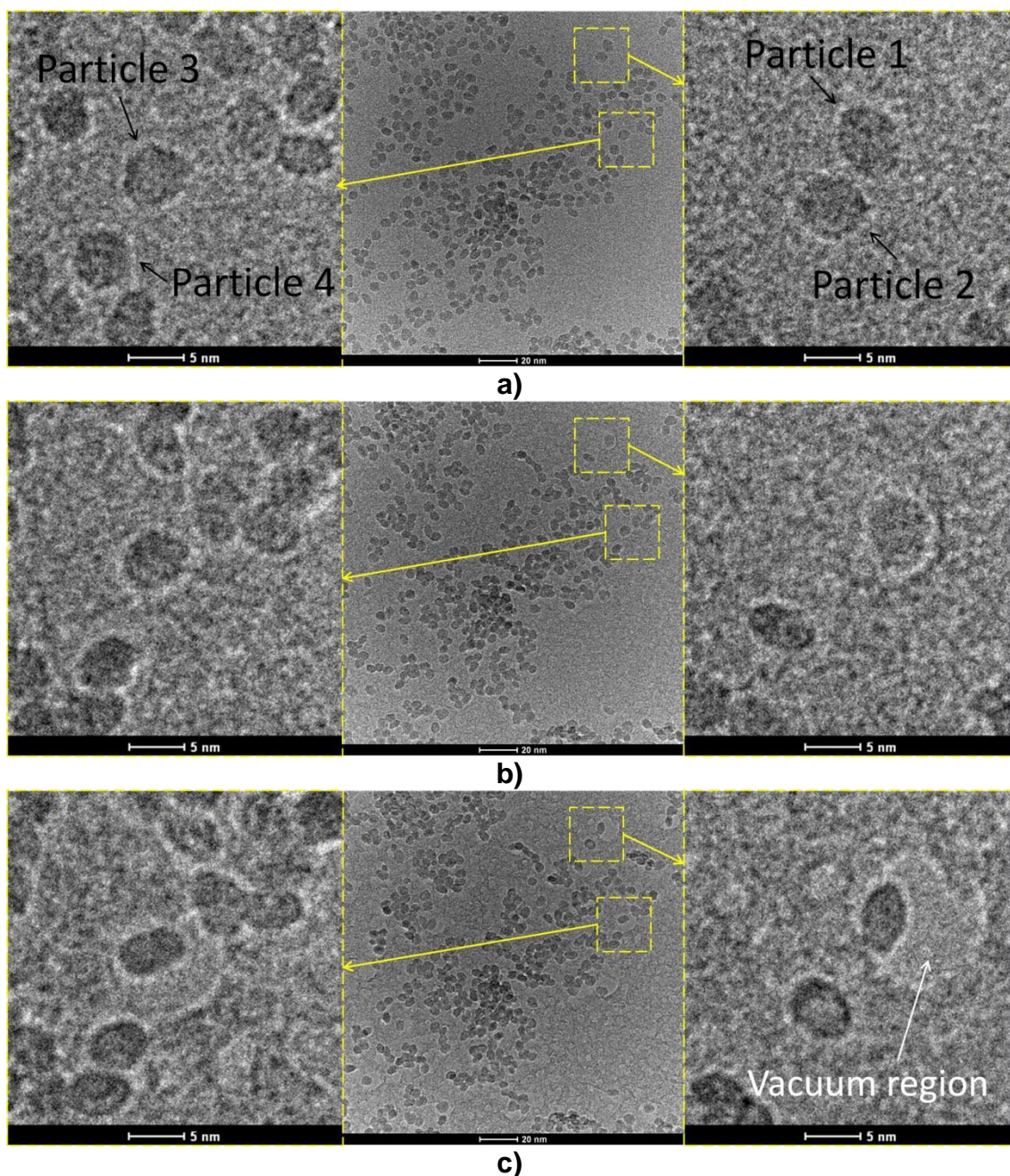
Figure 4.37 - Zoom of Figure 4.34, highlighting some ZrO_2 nanoparticles at room temperature exposed to an EBCD of 2000 A/m^2 for: a) 0 min, b) 30 min, and c) 60 min.
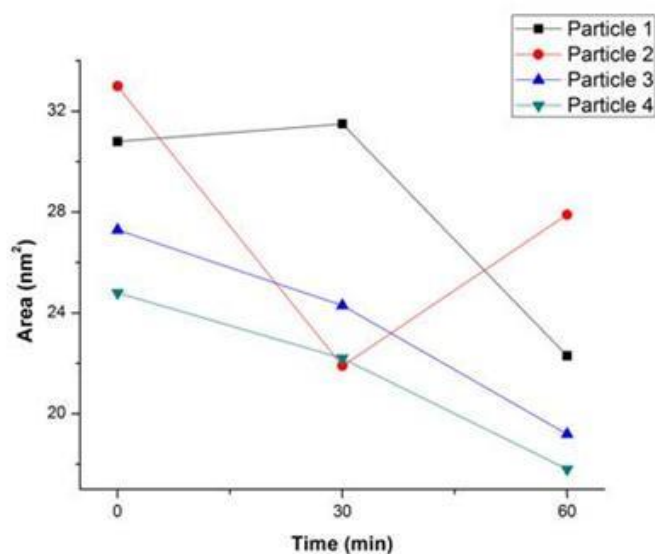
Figure 4.38 - Change in the projected area of the nanoparticles shown in Figure 4.37.

The nanoparticles exposed to an EBCD of 1000 A/m^2 for 60 minutes did not evidence significant changes (Figure 4.35), but as some damage is noticed in the carbon film, the EBCD was reduced to 800 A/m^2.

4.5 *In situ* tests

A mixture of the CeO$_2$ and ZrO$_2$ nanoparticles with 50-50 wt% was prepared and 1.0-1.5 µL of the dispersion was drip over a silicon grid. To remove the organic layer a heat treatment in an oxygen-rich atmosphere was made, heating the sample to 110°C for 5 min, and later to 210°C for 10 min (as described in the previous sections). Figure 4.39 shows low magnification HRTEM images of an *in situ* test, where the sample was heated to 800°C and held for 90 min, later the temperature was increased to 900°C and held for 90 min, and again increased to 950°C and held for 30 min. The EBCD used was between 700-400 A/m^2.

As can be observed, there is no significant change, even in the particles that are more agglomerated (like those in the lower part of the image). On other works with CeO$_2$ nanoparticles, the authors report dissolution, and growth of new particles at 890°C within a period of about 10 min [68]. The authors don't

report the EBCD used on the experiments, the nanoparticles have a mean size of 5 nm, and the samples were prepared in a Molybdenum (Mo) grid coated with α-C film (5 nm thick). A hypothesis is that the temperature helps disintegrates some particles, and the atoms that remain on the surface of the carbon film move until find other particles, making them grow. In our case, the damage is negligible and apparently there is very low (or no) mobility of the particles on the surface of the Si_3N_4. Several experiments were performed, starting from 500°C for 120 min until the results shown in Figure 4.39, none of those experiments showed any significant change.

To simplify the comparison, two images were superposed and subtracted; one at the beginning (i.e. 800°C for 0 min) and other at the end of the test (i.e. 950°C for 30 min). If both images were equal, the result would be a black image (all pixels with value 0), since both images are not exactly the same, only slightly different, the result is very low contrast image. Figure 4.40a shows the subtraction of Figure 4.39a and Figure 4.39d; since no irregularities are observed in the image, and due to the low contrast, we can conclude that both images are analogous and that there are not significant changes during the experiment.
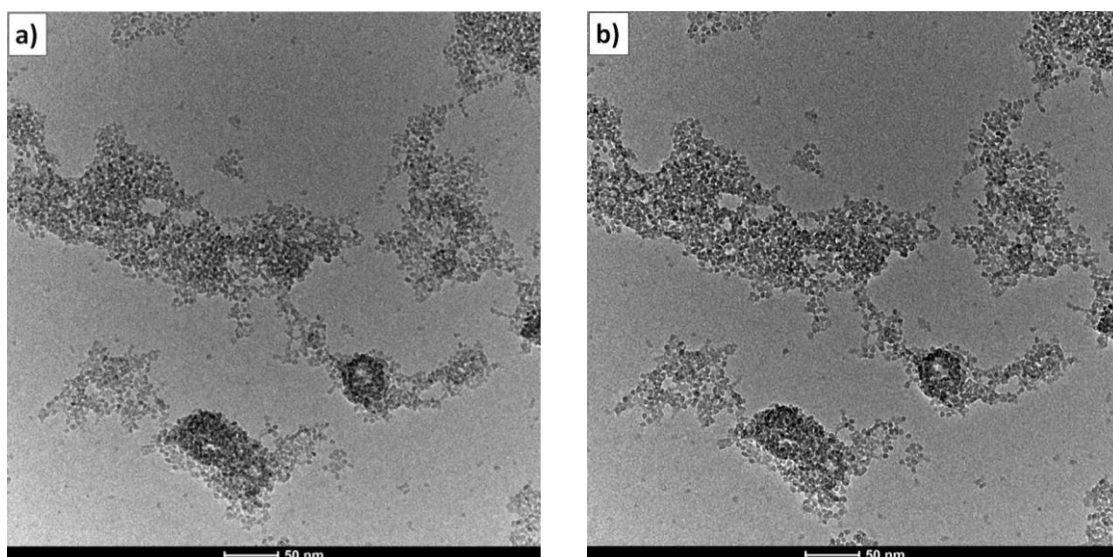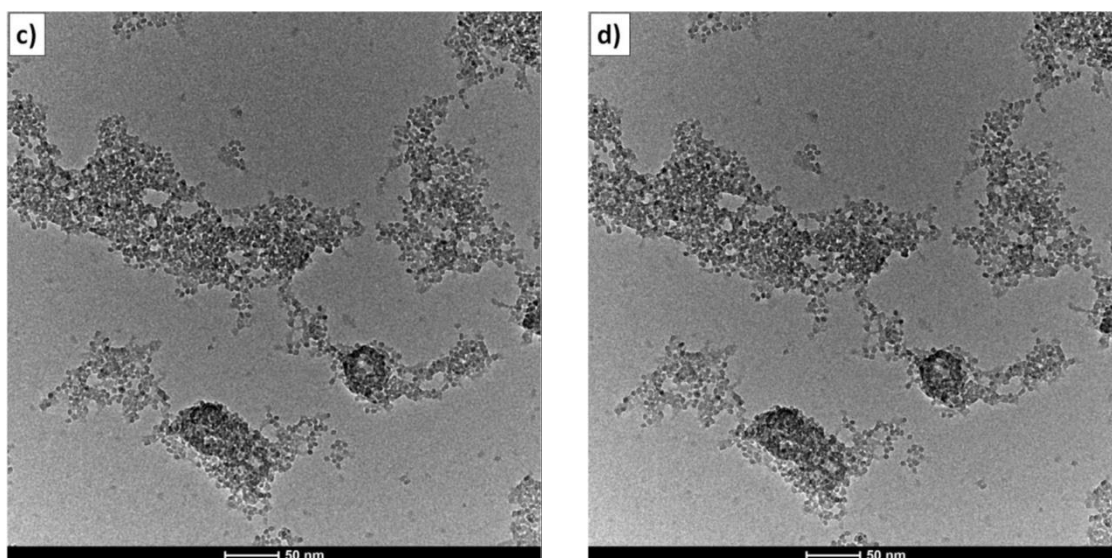
Figure 4.39 - Low magnification HRTEM images of mixed nanoparticles (CeO$_2$ and ZrO$_2$), a) 800°C for 0 min, b) 800°C for 90 min, c) 800°C for 90 min + 900°C for 120 min, and d) 800°C for 90 min + 900°C for 120 min + 950°C for 30 min.
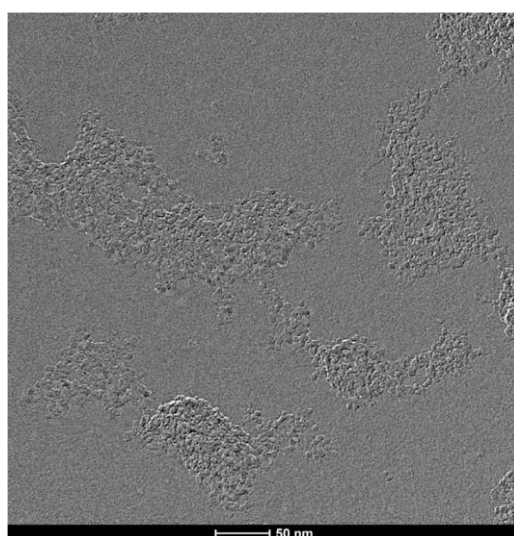
Figure 4.40 - Subtraction of the Figure 4.39a and Figure 4.39d.

After finishing the tests, the samples were cooled to room temperature, and the water circulator and the temperature controller were turned off. Then, high magnification HRTEM images were taken, with atomic resolution, to characterize the crystal structure and see if any phase transformation occurred during the tests (Figure 4.41). The acquisition of high magnification images of the smallest nanoparticles (below 5 nm) with atomic resolution at high temperatures, in this sample holder was not possible; same happens in other

acquisition modes (as Robert F. Klie *et. al.* quotes [83], the acquisition of high quality atomic-resolution Z-contrast images for temperatures higher than 500°C, with this kind of sample holder is tricky). The main reasons for this are: 1) thermal drift, which is inherent to the heating of the sample holder; 2) the turbulent flow of water through the circulation system, which is mandatory in operations above 500°C to prevent the heating to the rod of the stage; and 3) by electronic noise signals introduced by the SmartSet Hot Stage temperature controller when turned on (as shown on the Figure 4.42). Most of these problems can be mitigated with the use of MEMS grids, since only the grid is heated, there is no need of a cooling system and the thermal drift is greatly reduced.
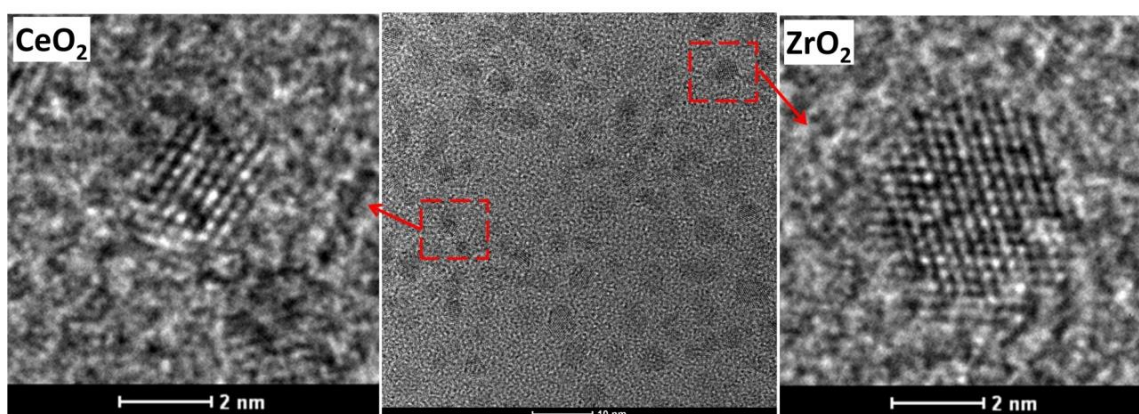
Figure 4.41 - HRTEM image of the sample heated at 800°C for 90 min + 900°C for 120 min + 950°C for 30 min, and cooled to room temperature.

To ensure that the lack of interaction between the particles was not due to a remnant of the organic layer on its surface, that was inhibiting the reactions; several samples were prepared and different treatments were employed to guarantee that the organic layer was completely removed. Dongguo Li *et al* evaluated several methods to remove the oleylamine surfactant, which includes thermal annealing, acetic acid washing, and UV-Ozone irradiation. Among these methods, the low temperature thermal annealing (≈185°C for 5 hours) in the air proved to be the most effective for the surface cleaning, without inducing particle size and morphology changes [84].
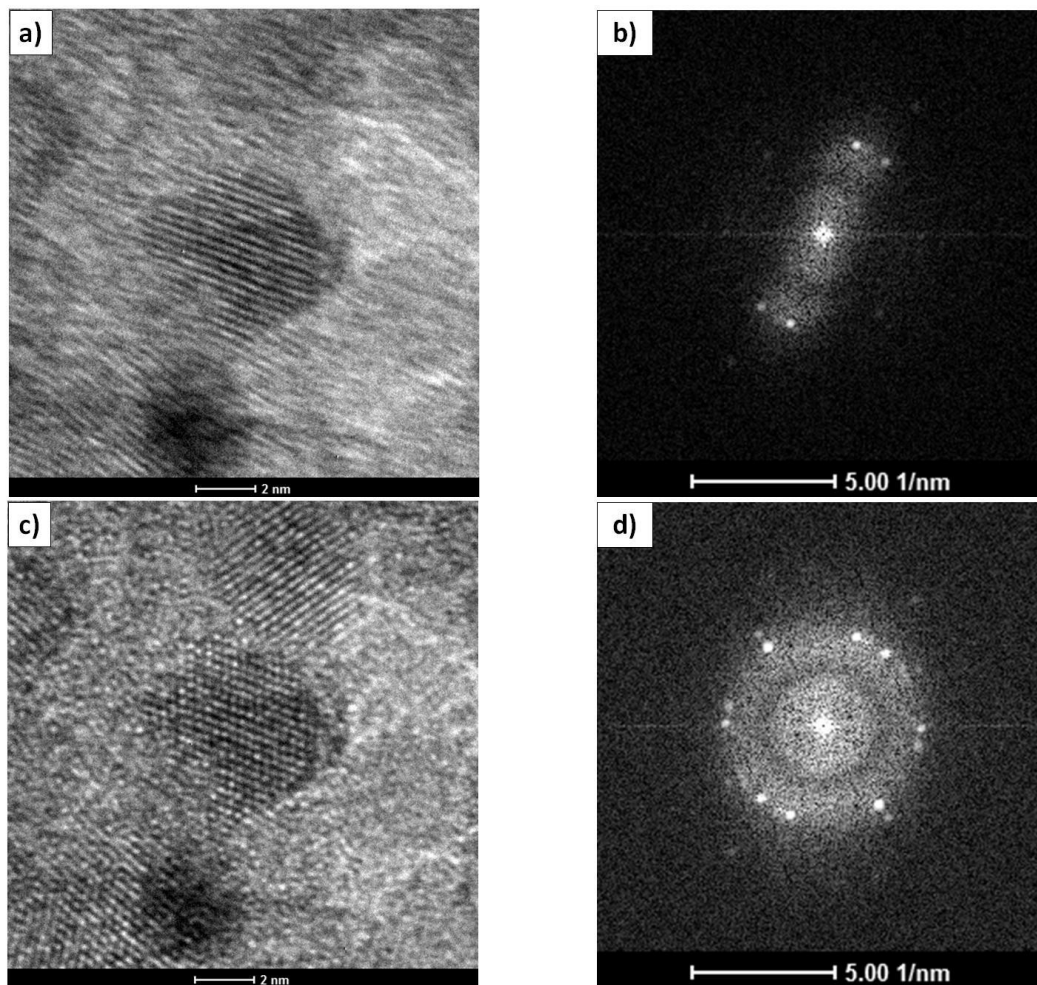
Figure 4.42 - HRTEM image at room temperature of some ZrO_2 nanoparticles with the SmartSet Hot Stage controller turned on a), and off c); and his respective FFT b) and d).

A mixture of the CeO_2 and ZrO_2 nanoparticles with 50-50 wt% was prepared and 1.0-1.5 µL of the dilution was drip over a silicon grid. To remove the organic layer, a heat treatment in air atmosphere was made, heating the sample at 185°C for 5 hours in a furnace. Figure 4.43 shows low magnification HRTEM images of an *in situ* test, where the sample was heated at 800°C for 60 min. As in the experiment shown in Figure 4.39, nothing happen. Figure 4.44a shows the subtraction of Figure 4.43a and Figure 4.43c; no significant variation between both image was observed.
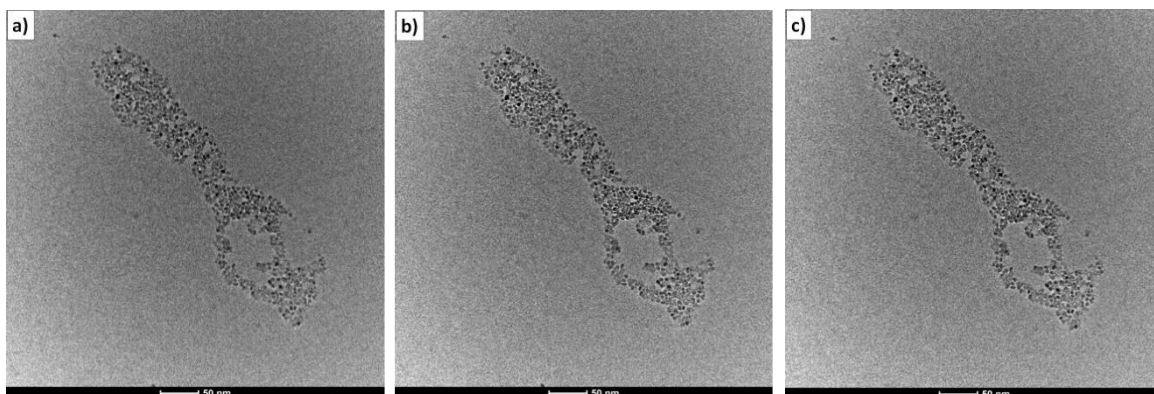
Figure 4.43 - Low magnification HRTEM images of mixed nanoparticles (CeO_2 and ZrO_2), after 185°C for 5 hours in a furnace with air atmosphere, to remove the organic layer, and heated *in situ* at 800°C for: a) 0 min, b) 30 min, and c) 60 min.
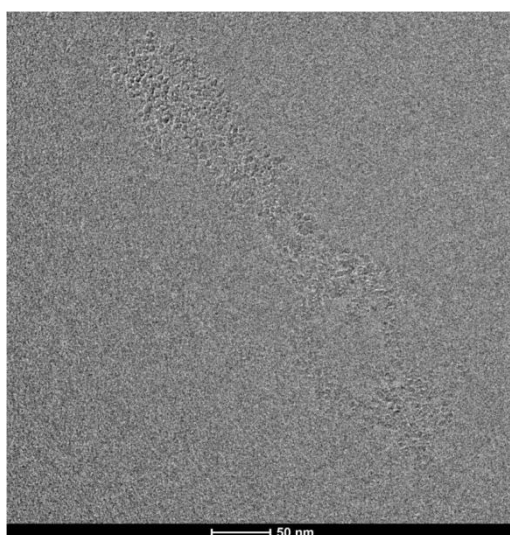
Figure 4.44 - a) Subtraction of the Figure 4.43a and Figure 4.43c.

Even with the treatment at 185°C for 5 hours, that proved to completely remove the organic surfactant (oleylamine), no interactions between the particles were observed. Thereby, other treatments at higher temperatures were tested, even if this could cause an agglomeration or an interaction of the nanoparticles before the *in situ* tests. Figure 4.45 shows the Thermogravimetric Analysis (TGA) and his Derivative thermogravimetry (DTG) of both oxides, CeO_2 and ZrO_2. It can be seen that the highest mass loss rate occurs at 449°C and 435°C for CeO_2 and ZrO_2, respectively.
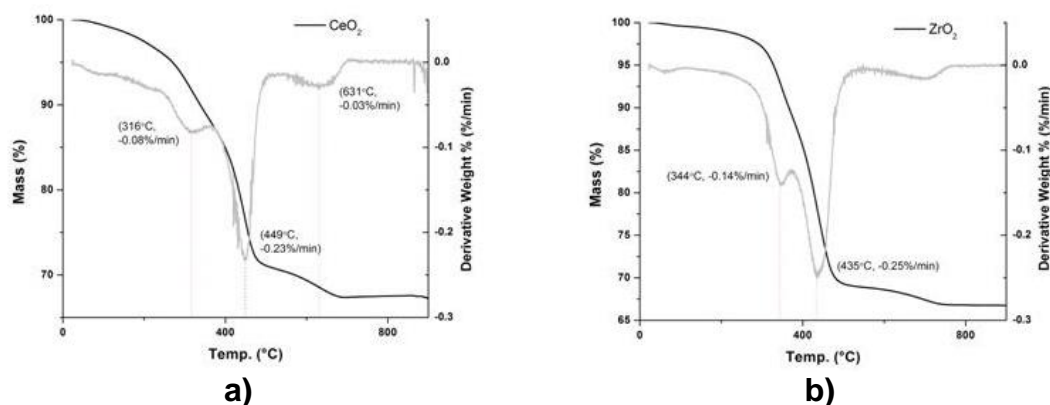
Figure 4.45 - TGA and DTG of: a) CeO_2, and b) ZrO_2 nanoparticles.

To evaluate if the CeO_2 was preventing the agglomeration and growth of ZrO_2 nanoparticles, samples with only ZrO_2 nanoparticles were prepared, and heat treatments to remove the organic layer were made at 185°C, 435°C, and 510°C for 5 hours. The sample was heated to 800°C for 60 min, as nothing happen, the temperature was increased to 900°C for other 60 min, as nothing happen the temperature was increased again to 1050°C for 180 min (Figure 4.46). Figure 4.47 shows the subtraction of Figure 4.46a and Figure 4.46c; only slightly changes were observed in the right part of the image, mainly related to the thermal expansion and not with changes in size or morphology of the particles.
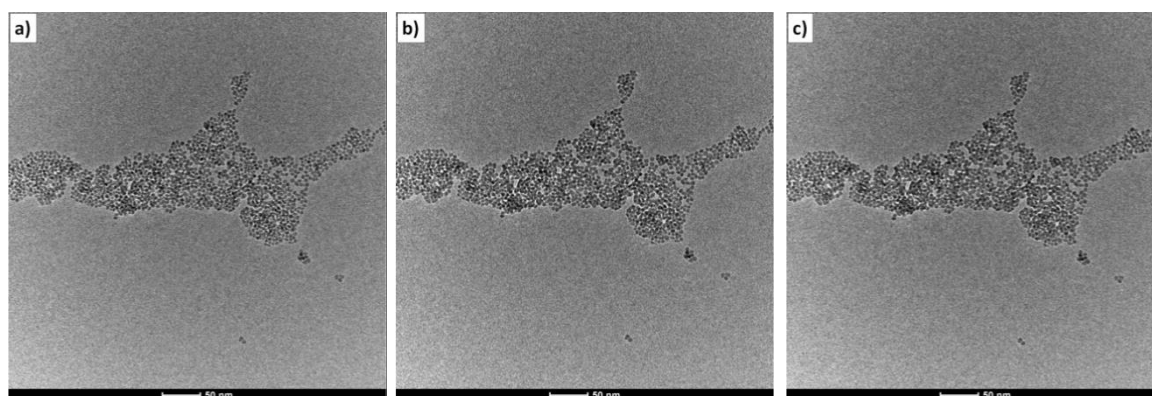
Figure 4.46 - Low magnification HRTEM images of ZrO_2 nanoparticles, after 510°C for 5 hours in a furnace with air atmosphere, to remove the organic layer, and heated *in situ* at 800°C for 60 min + 950°C for 60 min + 1050°C for: a) 0 min, b) 90 min, and c) 180 min.
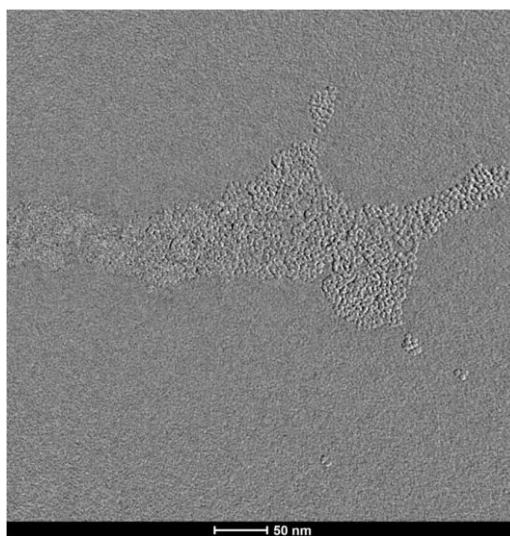
Figure 4.47 - Subtraction of the Figure 4.46a and Figure 4.46c.

A temperature of 1050°C is high enough to cause agglomeration of the nanoparticles, even at temperatures above 400°C has been known that ZrO_2 nanoparticles are sintered when the organic layer has been removed. In most of the cases when particles growth or sintering was reported, the particles were already in contact at the beginning of the experiments, or were close enough for small movements to cause the initial contact. In our case the particles are separated by the organic layer and after its deposition over the TEM grid, and subsequent removal of the organic layer, it seems that the particles are attached to the surface of the TEM grid; so they would not have any degree of freedom to move. Figure 4.48 shows the particle size distribution before and after the *in situ* test. Comparing the particle size distribution of the zirconia before and after the tests (4.6±0.8 nm and 4.4±0.8 nm) with the as-synthesized particles in Figure 4.21c (4.9±0.7 nm); there is not statistical variation in the size of the particles (i.e. the particles did not growth during the experiment), having an average size between 4 and 5 nm.
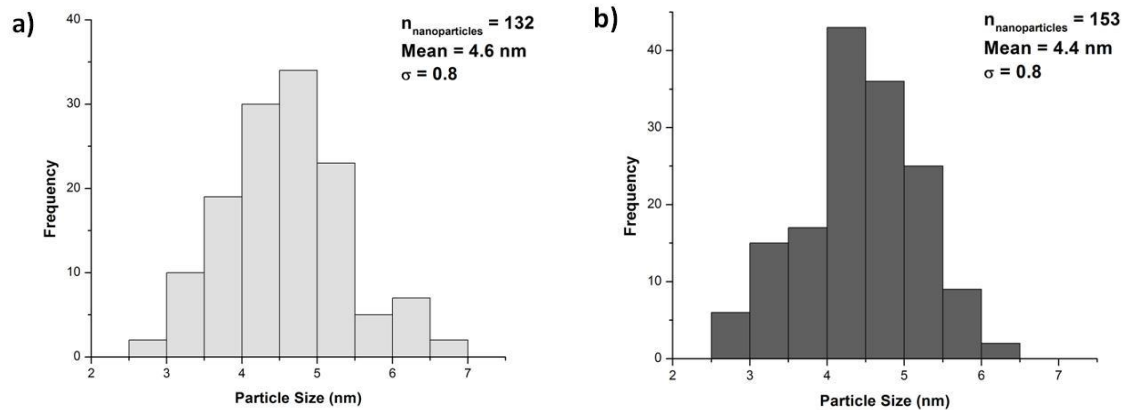
Figure 4.48 - Particle size distribution of ZrO_2 a) before, and b) after *in situ* heating at 800°C for 60 min + 950°C for 60 min + 1050°C for 180 min.

Let's take a break and understand how our particles are constituted and how they can interact with the surface of the films of the TEM grids. First of all we must understand that these oxide particles do not only have oxygen atoms inside the structure, but also are surrounded by oxygen atoms on the surface that help to chemically balance the charges of the metallic atoms. As an example, let's see a nanoparticle of CeO_2 of approx. 2.7 nm (Figure 4.49), assuming a perfect structure without any kind of defects, these particle would have 309 cerium atoms, and 480 oxygen atoms. To balance the charges, should be about twice oxygen atoms for each cerium atom, which means that we need about 138 additional oxygen atoms; obviously these atoms would be on the surface of the particle. The particle on the right side of Figure 4.49 is a more realistic approximation, has a total of 1029 atoms, being 309 cerium atoms, and 720 oxygen atoms.
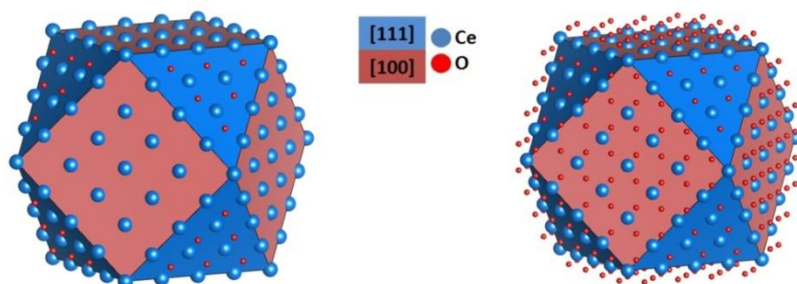
Figure 4.49 - Schematic representation of a CeO_2 nanoparticle, without and with oxygen atoms on its surface.

During the removal of the organic layer the carbon-oxygen bonds are broken, leaving oxygen atoms with free electrons that can react easily with the surface of the TEM grids (in this case Si_3N_4) forming silicon - oxygen bonds, which are very stable and difficult to break (even at temperatures as high as 1050°C). It is known that Si_3N_4 can oxidize when it is in the presence of CeO_2 or ZrO_2 (among others) [85,86], even at room temperature [87]. Curiously, a study conducted using various abrasives, like: boron carbide (B_4C), silicon carbide (SiC). aluminum oxide (Al_2O_3), chromium oxide (Cr_2O_3), zirconium oxide (ZrO_2), silicon oxide (SiO_2), cerium oxide (CeO_2), iron oxide (Fe_2O_3), yttrium oxide (Y_2O_3), copper oxide (CuO), and molybdenum oxide (Mo_2O_3); found that the CeO_2 and ZrO_2 were the most effective, since they oxidized the surface making easier the Chemo-mechanical polishing of the Si_3N_4 [86].

Now we know that the metal oxide nanoparticles react with the TEM grids, and that the mobility is so limited that they must be agglomerated before the beginning of the experiments, in order to have a possibility that they can interact. The next step is to prepare new samples in grids coated with α-C film and with a higher concentration of nanoparticles. To do this, 3 drops with 2.0 µL of the dilution were drip over the grid (a total of 6.0 µL). Dripping one drop, drying naturally, and dripping again. To remove the organic layer, the sample was heated at 185°C for 5 hours in air atmosphere. It's worth remembering that, since Cu grids have a limited range of working temperatures, the maximum temperature for the *in situ* tests will be 500°C. Figure 4.50 shows the particles after 420 min at 500°C, during the first part of the experiment the EBCD was 800 A/m^2, as nothing happen after 180 min the EBCD was increased to 14000 A/m^2 for another 240 min.

We can see that there is a synergy between the temperature and the EBCD. After the first 60 minutes with a high EBCD (Figure 4.50b) the particles began to sinter. The red arrow marks a region where some "nanopores" appear due to the sintering of the neighboring nanoparticles. The yellow arrow in Figure 4.50d shows the reduction of a hollow region due to the agglomeration of the surrounding nanoparticles; the same phenomenon was observed on the

100

others hollow regions. After 240 min of irradiation with a high EBCD at 500°C (Figure 4.50d), most of the nanopores have disappeared due to the sintering of the nanoparticles. The high EBCD damage the Carbon film of the TEM grid causing shrinkage, this allows contact between the particles, initiating the sintering.
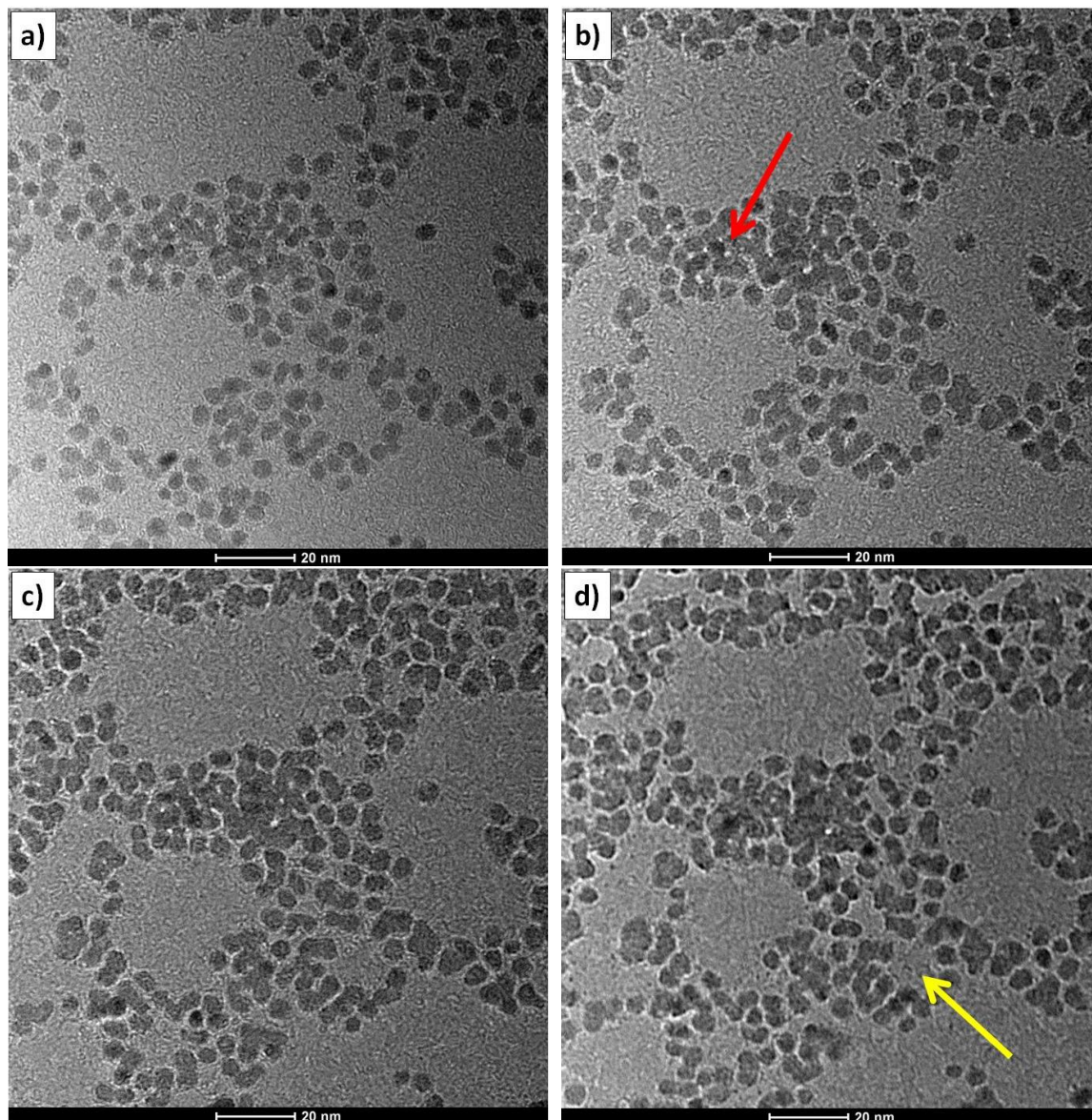
Figure 4.50 - Low magnification HRTEM images of ZrO_2 nanoparticles heated *in situ* at 500°C for 180 min at low EBCD plus: a) 0 min, b) 60 min, c) 120 min, and d) 240 min at a higher EBCD.

Figure 4.51 shows the particles before and after 420 min at 500°C, at the start of the test Cu nanoparticles appears, as reported Zhang *et al* [77]. Curiously, the ZrO_2 nanoparticles that were not affected by the electron beam (outside of the irradiation zone) did not grow or sintered, but a significant growth was observed in the Cu nanoparticles. This may be due to the low melting point of metallic copper compared with the metal oxides. The fact that the Cu nanoparticles grow indicates that there are Cu ions moving through the Carbon film; how these ions affect the interactions between the oxide nanoparticles is not clear. To avoid this other TEM grids can be used, like Mo or Au grids.
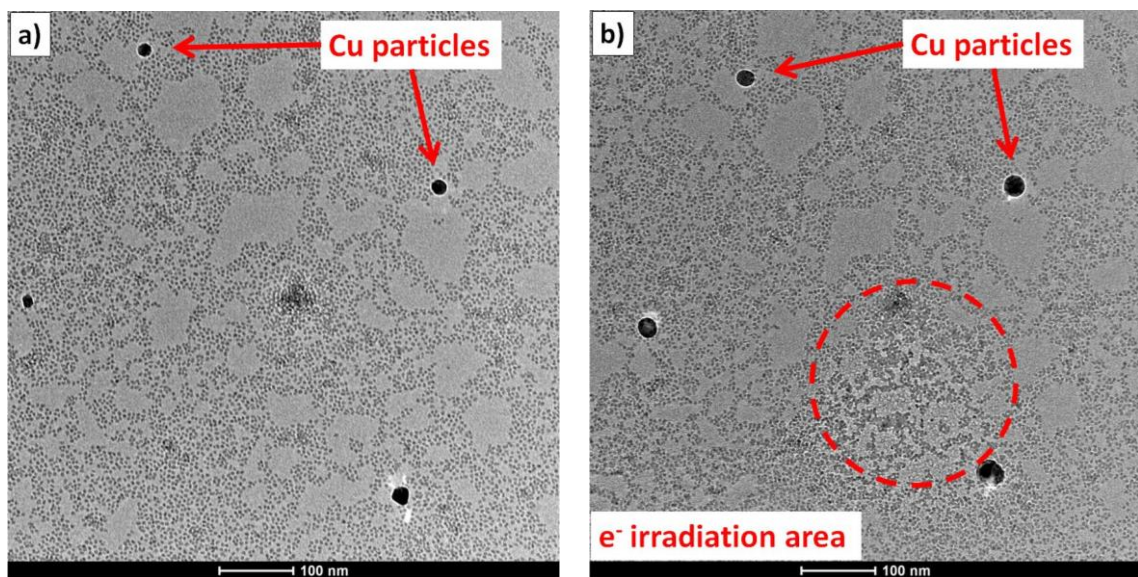
Figure 4.51 - Low magnification HRTEM images of ZrO_2 nanoparticles heated *in situ* at 500°C for: a) 0 min, and b) 420 min.

In a general way we can conclude that the *in situ* heating experiments are a powerful tool to follow the sintering process of nanoparticles. Other experiments with higher concentration of nanoparticles can be made in the future, which allows more contact between particles at the beginning of the test and avoid the use of high EBCDs. Also, TEM grids of Mo or Au can be used, which allow higher temperature tests.

Figure 4.52 - Low magnification HRTEM images of mixed nanoparticles (CeO_2 and ZrO_2) heated *in situ* at 500°C for: a) 0 min, and b) 180, c) 240min, and d) 360 min.

Similarly, a mixture of CeO_2 and ZrO_2 nanoparticles (50 wt%) was prepared on a Cu grid with 3 drops of the dilution (6.0 µL total). Figure 4.52 shows a sequence of images during an *in situ* test, for 360 min at 500°C, irradiated with an EBCD of 1500 A/m^2. A slight growth of the particles was observed. For the times and temperatures evaluated, no interactions between the CeO_2 and ZrO_2 particles, to create a new phase, were identified. Probably the energy needed to create a new crystal structure (like tetragonal $Ce_{0.5}Zr_{0.5}O_2$) starting from already stable structures (cubic CeO_2, and cubic ZrO_2) is too

high, and the temperatures used are not enough to promote these phase transformations. As Figure 4.53 shows, the main mechanism of interaction was oriented attachment.
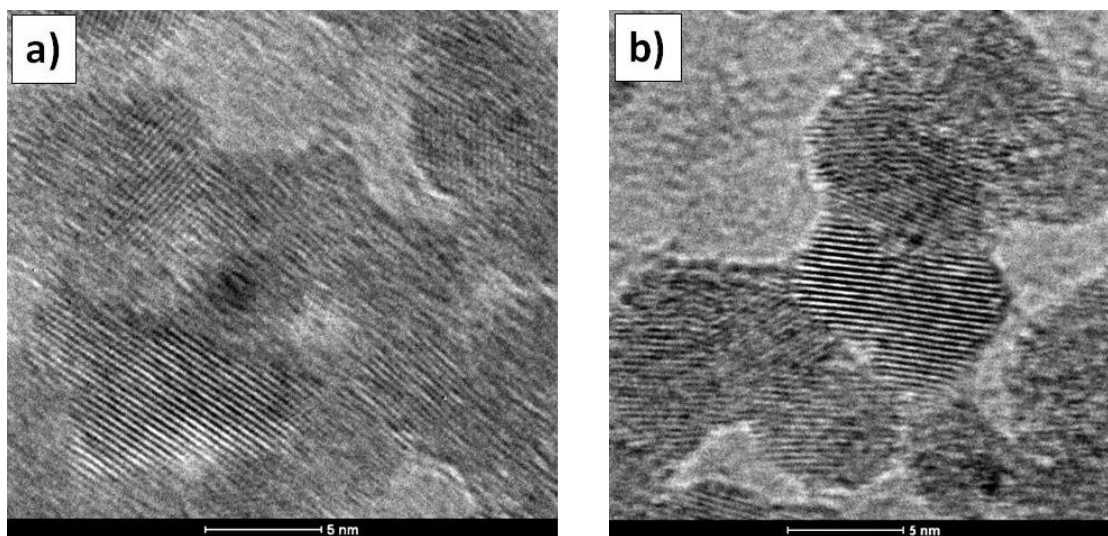
Figure 4.53 - HRTEM images of mixed nanoparticles (CeO_2 and ZrO_2) heated *in situ* at 500°C for 360 min.

In other test, the mixture of CeO_2 and ZrO_2 nanoparticles (50 wt%) was dripped on a Si_3N_4 grid with 3 drops of the dilution (6.0 µL total). Figure 4.54 shows low magnification images before and after an *in situ* test, for 360 min at 950°C, irradiated with an EBCD of 15000 A/m^2. Severe damage on the silicon membrane can be noted within the irradiation area. Also, the nanoparticles that are not agglomerated and that are within the irradiation area, indicated by the yellow arrow in Figure 4.54a, were vanished due to electron beam damage. The particles that were not irradiated during the *in situ* heating, indicated by the blue arrows in Figure 4.54b, remained unchanged. Once again, this shows how a high EBCD can affect the samples during the *in situ* tests.

Figure 4.55 shows a zoom in an area that was not affected by the electron beam during the *in situ* test. Although the nanoparticles are agglomerated, due to the removal of the organic layer before the test, it is possible to appreciate the contours of the particles (Figure 4.55a). After 360 minutes at 950°C, most of the contours between the particles have disappeared, and a densification can be observed (Figure 4.55b).
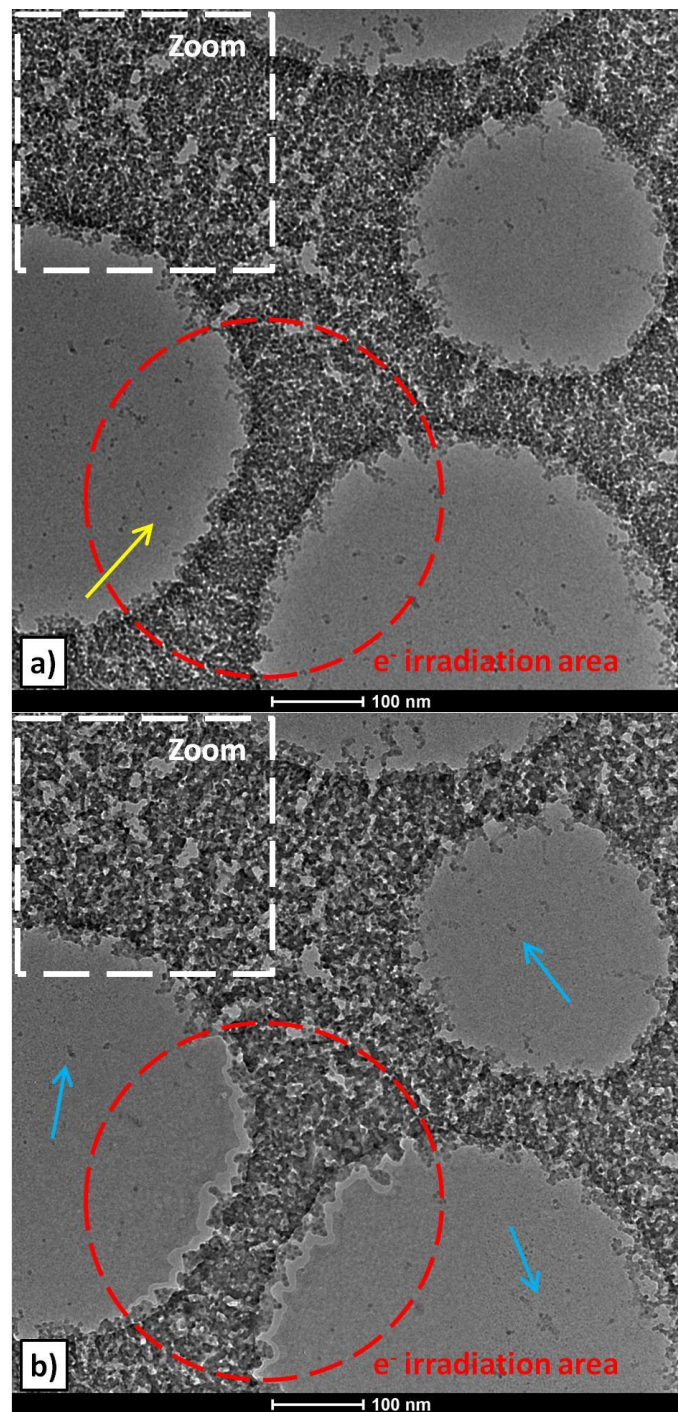
Figure 4.54 - Low magnification HRTEM images of mixed nanoparticles a) before, and b) after *in situ* heating at 950°C for 360 minutes. The red circle highlights the irradiation zone, the yellow and blue arrows shows isolated nanoparticles inside, and outside of the irradiation area, respectively.
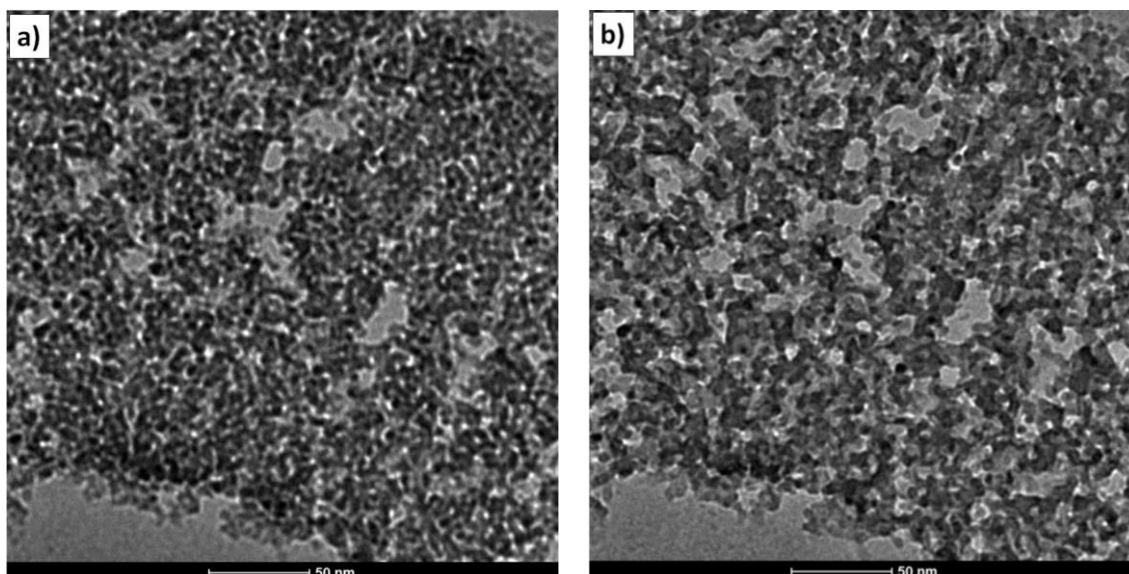
Figure 4.55 - Zoom of the areas marked with the white square in Figure 4.54a, and b respectively.

Figure 4.56 shows a sequence of images during the *in situ* test. During the first 30 minutes, no significant changes were observed. Between minutes 30 and 60, in areas with higher particle density (e.g. yellow arrow in Figure 4.56b and c), the first stages of sintering begin to be appreciated, creating more necks between adjacent particles, decreasing the interfaces. Between minutes 60 and 120, most of the interfaces between particles disappear (e.g. blue arrow in Figure 4.56c and d), giving way to the densification process. At minute 150 the first visible signs of beam damage appear on the Si_3N_4 membrane. It could be said that between minutes 180 and 240, the whole densification process is completed; no significant changes was observed between minutes 240 and 360.

Figure 4.57 shows low magnification HRTEM images of the mixed nanoparticles before and after the *in situ* test at 950°C. As previously discussed, the contours between particles can be easily identified before the tests, but they disappear during the tests. It might seem that there was a growth of the particles.

106
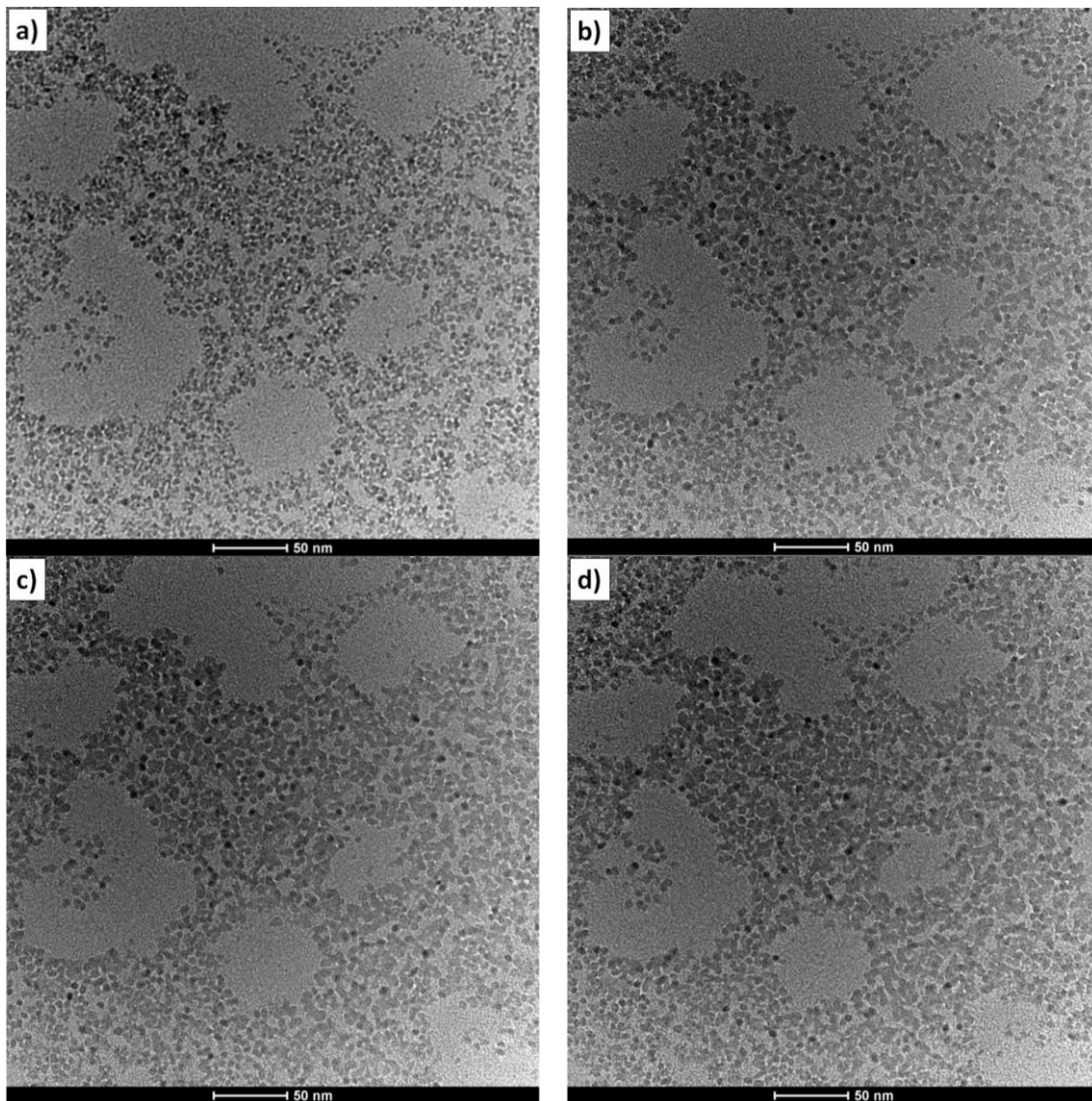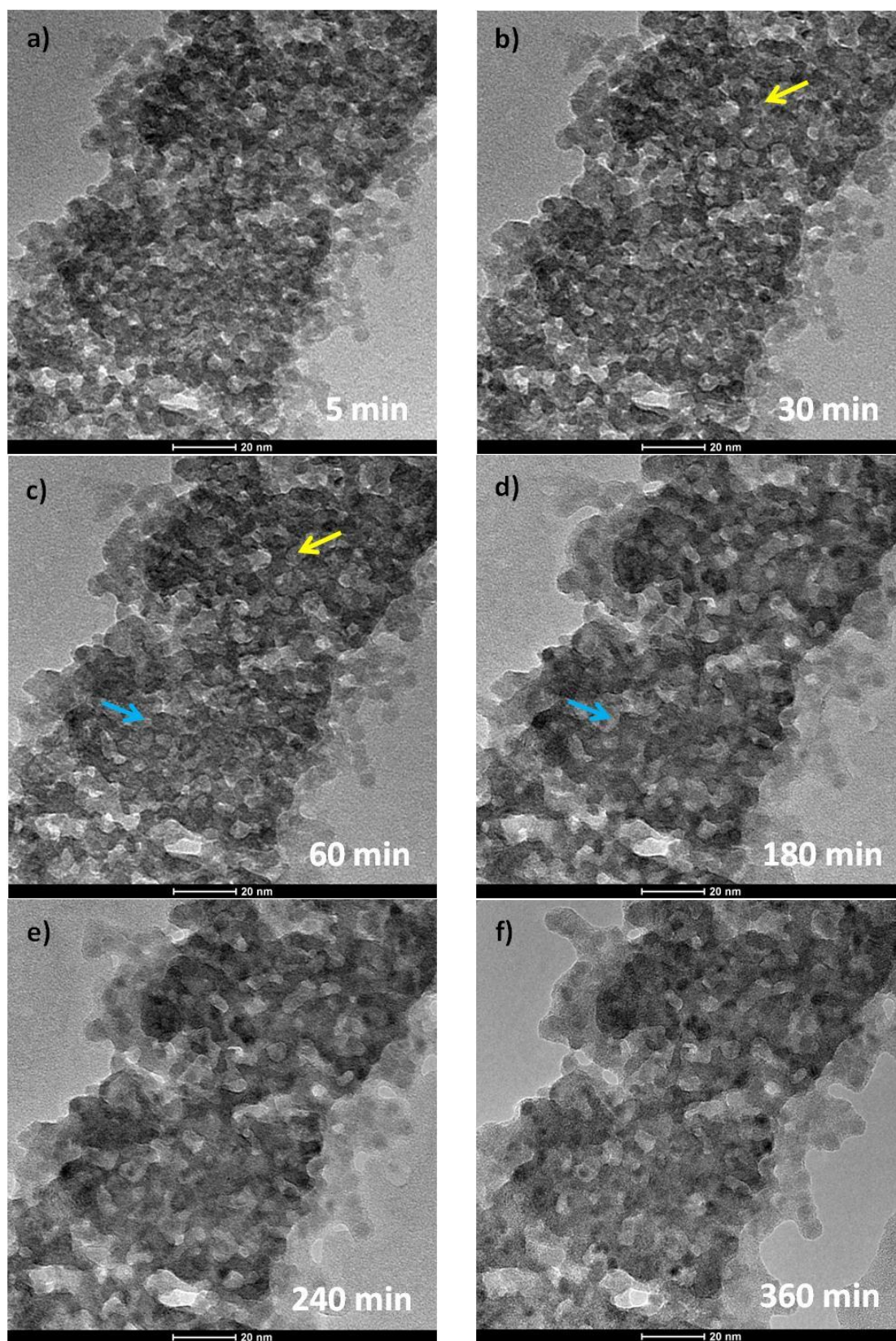

Figure 4.56 - Low magnification HRTEM images of mixed nanoparticles (CeO_2 and ZrO_2) heated *in situ* at 950°C for: a) 5, b) 30, c) 60, d) 180, e) 240, and f) 360 minutes.
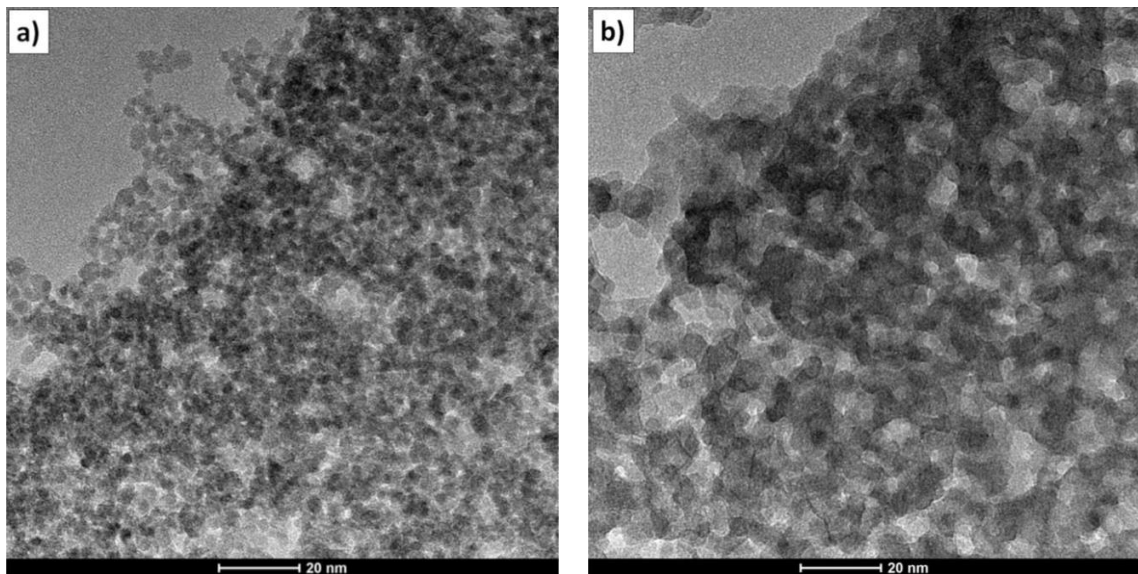
Figure 4.57 - Low magnification HRTEM images of mixed nanoparticles (CeO$_2$ and ZrO$_2$) a) before, and b) after *in situ* heating at 950°C for 360 minutes.

Looking closely, can be observed that before the test the nanoparticles are agglomerated and randomly oriented (Figure 4.58a), after 360 minutes at 950 degrees the nanoparticles are more aligned (Figure 4.58c), so it seems that they were a single crystal and there was no interface between them. The FFT of the images shows more clearly how before the test (Figure 4.58b) the spots are not well defined since the particles are randomly oriented creating diffraction rings. On the other hand, after the test (Figure 4.58d) the spots are well defined showing that more particles are oriented in the same direction; even the outer spots can be identified, corresponding to the {202} plane of zirconia.
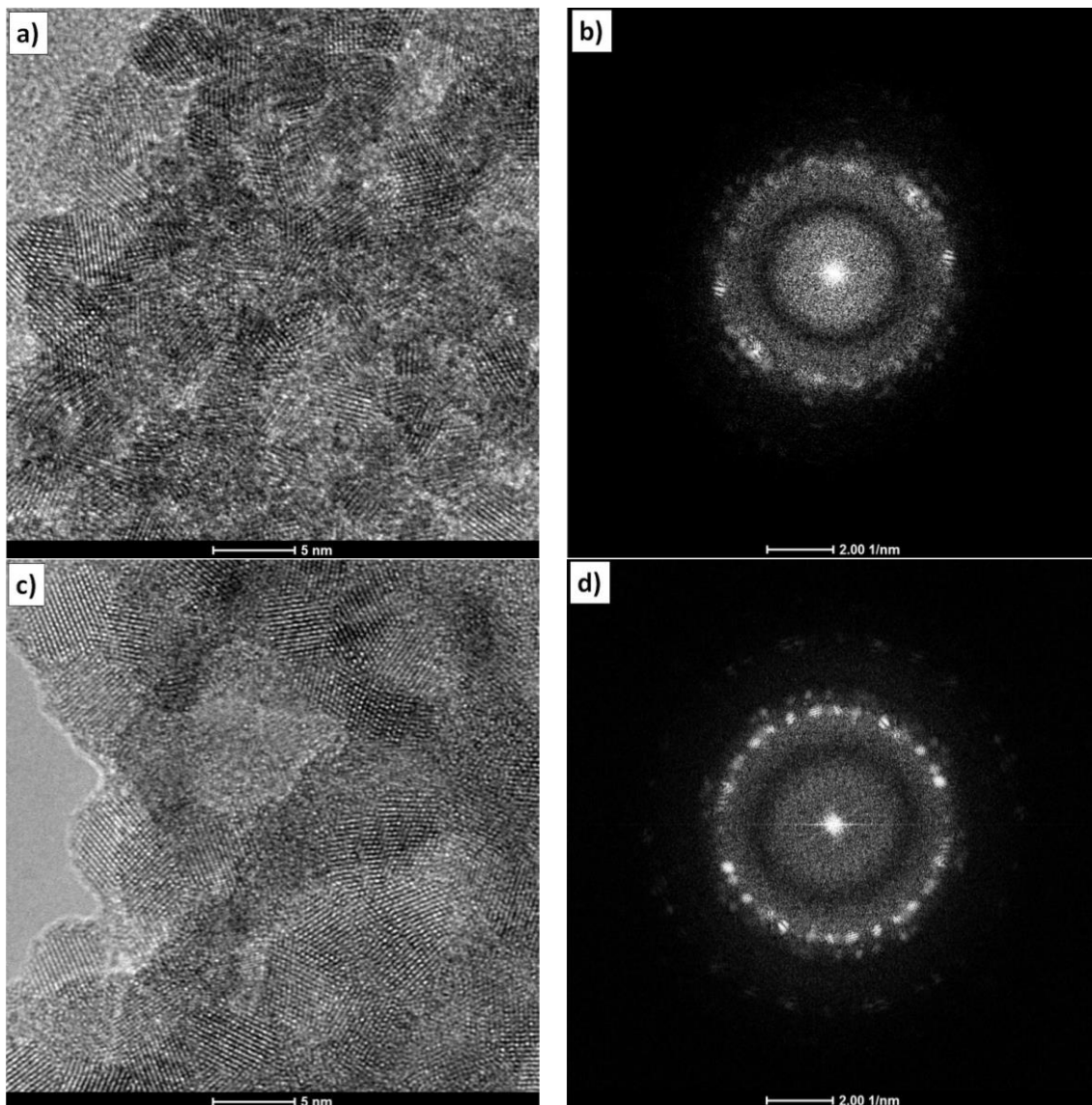
Figure 4.58 - HRTEM images, and his respective FFT, of mixed nanoparticles (CeO$_2$ and ZrO$_2$) before a) and b), and after c) and d) *in situ* heating at 950°C for 360 minutes.

Figure 4.59 shows a HRTEM image of some nanoparticles bonded after an *in situ* test at 950°C for 360 minutes. It can be seen that each particle has its own orientation and have sizes close to the originals, so it is ruled out that there has been growth during the test. The particles have coherent interfaces when the angle of misorientation is very low, and semi-coherent interfaces for larger angles. This indicates that, when they are over other particles, they have enough degrees of freedom to rotate and look for a preferred orientation with neighboring particles. This is why the contours between the particles cannot be

identified after the tests (at lower magnifications). On the APPENDIX B (Figure B.6 and Figure B.7) more images can be found, showing the same behavior.

Figure 4.59 - HRTEM images of mixed nanoparticles (CeO_2 and ZrO_2) after *in situ* heating at 950°C for 360 minutes.

In summary, for our testes conditions; mixed nanoparticles of CeO_2 and ZrO_2 (deposited on a Si_3N_4 grid) heated *in situ* at 950°C for 360 minutes did not interact. We could conclude that, it was not possible to observe growth of particles, but densification was observed when the particles are close enough at the beginning of the tests. This densification process includes a rearrangement of the particle to bond together by oriented attachment; whether perfect oriented lattices, generating twins, or interfaces with low-angle misalignments. Then, atom diffusion disappear most of the surfaces between the nanoparticles, but keep the crystallite size close to the initial size of the nanoparticles.

Generally, the main mechanism of interaction between the nanoparticles was oriented attachment. Even in conditions where oxides of CeO_2 and ZrO_2 are mixed together, only interactions between those of the same species were

observed. Since no reactions were observed between cerium and zirconium oxides, which were the most similar and in which more interactions were expected to occur, it was decided not to run the tests between mixed oxides of cerium and tin; however, the synthesis and characterization of tin oxide nanoparticles is available in the APPENDIX A.

Dongsheng Li *et al.* [58]; and Chao Zhu *et al.* [59] performed *in situ* tests at room temperature in liquid cells, in these conditions the nanoparticles (between 2-10 nm) had all the degrees of freedom. The main growth mechanism was, also, oriented attachment, followed by atomic diffusion through "the interface".

The behaviors observed in our experiments are representative of a vacuum environment. It is difficult to predict how the particles behave in an oxygen-rich environment, for example. Since the substrate (carbon film, or Si_3N_4 membrane) can oxidize when in contact with oxygen at high temperatures, which could change the way it interacts with the particles... and in the same way change the way in which the particles interact with each other.

4.6 The *in situ* tests in the literature

One of the main shortcomings found in the literature is that the electron beam current density (EBCD), that is an approximation of the energy deposited in the sample, is not reported. This makes it difficult to compare results, even if they have similar conditions of temperature or particle size. Even today, which is well know that the electron beam affects the samples, and to a large extent; few studies indicate whether, or not, this has a significant effect on the results presented.

Another problem is the lack of knowledge about the interactions between the samples and the films on the TEM grids. We know that there is a decrease in the degrees of freedom, since a particle in a fluid can move in 3D space and rotate freely, whereas in a substrate it can only be moved in 2D and sometimes it has the rotation compromised (depending on the roughness of the substrate and the size of the particle). What we do not know is how strong are the

interactions between particles and substrates, and how does this affect their mobility. In the literature this topic has not been addressed directly. From what we have seen in this work, oxides create strong bonds with the silicon nitrites membranes, whereas metal nanoparticles probably creates weaker bonds that are easily broken with the increase of the temperature, or with the help of the electron beam.

The vast majority of *in situ* tests reported in the literature, where sintering occurs successfully (or reactions between particles), start from nanoparticles that were already in contact before beginning the experiments. The lack of mobility of the nanoparticles on the TEM grids can explain this void in the literature. To mitigate this, new sample holders that allow the observation of liquid samples inside the microscopes are under development, Figure 4.60 [58].
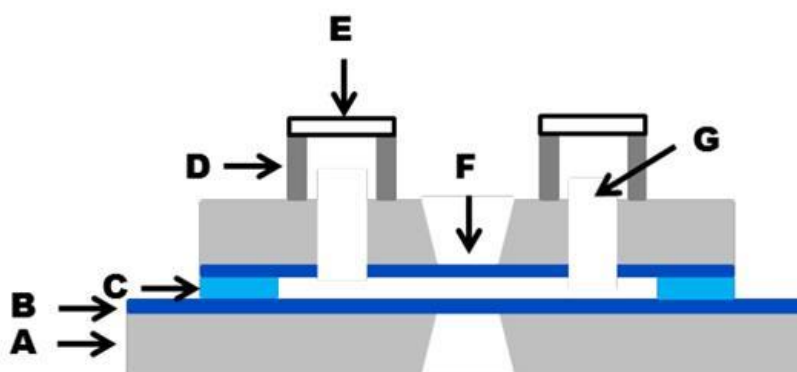
Fig. S1.

Schematic cross-section of the in situ TEM cell cross section viewed. Components: A: Si wafer, B: 50-100 nm Si_3N_4 membrane, C: Si_3N_4 spacer 450 nm, D: Si tower, E: Glass cap, F: Electron transparent Si_3N_4 membrane window, G: Solution reservoir.

Figure 4.60 - Schematic representation of a liquid cell design that can be introduced inside a TEM [58].

Lee *et al.* showed the coalescence of titanium oxide nanoparticles (Figure 2.14), in those experiments they start from aggregate particles and the EBCD was not reported. As observed, since the particles are already in contact there are no problems with the mobility and the sintering and growth is achieved with an increase of the temperature up to 800°C. Even with the aid of

temperature and with bonded particles, the mechanism that triggers the growth is a phase transformation; so even in favorable conditions, the particle growth can be difficult to obtain.

Cordeiro M. conducted several *in situ* experiments of synthesis and growth of cerium oxide nanoparticles [88], using nickel and molybdenum TEM grid; the EBCD was not reported. Figure 4.61 shows the sintering of two cerium oxide nanoparticles; at the beginning of the experiment the particles are very close, already in contact in a small area of their surfaces (minute 2). As time passes, the particles get closer and the contact area increases, starting the sintering process (minute 7 to 18), and forming a single crystal. After 30 minutes, the sintered particle begins to grow without being in contact with other nanoparticles; the author attributes this growth to the diffusion of cerium atoms (or clusters) through the surface of the substrate.

Analyzing Figure 4.61, we can see that over time the carbon film becomes brighter. As we discussed earlier, this is due to a decrease in the carbon film thickness due to beam damage. Figure 4.62 shows a zoom of Figure 4.61f; after 38 minutes a vacuum region is observed, highlighted in red. We cannot know what was the EBCD used in these experiments, nor how is the synergistic effect between the EBCD and the temperature, but even with the beam effect a growth of the particles can be observed, different when only beam damage is present (Figure 4.38).

Figure 4.38 shows that a high EBCD can sputter the atoms from the nanoparticles; these atoms could diffuse to the surface of the carbon film and assist the growth of the bigger nanoparticles. Nevertheless, we know that high EBCD can promote the agglomeration of nanoparticles at room temperature, so the dissolution, sintering and growth of nanoparticles cannot be attributed only to the temperature, as long as there is a pronounced effect of the electron beam.
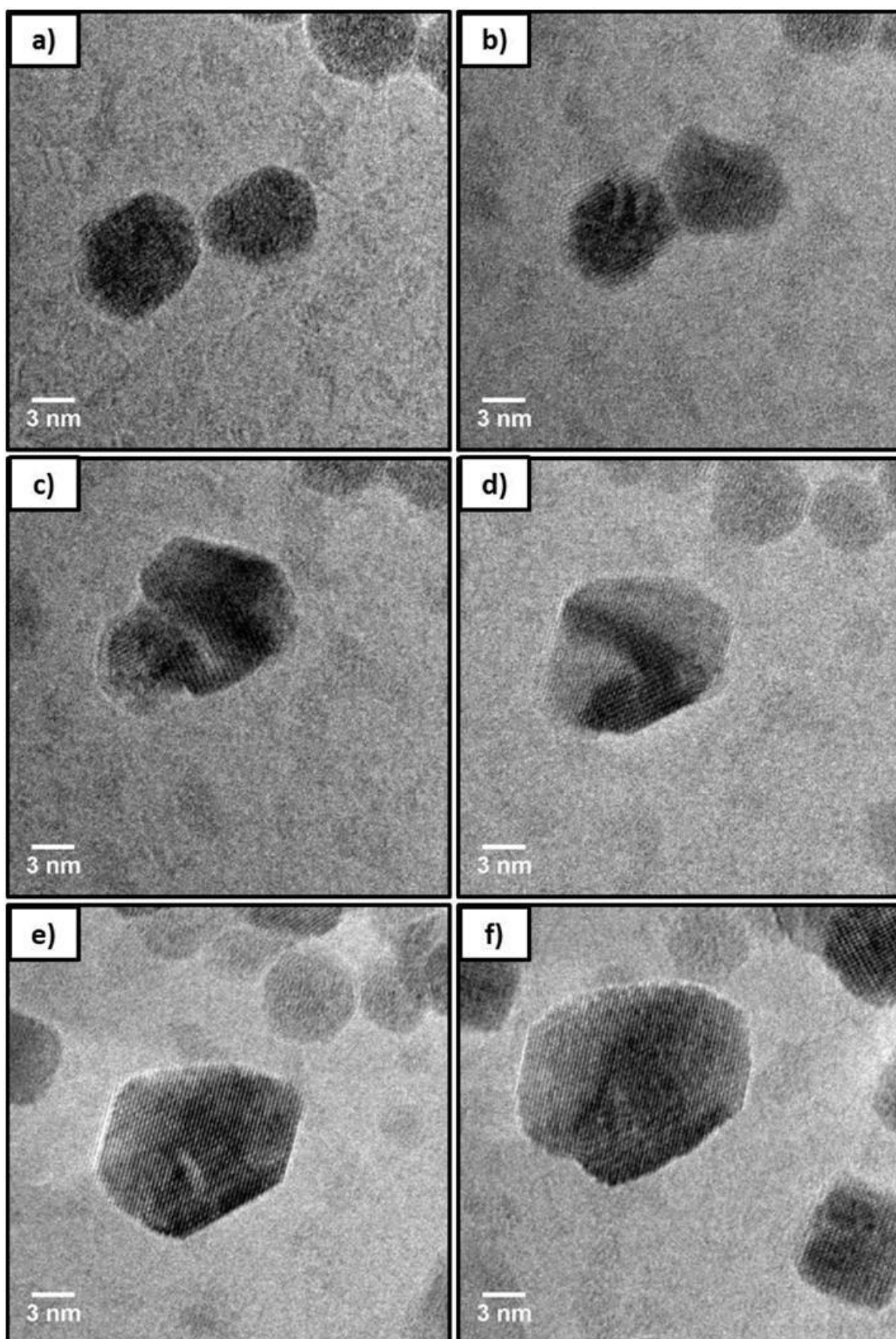
Figure 4.61 - Sintering of CeO$_2$ nanoparticles at 890°C in vacuum. a) 2 min, b) 7 min, c) 11 min, d) 18 min, e) 31 min and f) 38 min [88].
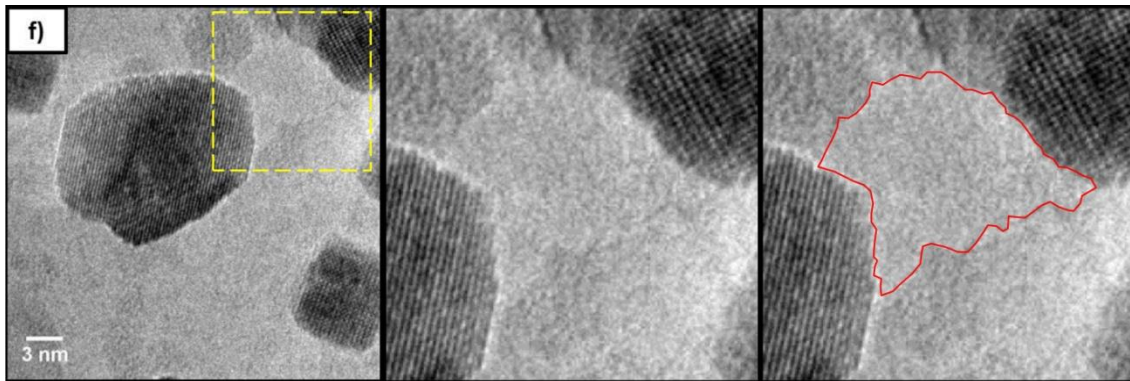
Figure 4.62 - Zoom of Figure 4.61f. The area highlighted in red indicates a region of the carbon film that was removed due to beam damage. Adapted from [88]

Looking at the sintering process, we can observe that even when the nanoparticles come into contact (minute 7, Figure 4.61b), the sintering process does not began until a rearrangement (rotation) of the nanoparticles occurs (minute 18, Figure 4.61d). Between minutes 7 and 11, the dimensions of the nanoparticle on the left do not change; it only seems smaller by an optical illusion, since the particle on the right is bigger because it grew by atom diffusion through the carbon film surface.

Figure 4.63 shows the sintering process of CeO_2 nanoparticles at 890°C from minutes 11 to 18. It can be seen that although the nanoparticles are bonded (Figure 4.63b), the contour of particle 1 can be easily identified on particle 2. Figure 4.63c and Figure 4.63d shows a zoom over the particles, a change in the orientation of the crystallographic planes can be observed, only after this rearrangement a complete sintering of both particles was observed. White and yellow lines serve as reference for assessing the change in orientation. We can assume that the sintering between both particles was assisted by oriented attachment. In this case, the sintering process by orientation attachment was more efficient than by mass transfer through the grain boundary. Perhaps in systems with less degrees of freedom, the mass transfer through the grain boundary have more relevance.
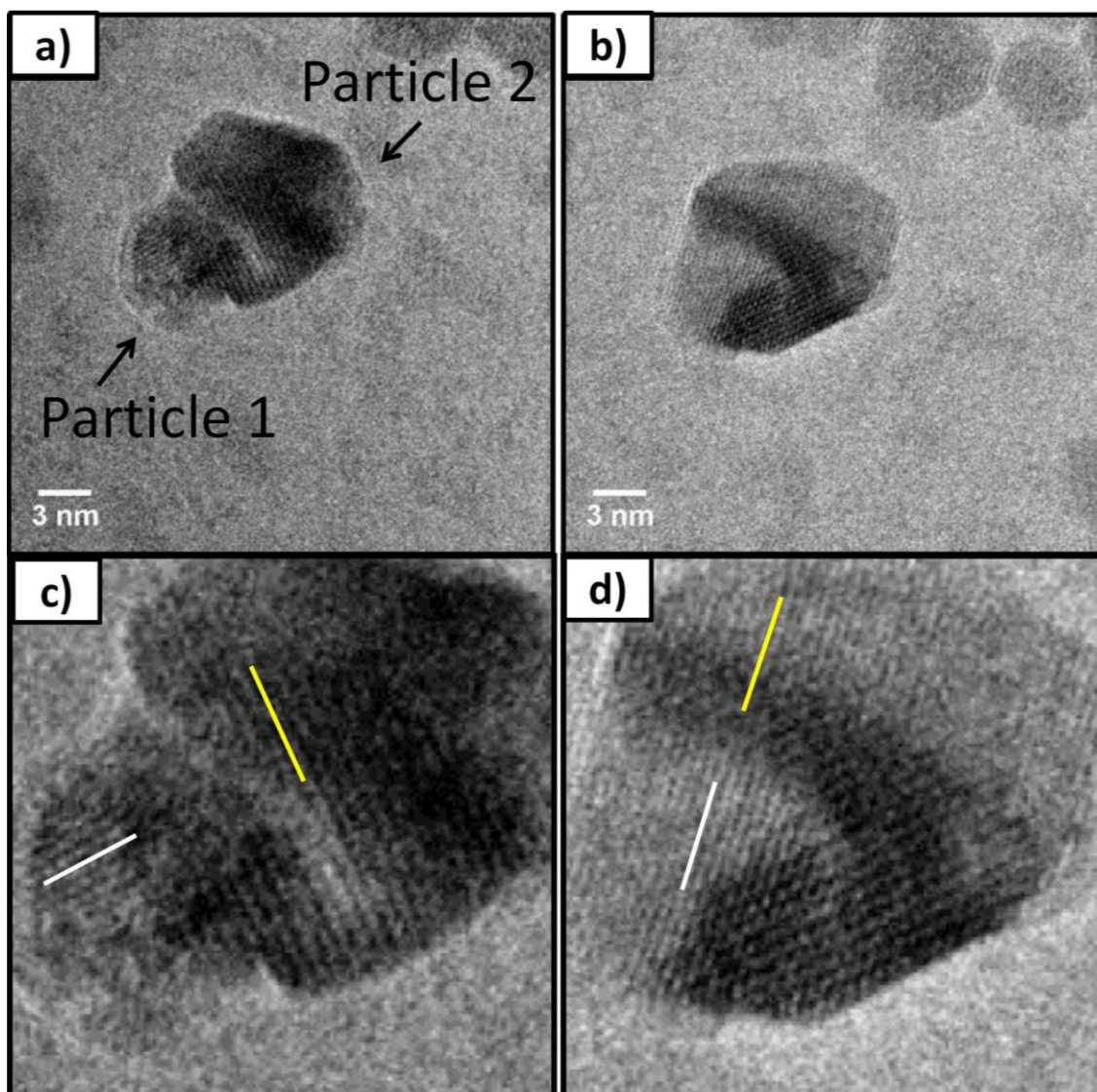
Figure 4.63 - Sintering of CeO$_2$ nanoparticles at 890°C in vacuum. a) 11 min, b) 18 min; c) and d) zoom of a) and b) respectively. Adapted from [88].

In others *in situ* heating experiments, Gonçalves R.H. evaluated the ability of tin (Sn) to inhibit the growth of iron oxide nanoparticles [79]. The Sn was used as a dopant on the surface of the nanoparticles. The nanoparticles were deposited over Si$_3$N$_4$ TEM grids. The tests were performed at 750°C, and neither the exposure time of the particles at high temperature, or the EBCD used during the tests were reported. Figure 4.64 and Figure 4.65 shows low magnification HRTEM images of pure γ-Fe$_2$O$_3$, and Sn doped γ-Fe$_2$O$_3$ (respectively), before and after the *in situ* heating experiments. Before the experiments the mean diameter of the nanoparticles was 12 nm, both for the

doped and undoped condition, after the *in situ* tests the size distribution was broadened from 8 to 100 nm for the undoped, and from 8 to 40 nm for the Sn doped condition (Figure 4.66). The author claims that the Sn^{4+} added on the surface of the nanoparticles reduces the grain boundary sliding, due to its low diffusion rate, decreasing the growth rate of the iron oxide.

Analyzing Figure 4.64b and Figure 4.65b, we can see that only some nanoparticles grew, others kept their initial size. If temperature is the driving force that determines the growth of the nanoparticles, they should all have grown (which did not happen). We know that the oxides can bond with the silicon film, which limits its movement; we also know that the nanoparticles must be in contact to promote growth. Comparing Figure 4.64 and Figure 4.65, we can see that the sample where the nanoparticles grew the most is also the sample with more particles in contact (before starting the test). By increasing the number of nanoparticles in contact at the beginning of the experiments, the final size may be affected, since there is a greater amount of mass available for the final particle.
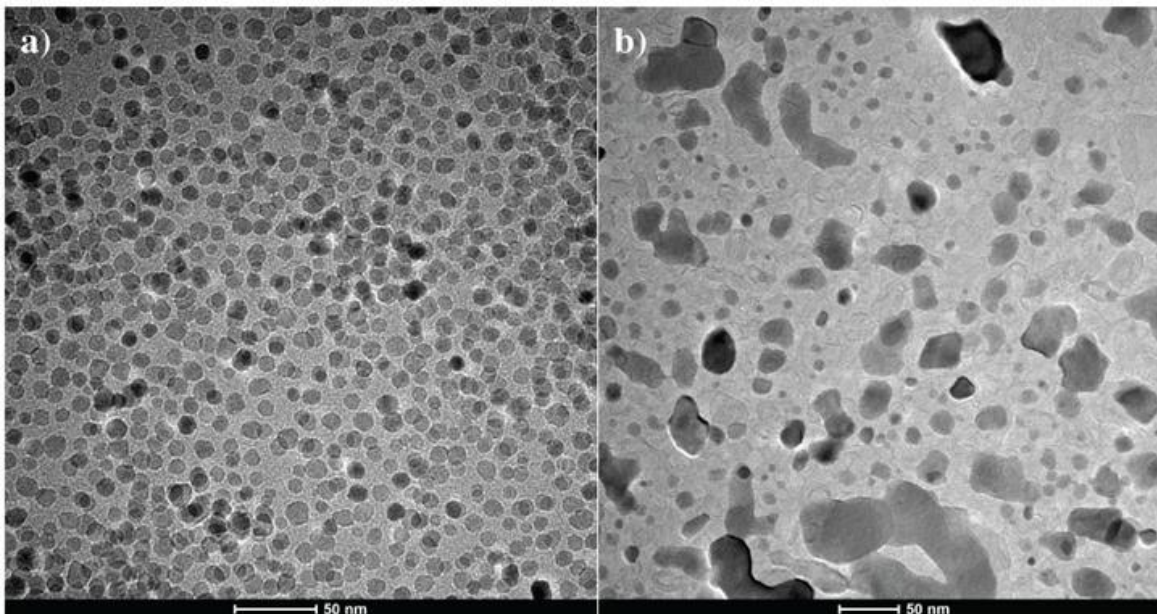
Figure 4.64 - Low magnification HRTEM images of *in situ* experiment of pure γ-Fe_2O_3, a) before and b) after heating at 750°C [79].
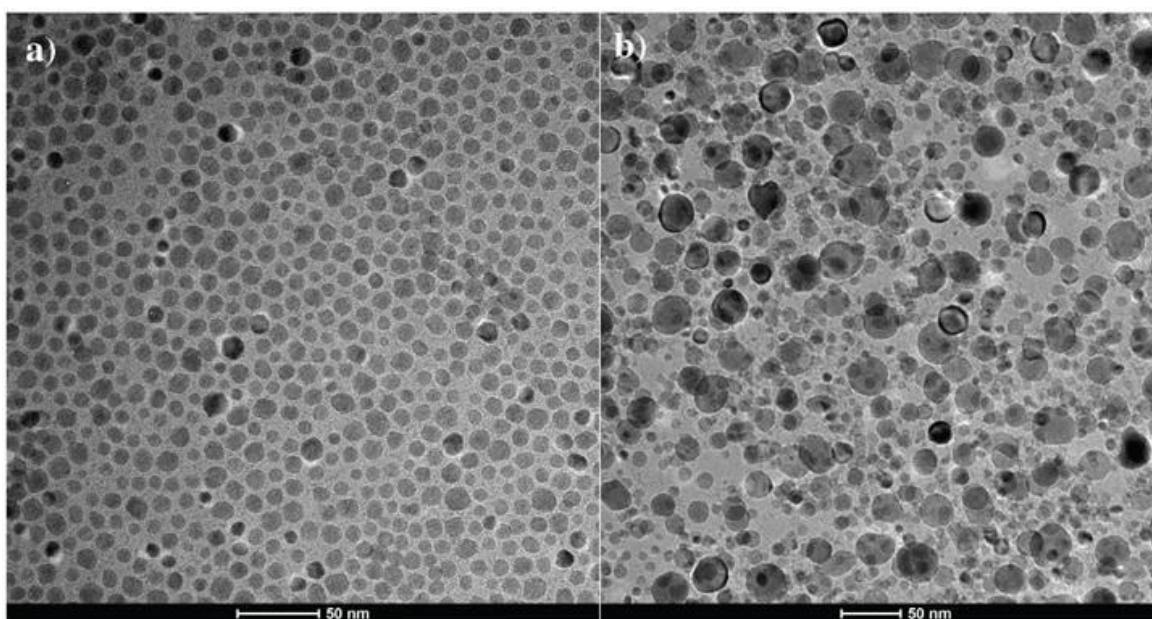
Figure 4.65 - Low magnification HRTEM images of *in situ* experiment of Sn doped γ-Fe$_2$O$_3$, a) before and b) after heating at 750°C [79].
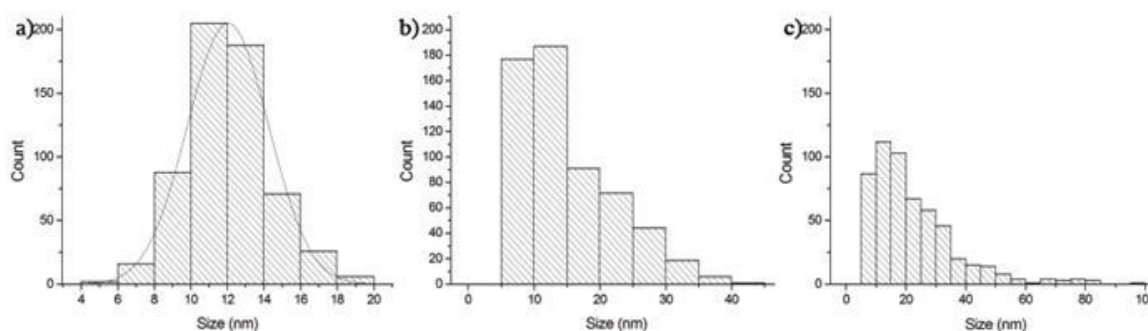
Figure 4.66 - Particle size distribution of: a) γ-Fe$_2$O$_3$ before, b) Sn doped γ-Fe$_2$O$_3$ after, and c) γ-Fe$_2$O$_3$ undoped after in situ heating experiments at 750°C [79].

Figure 4.67 shows a sequence of HRTEM images for undoped γ-Fe$_2$O$_3$ acquired during an *in situ* test at 650°C. The white arrow indicates the initial state of an agglomeration of nanoparticles which formed a ≈20 nm diameter particle during *in situ* test at high temperature. The red arrow indicates a nanoparticle that was not in contact with any other particle at the begging of the test, and that did not grow during the experiment. Just like this particle, many other "solitary particles" did not grow either. As the agglomerated nanoparticles grow, they come into contact with other particles, promoting a further growth.

Figure 4.68 shows a sequence of HRTEM images for Sn doped γ-Fe$_2$O$_3$ acquired during an *in situ* test at 750°C.   The white arrow indicates an agglomeration of nanoparticles which sintered during the experiment. Even in higher temperatures and longer times, it can be observed that the Sn doped γ-Fe$_2$O$_3$ manage to preserve their morphology and that the growth rate is slower.   Unfortunately, due to the difference in initial concentrations between the two experiments, it is difficult to assure a definitive conclusion about the final size distribution of the nanoparticles.
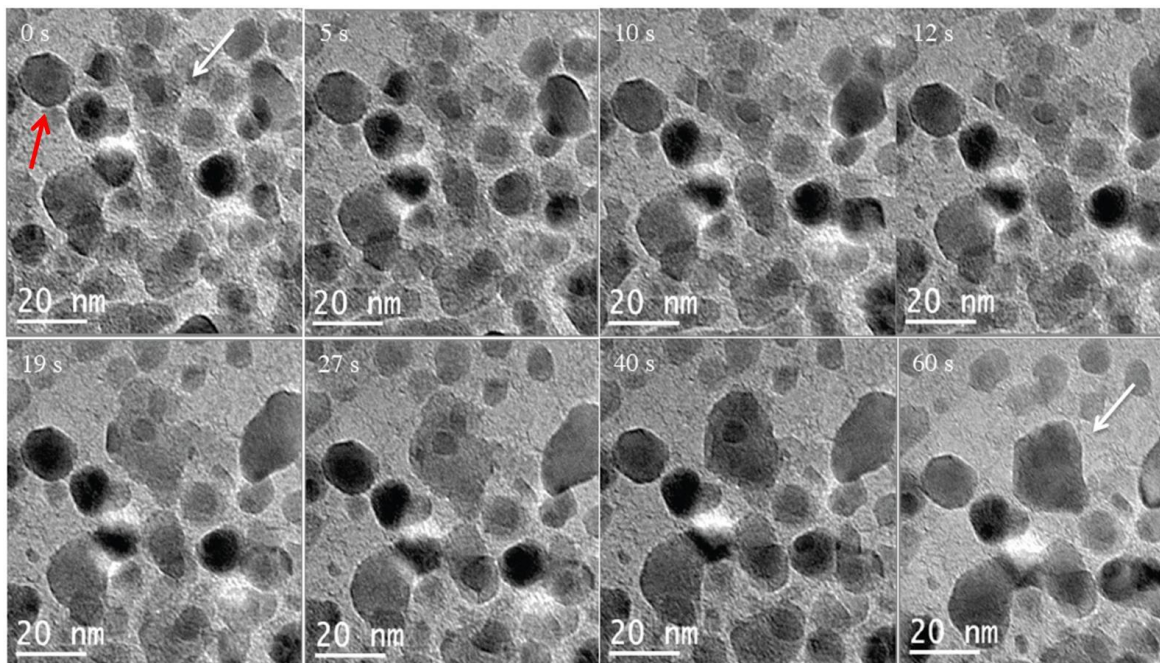
Figure 4.67 - Sequence of HRTEM images for undoped γ-Fe$_2$O$_3$ treated at 650°C. Adapted from [79].
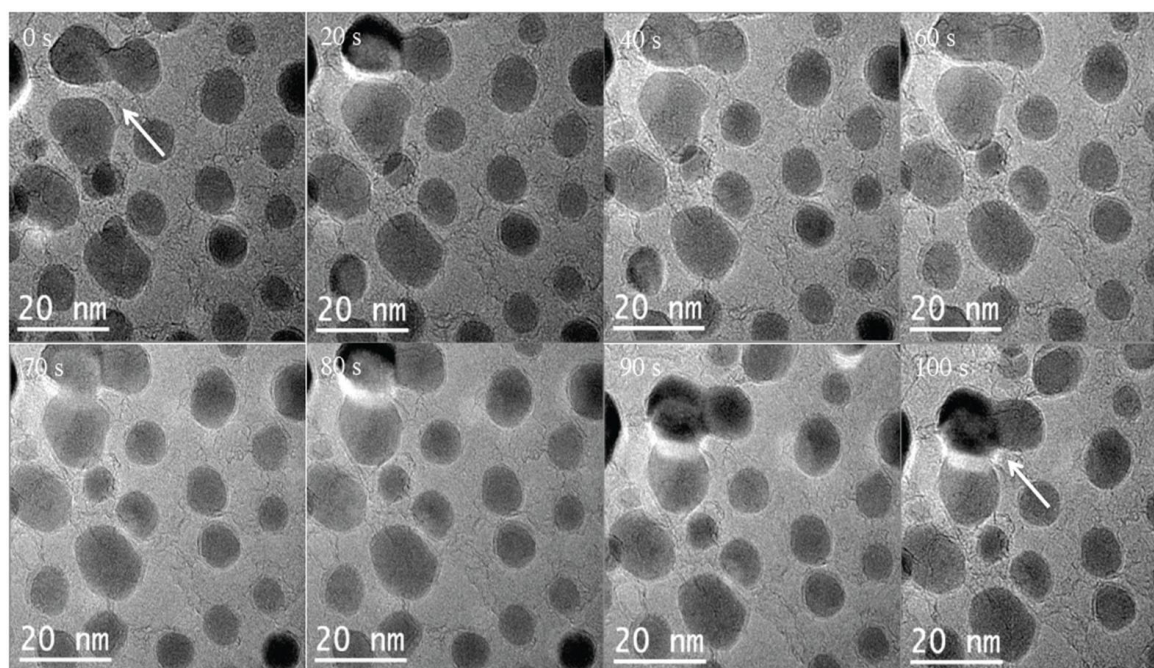
Figure 4.68 - Sequence of HRTEM images for Sn doped γ-Fe₂O₃ treated at 750°C. Adapted from [79].

An interesting fact is that, although the particles are iron oxides, they have enough degrees of freedom to move and rotate; which allows them to sinter (unlike our particles of cerium and zirconium oxide). This may be due to the difference in size (volume) of the particles. The cerium and zirconium oxide nanoparticles have a volume of $\approx$10 and 39 nm^3, respectively; while the iron oxide nanoparticles have a volume of $\approx$900 nm^3. This means that the iron nanoparticles are between 20 and 90 times larger than the others. Having a larger size means that a smaller percentage of the surface atoms will be bound with the substrate; and that there is a greater amount of atoms in each particle exerting attractive forces (Coulomb interactions).

As an exercise, let's compare our CeO$_2$ nanoparticle with 2.7 nm mean size with a hypothetical CeO$_2$ nanoparticle with mean diameter of 12 nm (Figure 4.69). To simulate the particles the software Vesta 3 was used [76], the crystal structure was fluorite without any defect and Oxygen atoms surround the particles, following the crystalline structure. The total amount of atoms in the particle with 2.7 nm is 1029, while in the particle with 12 nm there are 88499. The number of oxygen atoms on the surface was estimated at 288 and 5696 for

the particles of 2.7 and 12 mm, respectively. For the proposed morphologies, the crystallographic faces with the higher amount of atoms correspond to the {100} planes; being 40 and 396 oxygen atoms for the particles with 2.7 and 12 nm respectively
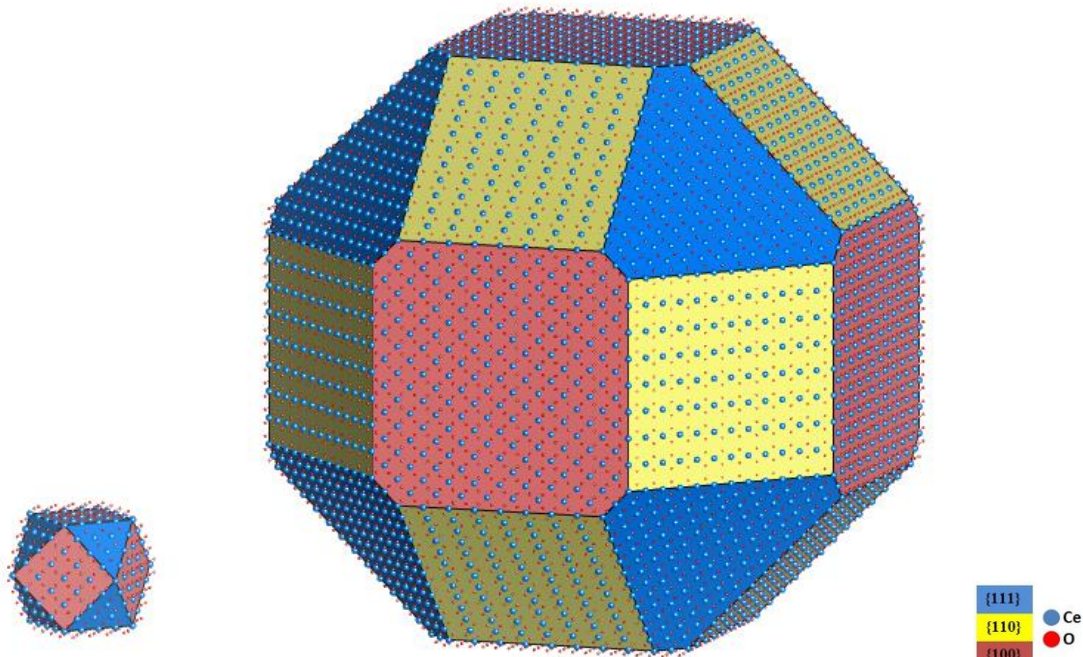
Figure 4.69 - 3D simulation of ceria nanoparticles, comparing two nanoparticles with a mean size 2.7 nm and 12 nm.

Assuming that the all oxygen atoms in the (100) plane, and the surface oxygen atoms (surrounding) of the two subsequent crystal planes are bound with the substrate; we would have a total of 84 and 552 for the particles with 2.7 and 12 nm, respectively. This would mean that, in the 2.7 nm particle, ≈8.2% of the atoms of the whole particle would be bound with the substrate; while in the 12 nm particle only ≈0.6% of its atoms would be bound.

$$(2.7nm) \rightarrow \frac{84 \, _{O \, atoms}}{1029 \, _{total \, atoms}} = 8.2\%$$

$$(12nm) \rightarrow \frac{552 \, _{O \, atoms}}{88499 \, _{total \, atoms}} = 0.6\%$$

For a particle of 2.7 nm, where approximately 50% of its atoms are on its surface, having ≈8% of its atoms bonded is something significant.

Obviously, these calculations are a simple approximation, since we cannot estimate, accurately, how many oxygen atoms are on the surface of the particles, nor how many of them are effectively bound to the substrate. Even so, it serves as an example to have a notion of how much of a nanoparticle can actually interact with the substrate. Also, it is worth mentioning that due to the roughness of the film, it is more likely to have fewer bonds between the faces of the 12 nm nanoparticle and the substrate; which further increases the gap with the 2.7 nm nanoparticle.

5 CONCLUSIONS

- Three different types of nanoparticles were synthesized using the solvothermal method for zirconium oxide and tin oxide, and hydrothermal and solvent-controlled method for cerium oxide. All nanoparticles can be dispersed in organic non-polar solvents such as toluene, and can be easily mixed for the realization of *in situ* and *ex situ* tests.

- A novel synthesis was developed, via the solvent-controlled method, ceria nanoparticles with a narrow size distribution, high reproducibility (above 80%), and a mean size below the common values found in the literature (2.7 ± 0.3 nm) was obtained.

- The effect of the electron beam current density on the samples during *in situ* experiments was investigated. We can conclude that there is a synergy between the temperature and the electron dose that promote the interaction between the nanoparticles.

- The material of the TEM grid (and his film) showed a great influence during the *in situ* tests, since the samples can interact with the atoms of the film of the TEM grid interfering with the "normal behavior" of the sample during the experiments.

- Several *in situ* tests were performed using ZrO_2 nanoparticles, and mixed nanoparticles of CeO_2 and ZrO_2. We can conclude that the *in situ* experiments at high temperature are a powerful tool to follow the behavior of nanoparticles during sintering. Further experiments at higher temperatures, using TEM grids that withstand those temperatures, can give more interesting results.

- In our experiments, the main mechanism of interaction between nanoparticles was oriented attachment, even in the mixed oxides the particles only interact with those of the same species.

- When the nanoparticles are in contact at the beginning of the tests, densification processes can be observed. On the other hand, the interactions between the oxide nanoparticles and the surface of the films avoid the movement and the sintering of the particles. To promote movement of the nanoparticles, a larger initial particle size is recommended.

- Following the methodology described in this work, other types of *in situ* experiments can be developed, using other particles, or mixtures of particles.

6 SUGGESTIONS FOR FUTURE WORKS

- Further researches over the solvent-controlled synthesis of cerium oxide developed in this work could lead to a better understanding of the growth mechanisms these nanoparticles. Also, this new synthesis route needs more research to obtain nanoparticles of larger sizes. In a parallel work, longer holding times at high temperature were used (up to 5 hours); no significant changes were observed.

- For future *in situ* experiments, the use of other TEM metal grids, like nickel (Ni), or molybdenum (Mo) which have a better performance at high temperatures, is recommended.

- Due to the turbulent flow produced by the water circulator system, and the electronic noise signals introduced by the SmartSet Hot Stage temperature controlled of the Gatan 628 single tilt heating holder. The use of other *in situ* holder, with MEMS, that allows the acquisition of high resolution images at high temperatures is recommended.

- Every day more and more technological advances in electron microscopy are developed. Nowadays, new sample holders for *in situ* transmission electron microscopy are available in the market. For example, the Poseidon™ liquid holder from Protochips allows the use of liquids and also heating (from room temperature to 100°C). Unfortunately, the access to this sample holders is restricted (high cost), and the temperatures are not so high (yet). Even so, the use of this type of sample holder is recommended.

- The use of larger nanoparticles (> 10-20 nm) is recommended. When a liquid cell for the *in situ* tests is not available, the use of larger oxide nanoparticles assists the movement, promoting their interaction.

- For future works, the measuring and control of the electron dose-rate is highly recommended. Since controlling the electron beam current density

(EBCD) allow us to guarantee that the phenomena observed during the experiments are due to the experimental setup, and are not influenced by beam damage.

7 BIBLIOGRAPHY

[1] D.B. Williams, C.B. Carter, Transmission Electron Microscopy: A textbook for Materials Science, Springer US, Boston, MA, 2009.

[2] P.L. Gai, ed., In-Situ Microscopy in Materials Research, Springer US, Boston, MA, 1997.

[3] F. Banhart, In-situ Electron Microscopy at High Resolution, World Scientific, 2008.

[4] D.-M. Tang, In Situ Transmission Electron Microscopy Studies of Carbon Nanotube Nucleation Mechanism and Carbon Nanotube-Clamped Metal Atomic Chains, Doctoral Thesis, Institute of Metal Research, Chinese Academy of Sciences, 2013.

[5] Reality check on reproducibility, Nature News. 533 (2016) 437. doi:10.1038/533437a.

[6] Global Rare Earth Elements Market Analysis And Segment Forecasts To 2020, (n.d.). http://www.grandviewresearch.com/industry-analysis/rare-earth-elements-market (accessed March 28, 2014).

[7] M. Humphries, Rare Earth Elements: The Global Supply Chain, (2013). http://www.fas.org/sgp/crs/natsec/R41347.pdf.

[8] Brazil needs technology and capability to explore rare-earth elements — English, (n.d.). http://www12.senado.gov.br/internacional/en/2013/brazil-needs-technology-and-capability-to-explore-rare-earth-elements (accessed April 10, 2014).

[9] A. Russell, K.L. Lee, Structure-Property Relations in Nonferrous Metals, John Wiley & Sons, Hoboken, NJ, 2005.

[10] Y. Chen, T. Liu, C. Chen, W. Guo, R. Sun, S. Lv, M. Saito, S. Tsukimoto, Z. Wang, Synthesis and characterization of CeO_2 nano-rods, Ceramics International. 39 (2013) 6607–6610. doi:10.1016/j.ceramint.2013.01.096.

[11] B.C.H. Steele, A. Heinzel, Materials for fuel-cell technologies, Nature. 414 (2001) 345–352. doi:10.1038/35104620.

[12]P. Jasinski, T. Suzuki, H.U. Anderson, Nanocrystalline undoped ceria oxygen sensor, Sensors and Actuators B: Chemical. 95 (2003) 73–77. doi:10.1016/S0925-4005(03)00407-6.

[13]A. Trovarelli, Catalytic Properties of Ceria and CeO2-Containing Materials, Catalysis Reviews. 38 (1996) 439–520. doi:10.1080/01614949608006464.

[14]G. Azimi, R. Dhiman, H.-M. Kwon, A.T. Paxson, K.K. Varanasi, Hydrophobicity of rare-earth oxide ceramics, Nat Mater. 12 (2013) 315–320. doi:10.1038/nmat3545.

[15]N.J. Lawrence, Synthesis and Catalytic Activity of Nanostructured Cerium Oxide, Master's Thesis, University of Nebraska, 2010.

[16]X. GAO, C. CHEN, S. REN, J. ZHANG, D. SU, Structural Effects of Cerium Oxides on Their Thermal Stability and Catalytic Performance in Propane Oxidation Dehydrogenation, Chinese Journal of Catalysis. 33 (2012) 1069–1074. doi:10.1016/S1872-2067(11)60404-X.

[17]S.S. Lee, H. Zhu, E.Q. Contreras, A. Prakash, H.L. Puppala, V.L. Colvin, High Temperature Decomposition of Cerium Precursors To Form Ceria Nanocrystal Libraries for Biological Applications, Chemistry of Materials. 24 (2012) 424–432. doi:10.1021/cm200863q.

[18]S. Deshpande, S. Patil, S.V. Kuchibhatla, S. Seal, Size dependency variation in lattice parameter and valency states in nanocrystalline cerium oxide, Applied Physics Letters. 87 (2005) 133113. doi:10.1063/1.2061873.

[19]C. Korsvik, S. Patil, S. Seal, W.T. Self, Superoxide dismutase mimetic properties exhibited by vacancy engineered ceria nanoparticles, Chem. Commun. (2007) 1056–1058. doi:10.1039/B615134E.

[20]I.A. Kartsonakis, P. Liatsi, I. Daniilidis, G. Kordas, Synthesis, Characterization, and Antibacterial Action of Hollow Ceria Nanospheres with/without a Conductive Polymer Coating, Journal of the American Ceramic Society. 91 (2008) 372–378. doi:10.1111/j.1551-2916.2007.02088.x.

[21]A. Karakoti, S. Singh, J.M. Dowding, S. Seal, W.T. Self, Redox-active radical scavenging nanomaterials, Chem. Soc. Rev. 39 (2010) 4422–4432. doi:10.1039/B919677N.

[22] K. Bhargava, A. Arya, A. Gangwar, S. Singh, M. Roy, M. Das, N. Sethy, Cerium oxide nanoparticles promote neurogenesis and abrogate hypoxia-induced memory impairment through AMPK-PKC-CBP signaling cascade, International Journal of Nanomedicine. (2016) 1159. doi:10.2147/IJN.S102096.

[23] G.-M. Lyu, Y.-J. Wang, X. Huang, H.-Y. Zhang, L.-D. Sun, Y.-J. Liu, C.-H. Yan, Hydrophilic CeO2 nanocubes protect pancreatic β-cell line INS-1 from H2O2-induced oxidative stress, Nanoscale. 8 (2016) 7923–7932. doi:10.1039/C6NR00826G.

[24] W.J. Stark, Nanoparticles in Biological Systems, Angew. Chem. Int. Ed. 50 (2011) 1242–1258. doi:10.1002/anie.200906684.

[25] C.K. Kim, T. Kim, I.-Y. Choi, M. Soh, D. Kim, Y.-J. Kim, H. Jang, H.-S. Yang, J.Y. Kim, H.-K. Park, S.P. Park, S. Park, T. Yu, B.-W. Yoon, S.-H. Lee, T. Hyeon, Ceria Nanoparticles that can Protect against Ischemic Stroke, Angew. Chem. Int. Ed. 51 (2012) 11039–11043. doi:10.1002/anie.201203780.

[26] O.A. Graeve, Zirconia, in: J.F. Shackelford, R.H. Doremus (Eds.), Ceramic and Glass Materials, Springer US, Boston, MA, 2008: pp. 169–197.

[27] M. G., Catalysis by Transition Metal Modified Ceria and Ceria-Zirconia Mixed Oxides Prepared via Sol-Gel Route, Doctoral Thesis, Cochin University of Science and Technology, 2006.

[28] G.R. Rao, J. Kašpar, S. Meriani, R. Monte, M. Graziani, NO decomposition over partially reduced metallized CeO2-ZrO2 solid solutions, Catalysis Letters. 24 (1994) 107–112. doi:10.1007/BF00807380.

[29] J. Kašpar, P. Fornasiero, M. Graziani, Use of CeO2-based oxides in the three-way catalysis, Catalysis Today. 50 (1999) 285–298. doi:10.1016/S0920-5861(98)00510-0.

[30] M. Ozawa, Role of cerium–zirconium mixed oxides as catalysts for car pollution: A short review, Journal of Alloys and Compounds. 275–277 (1998) 886–890. doi:10.1016/S0925-8388(98)00477-0.

[31] G. Dutta, U.V. Waghmare, T. Baidya, M.S. Hegde, K.R. Priolkar, P.R. Sarode, Reducibility of Ce1-xZrxO2: Origin of Enhanced Oxygen Storage Capacity, Catalysis Letters. 108 (2006) 165–172. doi:10.1007/s10562-006-0040-z.

[32] E. Mamontov, T. Egami, R. Brezny, M. Koranne, S. Tyagi, Lattice Defects and Oxygen Storage Capacity of Nanocrystalline Ceria and Ceria-Zirconia, The Journal of Physical Chemistry B. 104 (2000) 11110–11116. doi:10.1021/jp0023011.

[33] M.K. Devaraju, X. Liu, K. Yusuke, S. Yin, T. Sato, Solvothermal synthesis and characterization of ceria–zirconia mixed oxides for catalytic applications, Nanotechnology. 20 (2009) 405606. doi:10.1088/0957-4484/20/40/405606.

[34] R.D. Monte, J. Kašpar, On the Role of Oxygen Storage in Three-Way Catalysis, Topics in Catalysis. 28 (2004) 47–57. doi:10.1023/B:TOCA.0000024333.08447.f7.

[35] A. Wongkaew, Effect of Cerium Oxide and Zirconium Oxide to Activity of Catalysts, Chiang Mai J. Sci. 35 (2008) 156–162.

[36] T. Kim, J.M. Vohs, R.J. Gorte, Thermodynamic Investigation of the Redox Properties of Ceria−Zirconia Solid Solutions, Industrial & Engineering Chemistry Research. 45 (2006) 5561–5565. doi:10.1021/ie0511478.

[37] M.A. Carpenter, S. Mathur, A. Kolmakov, Metal Oxide Nanomaterials for Chemical Sensors, Springer, 2012.

[38] J.G. Lu, P. Chang, Z. Fan, Quasi-one-dimensional metal oxide materials—Synthesis, properties and applications, Materials Science and Engineering: R: Reports. 52 (2006) 49–91. doi:10.1016/j.mser.2006.04.002.

[39] P.G. Harrison, M.J. Willett, The mechanism of operation of tin(iv) oxide carbon monoxide sensors, Nature. 332 (1988) 337–339. doi:10.1038/332337a0.

[40] Y. Li, W. Yin, R. Deng, R. Chen, J. Chen, Q. Yan, B. Yao, H. Sun, S.-H. Wei, T. Wu, Realizing a SnO2-based ultraviolet light-emitting diode via breaking the dipole-forbidden rule, NPG Asia Mater. 4 (2012) e30. doi:10.1038/am.2012.56.

[41] X. Xu, R. Zhang, X. Zeng, X. Han, Y. Li, Y. Liu, X. Wang, Effects of La, Ce, and Y Oxides on SnO_2 Catalysts for CO and CH_4 Oxidation, ChemCatChem. 5 (2013) 2025–2036. doi:10.1002/cctc.201200760.

[42] A. Khodadadi, S.S. Mohajerzadeh, Y. Mortazavi, A.M. Miri, Cerium oxide/SnO2-based semiconductor gas sensors with improved sensitivity to CO,

Sensors and Actuators B: Chemical. 80 (2001) 267–271. doi:10.1016/S0925-4005(01)00915-7.

[43] J.L. Ayastuy, A. Iglesias-González, M.A. Gutiérrez-Ortiz, Synthesis and characterization of low amount tin-doped ceria (CeXSn1−XO2−δ) for catalytic CO oxidation, Chemical Engineering Journal. 244 (2014) 372–381. doi:10.1016/j.cej.2014.01.077.

[44] E. Tani, M. Yoshimura, S. Somiya, Revised Phase Diagram of the System ZrO2-CeO2 Below 1400oC, Journal of the American Ceramic Society. 66 (1983) 506–510. doi:10.1111/j.1151-2916.1983.tb10591.x.

[45] P. Duran, M. Gonzalez, C. Moure, J.R. Jurado, C. Pascual, A new tentative phase equilibrium diagram for the ZrO2-CeO2 system in air, Journal of Materials Science. 25 (1990) 5001–5006. doi:10.1007/BF00580121.

[46] L.M. Lopato, E.R. Andrievskaya, Reaction of Cerium Oxide with Zirconium and Yttrium Oxides at 1250°C, Powder Metallurgy and Metal Ceramics. 41 (2002) 63–71. doi:10.1023/A:1016064615748.

[47] A.S. Deshpande, N. Pinna, P. Beato, M. Antonietti, M. Niederberger, Synthesis and Characterization of Stable and Crystalline Ce1-xZrxO2 Nanoparticle Sols, Chem. Mater. 16 (2004) 2599–2604. doi:10.1021/cm040155w.

[48] R.A. Swalin, Thermodynamics of Solids, 2nd ed., Wiley-Interscience, 1972. https://www.abebooks.com/9780471838548/Thermodynamics-Solids-2nd-Ed-Richard-0471838543/plp (accessed October 2, 2018).

[49] T.G. Rochow, P.A. Tucker, Introduction to Microscopy by Means of Light, Electrons, X Rays, or Acoustics, 2nd ed., Springer US, 1994. //www.springer.com/gp/book/9780306446849 (accessed August 18, 2018).

[50] N. Jiang, J.C.H. Spence, On the dose-rate threshold of beam damage in TEM, Ultramicroscopy. 113 (2012) 77–82. doi:10.1016/j.ultramic.2011.11.016.

[51] H. Ehrlich, M. Motylenko, P.V. Sundareshwar, A. Ereskovsky, I. Zgłobicka, T. Noga, T. Płociński, M.V. Tsurkan, E. Wyroba, S. Suski, H. Bilski, M. Wysokowski, H. Stöcker, A. Makarova, D. Vyalikh, J. Walter, S.L. Molodtsov, V.V. Bazhenov, I. Petrenko, E. Langer, A. Richter, E. Niederschlag, M. Pisarek, A. Springer, M. Gelinsky, D. Rafaja, A. Witkowski, D.C. Meyer, T. Jesionowski,

132

K.J. Kurzydłowski, Multiphase Biomineralization: Enigmatic Invasive Siliceous Diatoms Produce Crystalline Calcite, Advanced Functional Materials. 26 (2016) 2503–2510. doi:10.1002/adfm.201504891.

[52] D. Mohanty, A.S. Sefat, S. Kalnaus, J. Li, R.A. Meisner, E.A. Payzant, D.P. Abraham, D.L. Wood, C. Daniel, Investigating phase transformation in the Li1.2Co0.1Mn0.55Ni0.15O2 lithium-ion battery cathode during high-voltage hold (4.5 V) via magnetic, X-ray diffraction and electron microscopy studies, J. Mater. Chem. A. 1 (2013) 6249–6261. doi:10.1039/C3TA10304H.

[53] M. Niederberger, N. Pinna, Metal Oxide Nanoparticles in Organic Solvents, Springer London, London, 2009. http://link.springer.com/10.1007/978-1-84882-671-7 (accessed December 13, 2016).

[54] B.L. Cushing, V.L. Kolesnichenko, C.J. O'Connor, Recent Advances in the Liquid-Phase Syntheses of Inorganic Nanoparticles, Chem. Rev. 104 (2004) 3893–3946. doi:10.1021/cr030027b.

[55] K. Byrappa, M. Yoshimura, Handbook of Hydrothermal Technology, Cambridge University Press, 2008.

[56] K. Byrappa, T. Adschiri, Hydrothermal technology for nanotechnology, Progress in Crystal Growth and Characterization of Materials. 53 (2007) 117–166. doi:10.1016/j.pcrysgrow.2007.04.001.

[57] G.H. Lee, J.-M. Zuo, Growth and Phase Transformation of Nanometer-Sized Titanium Oxide Powders Produced by the Precipitation Method, Journal of the American Ceramic Society. 87 (2004) 473–479. doi:10.1111/j.1551-2916.2004.00473.x.

[58] D. Li, M.H. Nielsen, J.R.I. Lee, C. Frandsen, J.F. Banfield, J.J.D. Yoreo, Direction-Specific Interactions Control Crystal Growth by Oriented Attachment, Science. 336 (2012) 1014–1018. doi:10.1126/science.1219643.

[59] C. Zhu, S. Liang, E. Song, Y. Zhou, W. Wang, F. Shan, Y. Shi, C. Hao, K. Yin, T. Zhang, J. Liu, H. Zheng, L. Sun, In-situ liquid cell transmission electron microscopy investigation on oriented attachment of gold nanoparticles, Nature Communications. 9 (2018) 421. doi:10.1038/s41467-018-02925-6.

[60] H.-X. Mai, L.-D. Sun, Y.-W. Zhang, R. Si, W. Feng, H.-P. Zhang, H.-C. Liu, C.-H. Yan, Shape-Selective Synthesis and Oxygen Storage Behavior of

Ceria Nanopolyhedra, Nanorods, and Nanocubes, J. Phys. Chem. B. 109 (2005) 24380–24385. doi:10.1021/jp055584b.

[61] S. Yang, L. Gao, Controlled Synthesis and Self-Assembly of CeO2 Nanocubes, J. Am. Chem. Soc. 128 (2006) 9330–9331. doi:10.1021/ja063359h.

[62] N. Du, H. Zhang, B. Chen, X. Ma, D. Yang, Ligand-free Self-Assembly of Ceria Nanocrystals into Nanorods by Oriented Attachment at Low Temperature, J. Phys. Chem. C. 111 (2007) 12677–12680. doi:10.1021/jp074011r.

[63] H. Zhang, J.F. Banfield, Energy Calculations Predict Nanoparticle Attachment Orientations and Asymmetric Crystal Formation, J. Phys. Chem. Lett. 3 (2012) 2882–2886. doi:10.1021/jz301161j.

[64] V. Sharma, P.A. Crozier, R. Sharma, J.B. Adams, Direct observation of hydrogen spillover in Ni-loaded Pr-doped ceria, Catalysis Today. 180 (2012) 2–8. doi:10.1016/j.cattod.2011.09.009.

[65] J.A. Pérez-Omil, S. Bernal, J.J. Calvino, J.C. Hernández, C. Mira, M.P. Rodríguez-Luque, R. Erni, N.D. Browning, Combined HREM and HAADF Scanning Transmission Electron Microscopy: A Powerful Tool for Investigating Structural Changes in Thermally Aged Ceria−Zirconia Mixed Oxides, Chemistry of Materials. 17 (2005) 4282–4285. doi:10.1021/cm050976g.

[66] P.A. Crozier, R. Wang, R. Sharma, In situ environmental TEM studies of dynamic changes in cerium-based oxides nanoparticles during redox processes, Ultramicroscopy. 108 (2008) 1432–1440. doi:10.1016/j.ultramic.2008.05.015.

[67] S. Huang, L. Li, J. Vleugels, P. Wang, O. Van der Biest, Thermodynamic prediction of the nonstoichiometric phase $Zr_{1-z}Ce_zO_{2-x}$ in the ZrO_2–$CeO_{1.5}$–CeO_2 system, Journal of the European Ceramic Society. 23 (2003) 99–106. doi:10.1016/S0955-2219(02)00073-0.

[68] M.A.L. Cordeiro, P.A. Crozier, E.R. Leite, Anisotropic Nanocrystal Dissolution Observation by in Situ Transmission Electron Microscopy, Nano Lett. 12 (2012) 5708–5713. doi:10.1021/nl3029398.

[69] K. Zhou, X. Wang, X. Sun, Q. Peng, Y. Li, Enhanced catalytic activity of ceria nanorods from well-defined reactive crystal planes, Journal of Catalysis. 229 (2005) 206–212. doi:10.1016/j.jcat.2004.11.004.

[70] M.A.L. Cordeiro, W. Weng, D.G. Stroppa, C.J. Kiely, E.R. Leite, High Resolution Electron Microscopy Study of Nanocubes and Polyhedral Nanocrystals of Cerium(IV) Oxide, Chem. Mater. 25 (2013) 2028–2034. doi:10.1021/cm304029s.

[71] D.G. Stroppa, L.A. Montoro, A. Beltrán, T.G. Conti, R.O. da Silva, J. Andrés, E.R. Leite, A.J. Ramirez, Anomalous oriented attachment growth behavior on SnO2 nanocrystals, Chem. Commun. 47 (2011) 3117–3119. doi:10.1039/C0CC04570E.

[72] J. Ba, J. Polleux, M. Antonietti, M. Niederberger, Non-aqueous Synthesis of Tin Oxide Nanocrystals and Their Assembly into Ordered Porous Mesostructures, Advanced Materials. 17 (2005) 2509–2512. doi:10.1002/adma.200501018.

[73] M. Niederberger, G. Garnweitner, Organic Reaction Pathways in the Nonaqueous Synthesis of Metal Oxide Nanoparticles, Chem. Eur. J. 12 (2006) 7282–7302. doi:10.1002/chem.200600313.

[74] * Shuxue Zhou, ‡ Georg Garnweitner, § and Markus Niederberger, † Markus Antonietti*, Dispersion Behavior of Zirconia Nanocrystals and Their Surface Functionalization with Vinyl Group-Containing Ligands, (2007). doi:10.1021/la700837u.

[75] G. Garnweitner, L.M. Goldenberg, O.V. Sakhno, M. Antonietti, M. Niederberger, J. Stumpe, Large-Scale Synthesis of Organophilic Zirconia Nanoparticles and their Application in Organic–Inorganic Nanocomposites for Efficient Volume Holography, Small. 3 (2007) 1626–1632. doi:10.1002/smll.200700075.

[76] K. Momma, F. Izumi, VESTA 3 for three-dimensional visualization of crystal, volumetric and morphology data, Journal of Applied Crystallography. 44 (2011) 1272–1276. doi:10.1107/S0021889811038970.

[77] Z. Zhang, D. Su, Behaviour of TEM metal grids during in-situ heating experiments, Ultramicroscopy. 109 (2009) 766–774. doi:10.1016/j.ultramic.2009.01.015.

[78] L.F. Allard, W.C. Bigelow, M. Jose-Yacaman, D.P. Nackashi, J. Damiano, S.E. Mick, A new MEMS-based system for ultra-high-resolution

imaging at elevated temperatures, Microscopy Research and Technique. 72 (2009) 208–215. doi:10.1002/jemt.20673.

[79] R.H. Gonçalves, Deposição de Nanocristais Coloidais: da Síntese à Aplicação na Fotoeletroquímica da Oxidação da Água, Ph.D, Federal University of Sao Carlos, 2016. https://repositorio.ufscar.br/handle/ufscar/7988.

[80] T. Ristoiu, L. Ciontea, R.-C. Suciu, T. Petrisor Jr., M.. Gabor, G. Thalmayer, T. Petrisor, Thermal decomposition study by DTA-TG-MS of cerium[III] acetylacetonate used as ceria thin film precursor, JOAM. 10 (2018) 2223–2227.

[81] S. Mourdikoudis, L.M. Liz-Marzán, Oleylamine in Nanoparticle Synthesis, Chemistry of Materials. 25 (2013) 1465–1476. doi:10.1021/cm4000476.

[82] J. Barthel, Dr. Probe: A software for high-resolution STEM image simulation, Ultramicroscopy. 193 (2018) 1–11. doi:10.1016/j.ultramic.2018.06.003.

[83] Robert F. Klie, Weronika Walkosz, G. Yang, Y. Zhao, Variable Temperature Electron Energy-Loss Spectroscopy, in: Scanning Transmission Electron Microscopy: Imaging and Analysis, Springer-Verlag, New York, 2011.

[84] D. Li, C. Wang, D. Tripkovic, S. Sun, N.M. Markovic, V.R. Stamenkovic, Surfactant Removal for Colloidal Nanoparticles from Solution Synthesis: The Effect on Catalytic Performance, ACS Catal. 2 (2012) 1358–1362. doi:10.1021/cs300219j.

[85] K.H. Stern, Oxidation of Silicon, Silicon Carbide, PN, Naval Research Laboratory, 1986.

[86] M. Jiang, N.O. Wood, R. Komanduri, On chemo-mechanical polishing (CMP) of silicon nitride (Si3N4) workmaterial with various abrasives, Wear. 220 (1998) 59–71. doi:10.1016/S0043-1648(98)00245-2.

[87] P. Bera, C. Anandan, XRD and XPS studies of room temperature spontaneous interfacial reaction of CeO2 thin films on Si and Si3N4 substrates, RSC Adv. 4 (2014) 62935–62939. doi:10.1039/C4RA09882J.

[88] M.A.L. Cordeiro, Estudo da Síntese de Nanocristais de CeO2 e de ZrO2 e Suas Sinterizações Por Microscopia Eletrônica de Transmissão in situ, Ph.D, Federal University of Sao Carlos, 2013.

136

APPENDIX A: SYNTHESIS OF TIN OXIDE NANOCRYSTALS

Similar to the zirconia, the tin oxide was synthesized by the solvothermal method. The SnO_2 nanocrystals were synthesized in a glovebox under a controlled atmosphere. A total of 0.75 mL of Tin (IV) chloride [$SnCl_4$] was stirred in a vessel with 15 mL of benzyl alcohol, after which the reaction vessel will be removed from the glovebox and heated at 110°C for about 24 h in a silicone bath. SnO_2 nanoparticles will be collected by centrifugation, washed and stored in THF [72]. Similar to the zirconia, the organic layer was modified to disperse the nanoparticles in organic non-polar solvents.
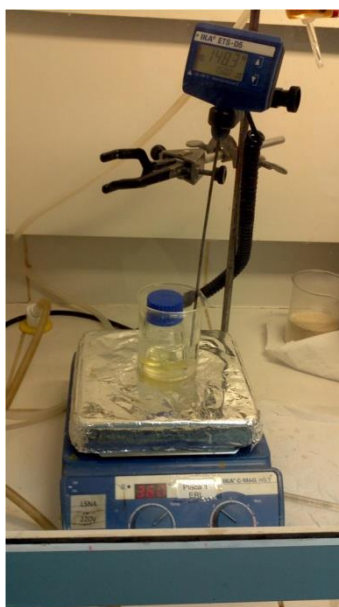
Figure A.1 - Assembly for synthesis of tin oxide nanoparticles.

The tin oxide nanoparticles were made based on previously reported synthesis from Niederberger *et al.* [72,73]. Figure A.2 shows the tin oxide nanoparticles dispersed in tetrahydrofuran. To disperse the particles in non-polar solvents, like toluene, an aliquot was dried under vacuum and toluene was added to the "powder", some drops of oleylamine was added, and after stirring, the particles begin to disperse. No significant change in the color of the dispersion was observed (due to the addition of the OAm).

Figure A.2 - Dispersion of tin oxide nanoparticles synthesized by the solvothermal method.

Figure A.3 shows a typical tetragonal structure of the tin oxide (JCPDS card no. 021-1250). Figure A.4 shows HRTEM images of the tin oxide nanoparticles, it can be observed that the particles are well dispersed, without agglomerates. The main difference between this synthesis, and the others syntheses of ceria and zirconia, is that the particle size distribution of the first two syntheses have a distribution that fit with a Gaussian distribution while the tin oxide best fit with a Log-normal distribution (Figure A.4c).
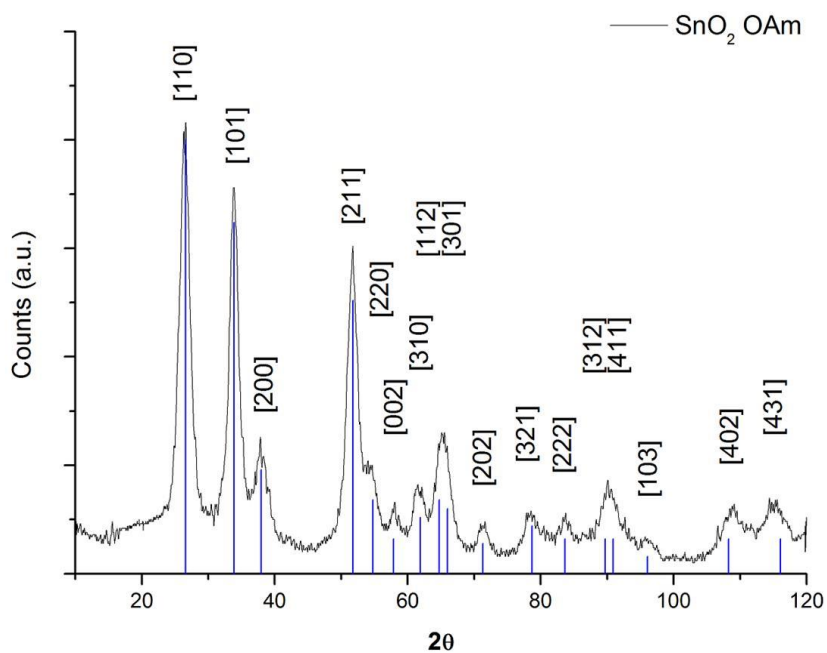
Figure A.3 - XRD of tin oxide nanoparticles synthesized by the solvothermal method.
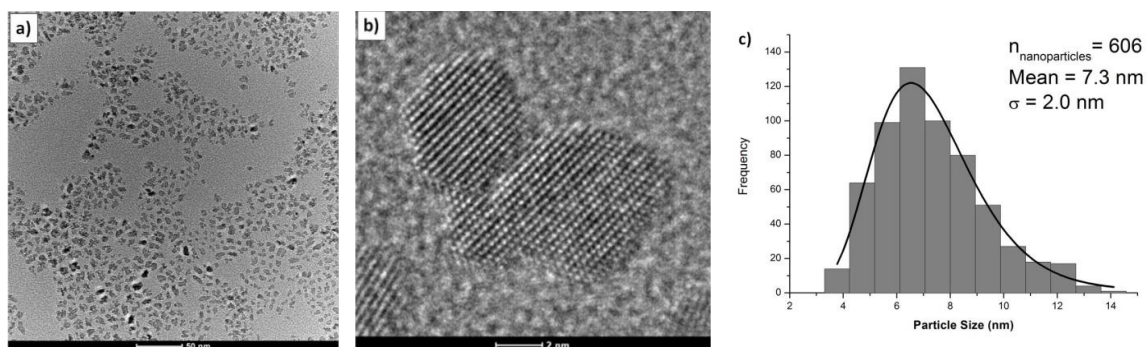
Figure A.4 - a) Low magnification HRTEM image of tin oxide nanoparticles, b) HRTEM image of isolated particles. c) Particle size distribution.

Figure A.5 shows the thermogravimetric analysis curve of the tin oxide nanoparticles synthesized with benzyl alcohol, dispersed in toluene with the addition of some drops of oleylamine. The first stage of mass loss in this sample occurs at lower temperatures compared with the particles synthesized with oleyl alcohol (or oleic acid). This is due to the low molecular weight of the benzyl alcohol (108.138 g/mol), compared to oleyl alcohol (268.478 g/mol). Increase the molecular weight increases the intermolecular forces, so it is more difficult to remove long chains from the surfaces of the particles. The final weight loss stabilizes around 62%, similar to zirconia, and ceria with 3 mmol of OAm.
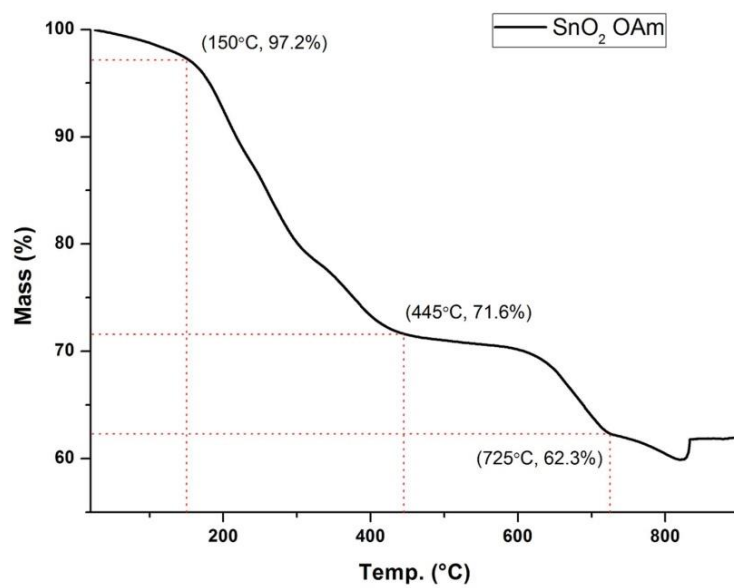
Figure A.5 - TGA of tin oxide nanoparticles synthesized by the solvothermal method.
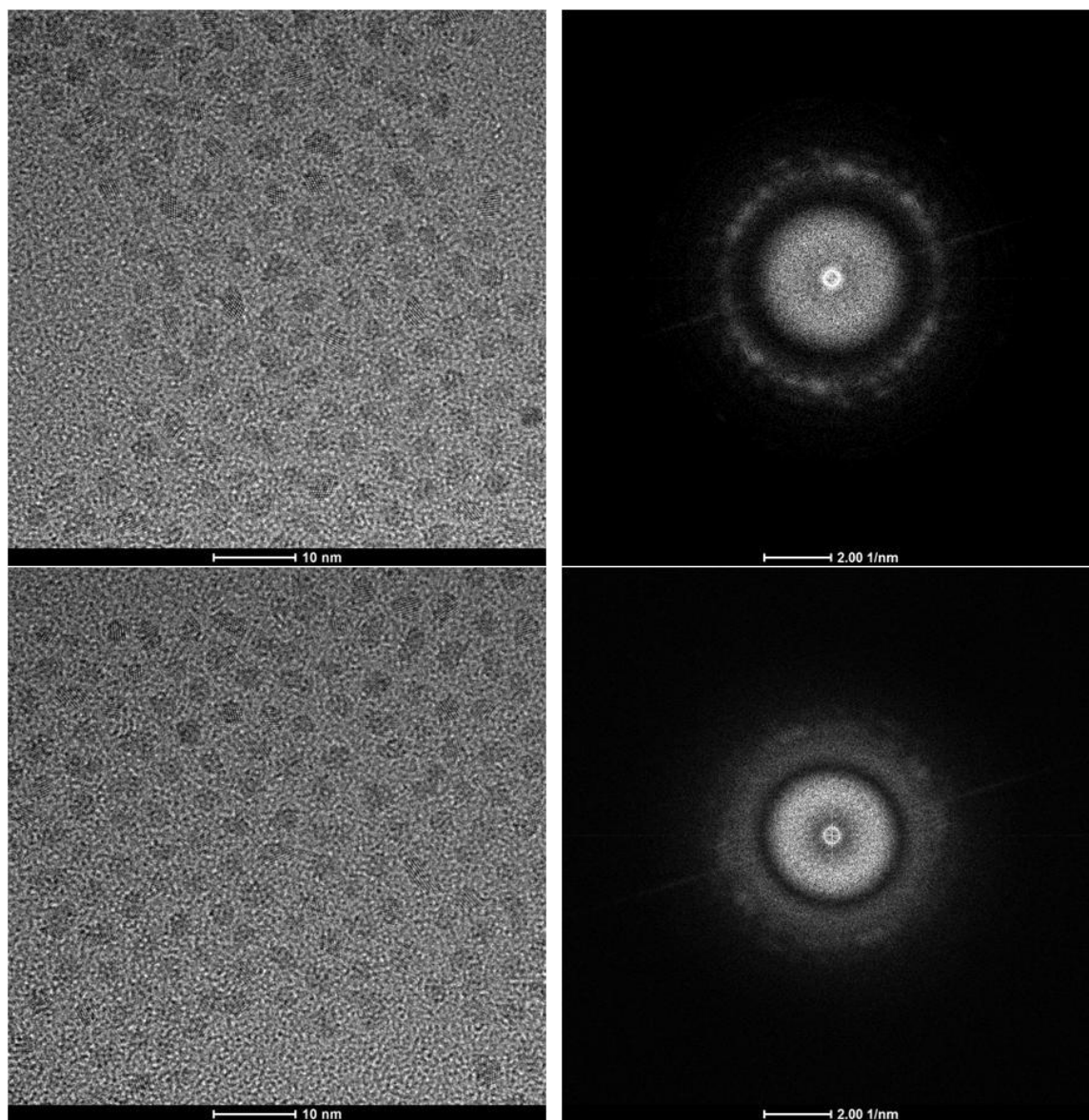
APPENDIX B: COMPLEMENTARY IMAGES

Figure B.1 - Low magnification HRTEM images and the corresponding FFT of ceria nanoparticles synthesized with, 0 mmol of OAm.
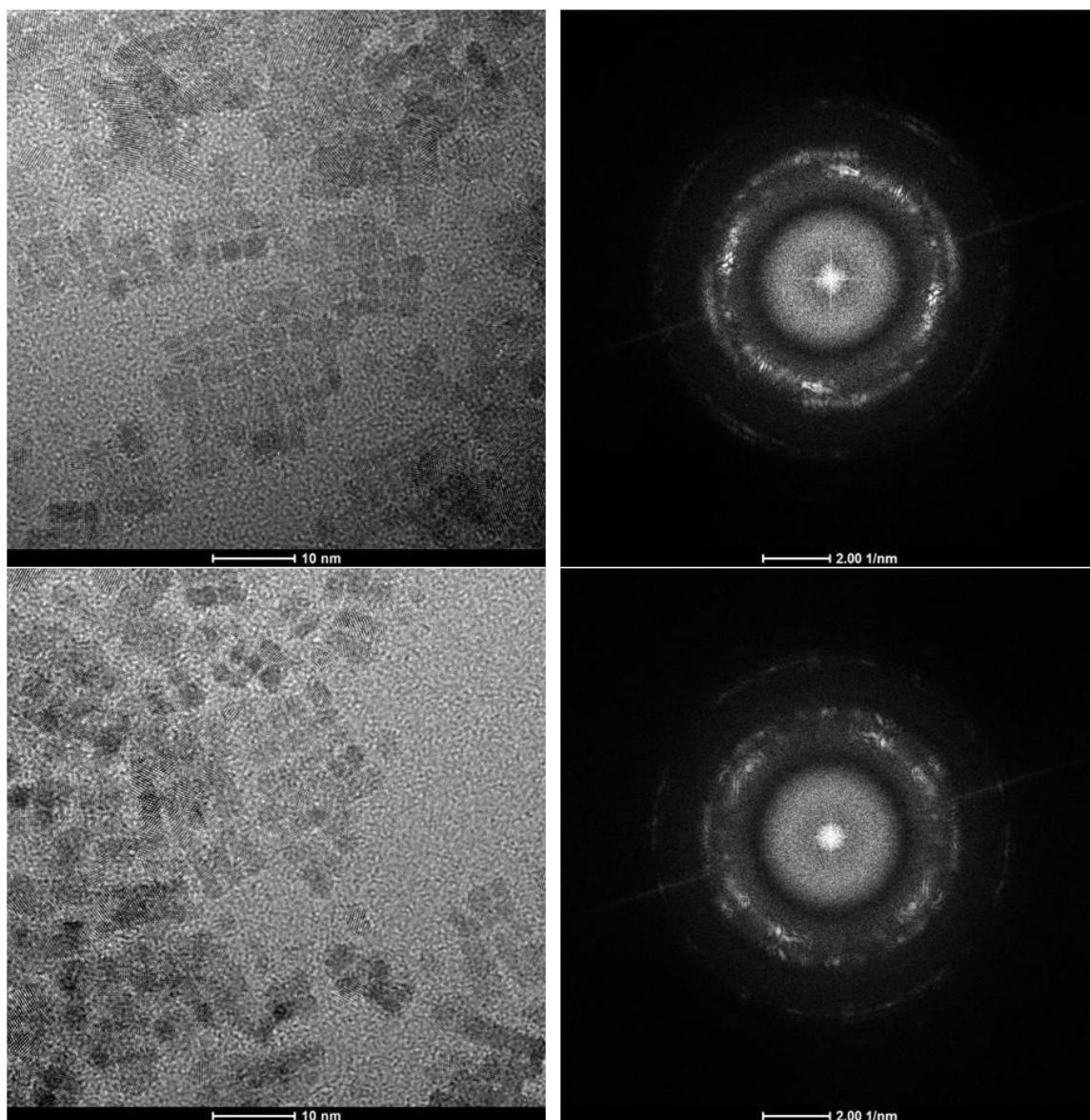
Figure B.2 - Low magnification HRTEM images and the corresponding FFT of ceria nanoparticles synthesized with, 3 mmol of OAm.
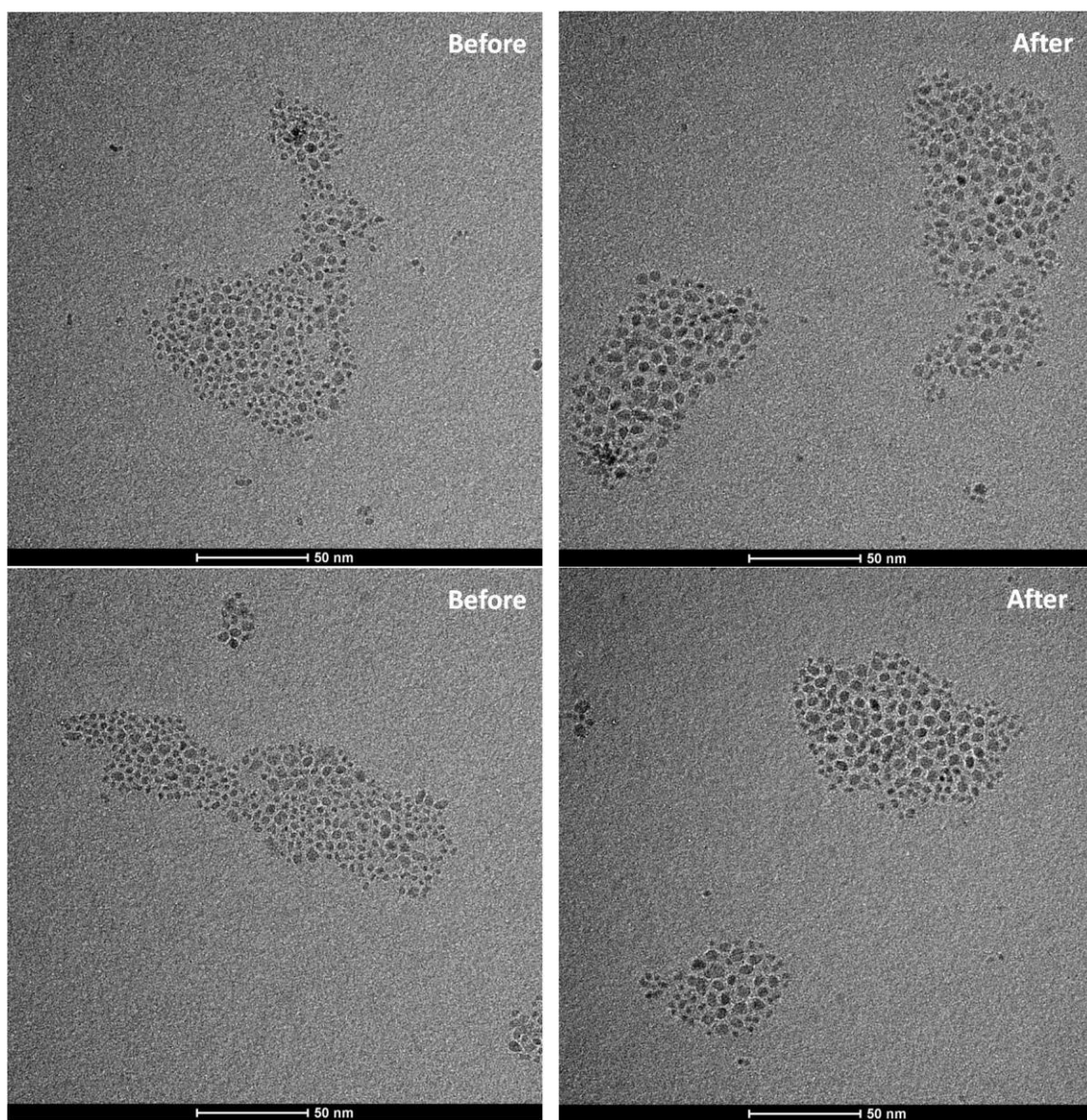
Figure B.3 - Low magnification HRTEM images before and after the *ex situ* test at 500°C for 30 minutes in mixed nanoparticles of CeO_2 and ZrO_2.
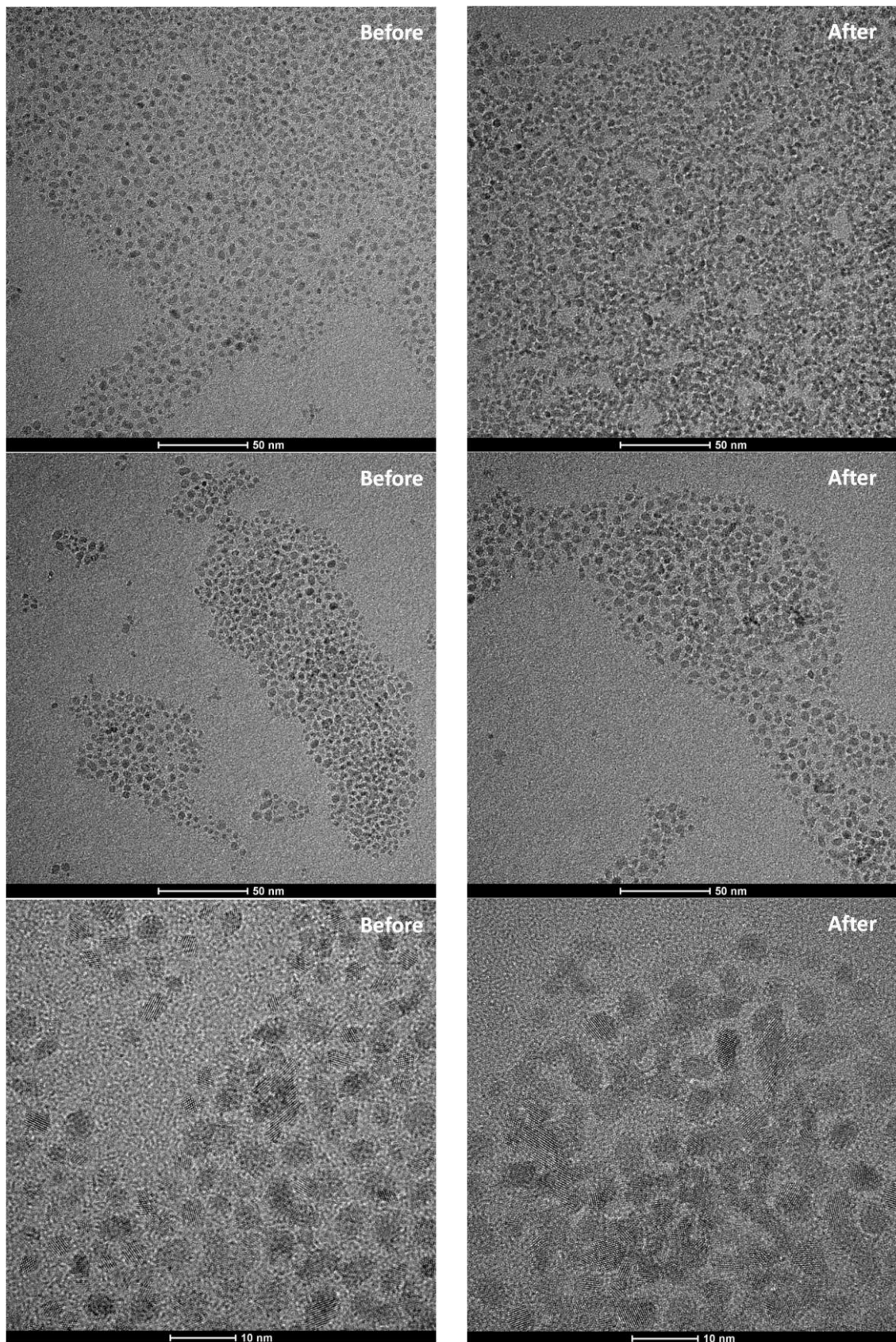
Figure B.4 - Low magnification HRTEM images before and after the *ex situ* test at 600°C for 30 minutes in mixed nanoparticles of CeO_2 and ZrO_2.
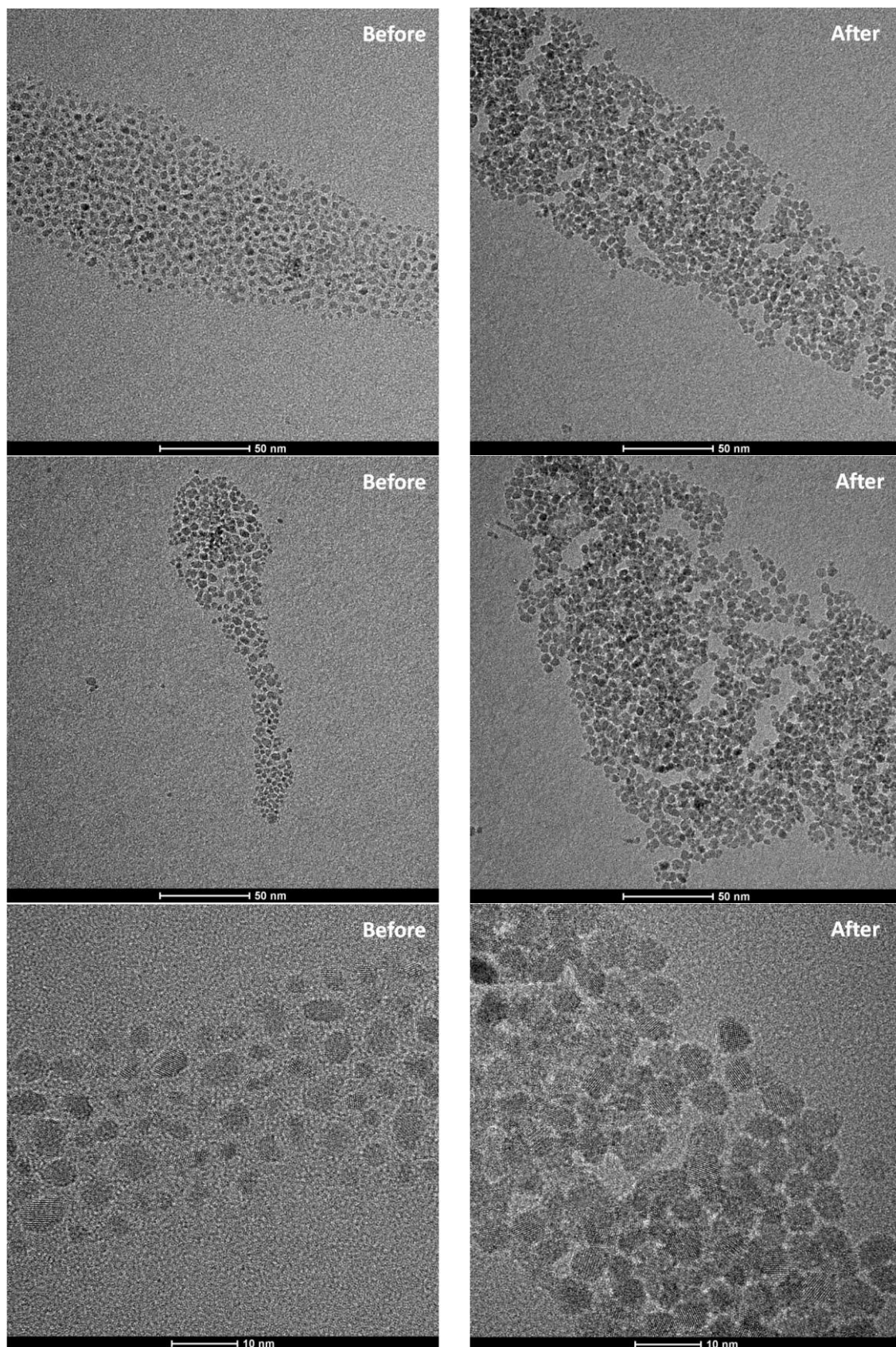
Figure B.5 - Low magnification HRTEM images before and after the *ex situ* test at 600°C for 60 minutes in mixed nanoparticles of CeO_2 and ZrO_2.
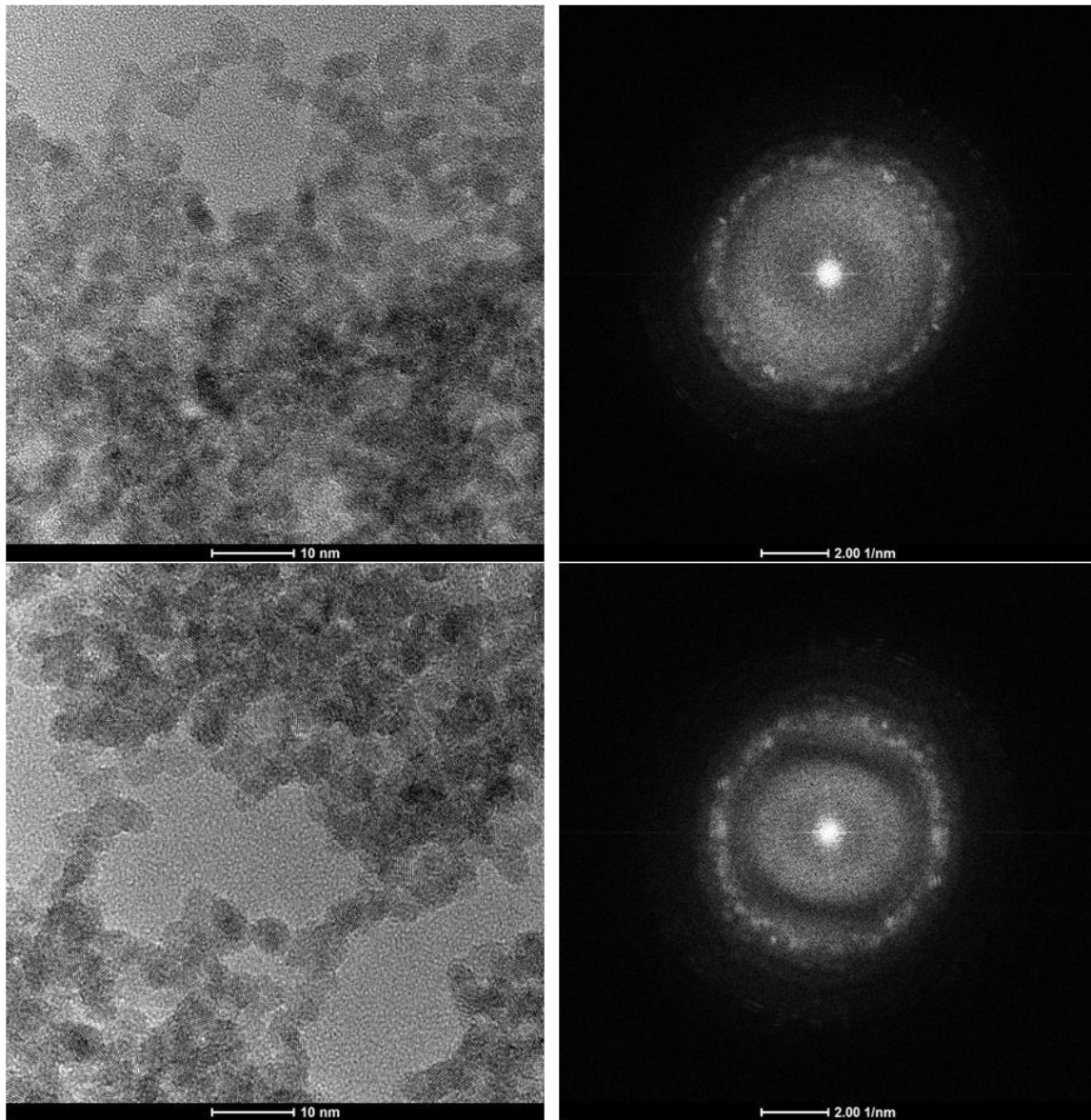
Figure B.6 - HRTEM images and his respective FFT, of mixed nanoparticles (CeO$_2$ and ZrO$_2$) before *in situ* heating at 950°C for 360 minutes.
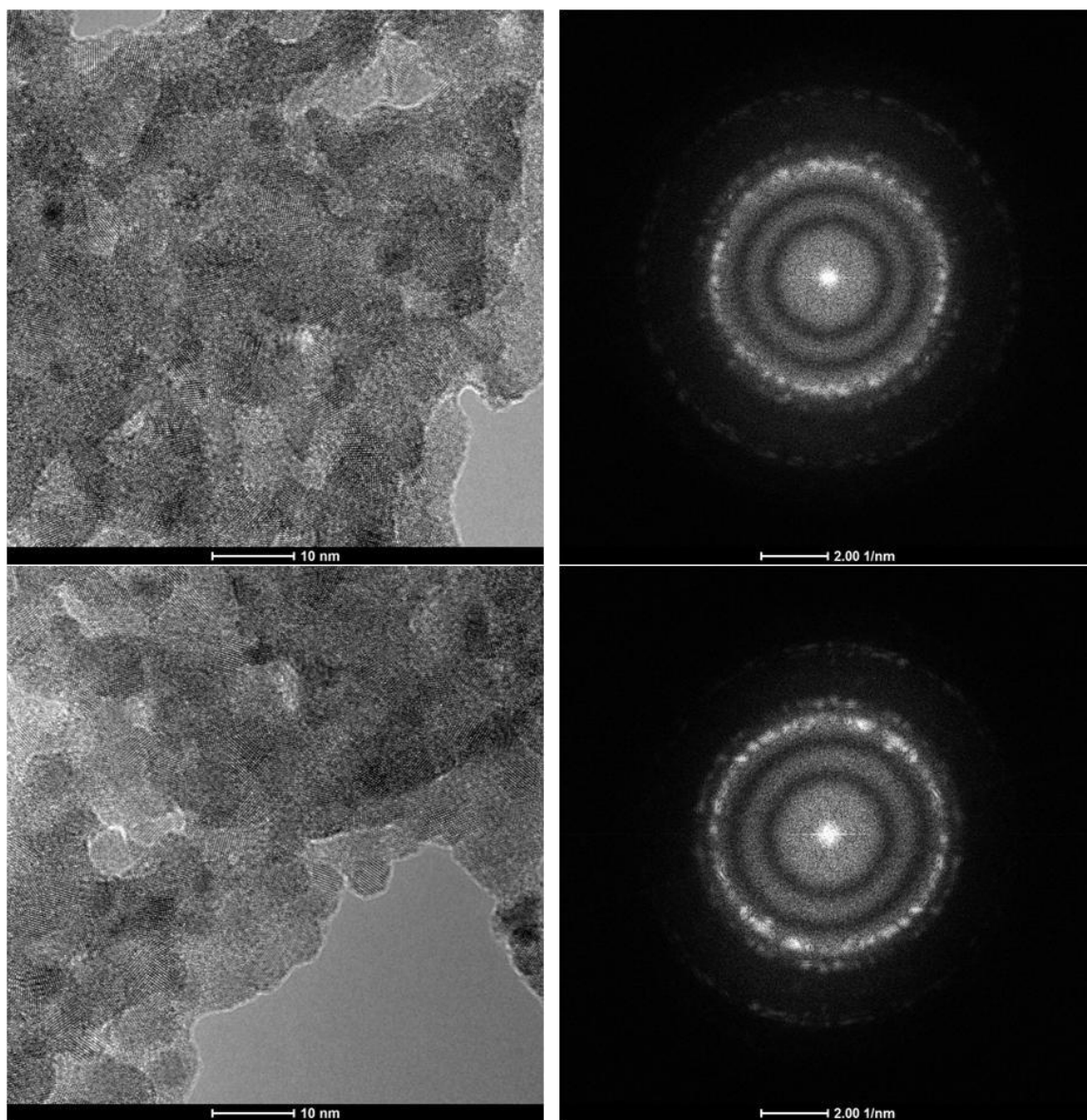
Figure B.7 - HRTEM images and his respective FFT, of mixed nanoparticles (CeO_2 and ZrO_2) after *in situ* heating at 950°C for 360 minutes.